Copper-Based Nanowires for Printable Memory and Stretchable Conductors

by

Matthew Joseph Catenacci

Department of Chemistry
Duke University

Date:_____
Approved:

_____
Benjamin Wiley, Supervisor

_____
Stephen Craig

_____
Jie Liu

_____
Aaron Franklin

Dissertation submitted in partial fulfillment of
the requirements for the degree of Doctor
of Philosophy in the Department of
Chemistry in the Graduate School
of Duke University

2018

ABSTRACT

Copper-Based Nanowires for Printable Memory and Stretchable Conductors

by

Matthew Joseph Catenacci

Department of Chemistry
Duke University

Date:_____
Approved:

_____
Benjamin Wiley, Supervisor

_____
Stephen Craig

_____
Jie Liu

_____
Aaron Franklin

An abstract of a dissertation submitted in partial
fulfillment of the requirements for the degree
of Doctor of Philosophy in the Department of
Chemistry in the Graduate School of
Duke University

2018

Copyright by
Matthew Joseph Catenacci
2018

Abstract

In the field of electronic materials, metal nanowires have been extensively studied for both their syntheses and their properties in electronic composites and devices. This dissertation addresses challenges in the field of electronic materials development with the use of copper nanowires synthesized in gram-scale syntheses, as well as provides analysis of devices and composites that could only be feasibly manufactured thanks to the large-scale syntheses.

In the field of printed electronics, there has been research into the development of fully printed memories. One of the challenges has been developing a memory that has switching characteristics that are on par with existing commercial memories, such as Flash memory. This can be achieved with a composite of Cu-SiO_2 nanowires dispersed in ethylcellulose, which acts as a resistive switch when between printed Cu and Au electrodes. A 16-cell crossbar array of these memristors was printed with an aerosol jet. The memristors exhibited moderate operating voltages (~3 V), no degradation over 10^4 switching cycles, write speeds of 3 μs, and extrapolated retention times of 10 years. The low operating voltage enabled the programming of a fully printed 4-bit memristor array with an Arduino. The excellent performance of these fully printed memristors could help enable the creation of fully printed RFID tags and sensors with integrated data

storage. Thanks to the large-scale synthesis of copper nanowires, this can allow for the expanded production of high-quality, fully printed memories.

Materials that retain a high conductivity under strain are essential for wearable electronics. I describe a new conductive, stretchable composite consisting of a Cu-Ag core-shell nanowire felt infiltrated with a silicone elastomer. This composite exhibits a retention of conductivity under strain that is superior to any composite with a conductivity greater than 1000 S cm^{-1}. This work also shows how the mechanical properties, conductivity, and deformation mechanisms of the composite changes as a function of the stiffness of the silicone matrix. The retention of conductivity under strain was found to decrease as the Young's modulus of the matrix increased. This was attributed to void formation as a result of debonding between the nanowire felt and the elastomer. The nanowire composite was also patterned to create serpentine circuits with a stretchability of 300%. Composites of this scale and density could only be feasibly manufactured thanks to large-scale syntheses of copper nanowires and the silver coating of copper nanowires. With the advances made in the quality of stretchable conductive composites, alternate methods were employed as to manufacture new composites and structures, such as the cofiltration of nanowires and waterborne rubber to accelerate production, or the manufacturing of Cu-Ag nanowire aerogels with density tunable via the aspect ratio of the nanowires.

Dedication

I would like to dedicate this dissertation to my mother, father, and four older siblings, for all they have done to help me come to where I am today.

Contents

Abstract iv

List of Tables x

List of Figures xi

Acknowledgements xiv

1. Introduction 1

1.1 Large scale synthesis of Cu NWs and applications 2

1.2 Cu-SiO_2 NWs for Fully Printed Memory 7

1.3 Cu-Ag NWs for Stretchable Conductive Composites 15

2. Fully Printed Memory 20

2.1 Manufacturing of Printed Memory Devices 21

2.1.1 Cu-SiO_2 NW Synthesis 21

2.1.2 PDMS Ink and Device Manufacturing 22

2.1.3 Fully Printed Device Manufacturing 24

2.1.4 Switching and Write Speed Measurements 25

2.1.5 Programming Tests 27

2.2 PDMS-Composite Device Properties 28

2.2.1 Cu-SiO_2 NW and Device Imaging 28

2.2.2 Resistive Switching 29

2.2.3 Retention 33

2.2.4 Write Speed 34

2.2.5 Summary 35
2.3 Fully Printed Device Properties 35
2.3.1 Device Imaging 35
2.3.2 Resistive Switching 36
2.3.3 Retention 40
2.3.4 Write Speed 40
2.3.5 Circuit Integration 41
2.3.6 Summary 43
3. Conductive Stretchable Composites 44
3.1 Manufacturing of Composites 45
3.1.1 Cu-Ag NW synthesis 45
3.1.2 Filtration and Infiltration 46
3.1.3 Electrical and Strain Characterization 48
3.1.4 Device Manufacturing 49
3.2 Composite Properties 49
3.2.1 Fabrication and Conductivity 49
3.2.2 Effect of Matrix Stiffness on Conductivity as a Function of Strain 51
3.2.3 Composite Cycling 58
3.2.4 Time-Dependent Behavior 64
3.2.5 Patterning for Circuit Manufacturing 67
3.3 Summary 70
4. NW Composites from Cofiltration and Aerogels 71

4.1 Cofiltration of Cu-Ag NWs and Waterborne Elastomer 71

4.1.1 Cofiltration Methods and Materials 72

4.1.2 Cofiltration Results and Conductivity 74

4.1.3 Stress vs. Strain and R/R_0 vs. Strain Analysis 77

4.1.4 Composite Cycling 80

4.1.5 Summary 83

4.2 Cu-Ag NW Aerogels 84

4.2.1 Manufacturing Aerogels of Cu-Ag NWs with Varied Aspect Ratios 85

4.2.2 Visualization and Density Characteristics of Aerogels 87

4.2.3 Summary 90

5. Conclusion 91

References 93

Biography 106

List of Tables

Table 1: Comparison of switching properties of published fully printed memories and this current work 12

List of Figures

Figure 1: Large-scale synthesis of Cu NWs. 4

Figure 2: Resistivity vs. sintering temperature for 41 μm Cu-Ag NWs, 27 μm Ag NWs, and Ag NPs. 6

Figure 3: Schematic illustration of roll-to-roll gravure-printed antennas, electrodes, and wires 10

Figure 4: Performance comparison of 3D stretchable conductive composites 15

Figure 5: Circuit diagram for the switching speed test. 26

Figure 6: TEM image of Cu-SiO_2 NWs 28

Figure 7: Schematic of the PDMS composite device. 29

Figure 8: Performance of PDMS composite memristor during forming and cycling 30

Figure 9: Cross-sectional schematics illustrating the operating mechanism of the Cu-SiO_2 NW memristor. 31

Figure 10: Cycling properties of the PDMS composite memristor. 32

Figure 11: Plot of ON resistance vs. time over 10^4 s for the PDMS composite memristor. 33

Figure 12: Write speed characteristics of a single write step for the PDMS composite memristor. 34

Figure 13: Imaging of fully printed memristor array 35

Figure 14: Performance of a fully printed memristor during forming and cycling 36

Figure 15: Cycling behavior of the fully printed memristor array over multiple cells. 38

Figure 16: Plot of ON resistances versus time over three separate devices. 39

Figure 17: Write speed characteristics of the fully printed memory. 41

Figure 18: Example circuit utilizing a 4-bit fully printed memristor. 43

Figure 19: Schematic and dimensions of the ASTM D412 test specimen..... 47

Figure 20: Procedure for stretchable conductive composite manufacturing..... 50

Figure 21: Conductivity of Cu-Ag NW felts vs. annealing temperature 51

Figure 22: Stiffness vs. conductivity behavior of stretchable conductive composites 53

Figure 23: Images showing the difference in the stretchability and void formation..... 54

Figure 24: SEM images of the Ecoflex and Dragon Skin composites..... 56

Figure 25: Comparison of stretchable conductive composites and annealing condition. 57

Figure 26: Cycling behavior of the stretchable conductive composites. 59

Figure 27: Hysteresis behavior of plain PDMS 60

Figure 28: Analysis of composites during strain before and after cycling..... 61

Figure 29: Strain rate dependence on composite behavior. 65

Figure 30: Demonstration of stretchable LED circuit..... 67

Figure 31: Serpentine Cu-Ag NW trace properties 69

Figure 32: SEM microscope image of plain PU microspheres. 73

Figure 33: Procedure for the cofiltration method for composite manufacturing..... 75

Figure 34: Cofiltered composite properties relative to annealing. 76

Figure 35: Comparison of PDMS-infiltrated composites vs. PU-cofiltered composites. .. 77

Figure 36: SEM images of the PU composite..... 79

Figure 37: Cycling behavior of the PU composite relative to the Dragon Skin composite. 81

Figure 38: Analysis of PU and Dragon Skin composites during strain before and after cycling..... 83

Figure 39: Photograph of settled Cu-Ag NWs in solution and subsequent aerogels formed after freeze-drying. 87

Figure 40: Density calculations of Cu-Ag NWs relative to aspect ratio 88

Figure 41: Microscope image of aerogel made with 175 AR Cu-Ag NWs. 90

Acknowledgements

I would like to thank Dr. Benjamin Wiley for his support and encouragement in tackling ambitious research projects, which allowed for great strides in the fields of materials chemistry and materials science. I would also like to thank my undergraduate advisor, Dr. Gregory Hartland, for fostering my interest in nanomaterials and nanomaterial analysis in his research laboratory at the University of Notre Dame. Lastly, I would like to thank Duke University for providing the resources and facilities I needed to pursue my research projects.

1. Introduction

As the field of electronics expands, so too does the field of materials science and materials chemistry in order to develop and synthesize materials for improved electronic devices. For example, research into semiconductor materials was and continues to be essential to the development of modern computing, allowing for the transition from large, vacuum-tube based computers down to the microchips and nanoscale transistors we see in today's devices. As the demand for electronic devices with capabilities such as flexibility, reduced cost, and improved ease of processing increases, so too does the demand for the development of novel electronic materials that can allow for the manufacturing of such devices.

One of the branches of materials chemistry that has undergone extensive research and development in recent years is the synthesis of metal nanomaterials, specifically metal nanowires. These one-dimensional structures can be made from a variety of metals, but a great deal of research has focused upon the syntheses and applications of silver nanowires (Ag NWs) and copper nanowires (Cu NWs). One of the greatest advantages of metal nanowires is that they can be used in applications that may require the use of metals, but can be used at reduced volume while retaining certain beneficial bulk properties, such as high electrical and thermal conductivity.[1-3] Likewise,

metal nanowire networks can have unique properties that are not seen in bulk metal structures which allow for expanded device capabilities, such as transparency, flexibility, and stretchability.[4-7] For example, low-density networks of conductive metal nanowires can act as a replacement for indium tin oxide (ITO) for transparent conductors. Not only can the use of metal nanomaterials be cheaper than the use of ITO, specifically due to the high costs of indium production and the sputtering processes requires to deposit ITO, the conductivity and transparency of Ag NW films can be competitive with ITO films.[8-9] In addition, conductive nanowire networks can be readily solution coated or printed,[8, 10-11] which allows for greater ease of production and more rapid production than devices manufactured using evaporated or sputtered conductive materials. As the demand increases for electronic devices with expanded capabilities and reduced processing costs, metal nanowire networks can fill such niches for new devices.

1.1 Large scale synthesis of Cu NWs and applications

Cu NWs have come into great focus within the Wiley lab, due to the development of large-scale, multi-gram syntheses that are faster, cheaper, and greener than those of other metal nanowires, which allows for the development of large-scale and highly-concentrated composites using Cu NWs as a filler material. For example, the

challenge with most metal nanowire syntheses are the time, temperature, and media suitable for nanowire formation and growth, as well as the maximum length of the nanowires after reaction completion. One of the main competitors for Cu NWs are Ag NWs, and there are significant challenges in the large-scale synthesis of Ag NWs. Previous studies that have looked into large-scale, electrically conductive composites of Ag NWs for gel-based and scaffold-based networks[12-14] all used a specific polyol synthesis for Ag NW production for the scale they found necessary. This process requires reaction temperatures in excess of 200 °C, a non-aqueous reaction media of glycerol, and results in NWs limited to length to approximately 15 μm.[15]

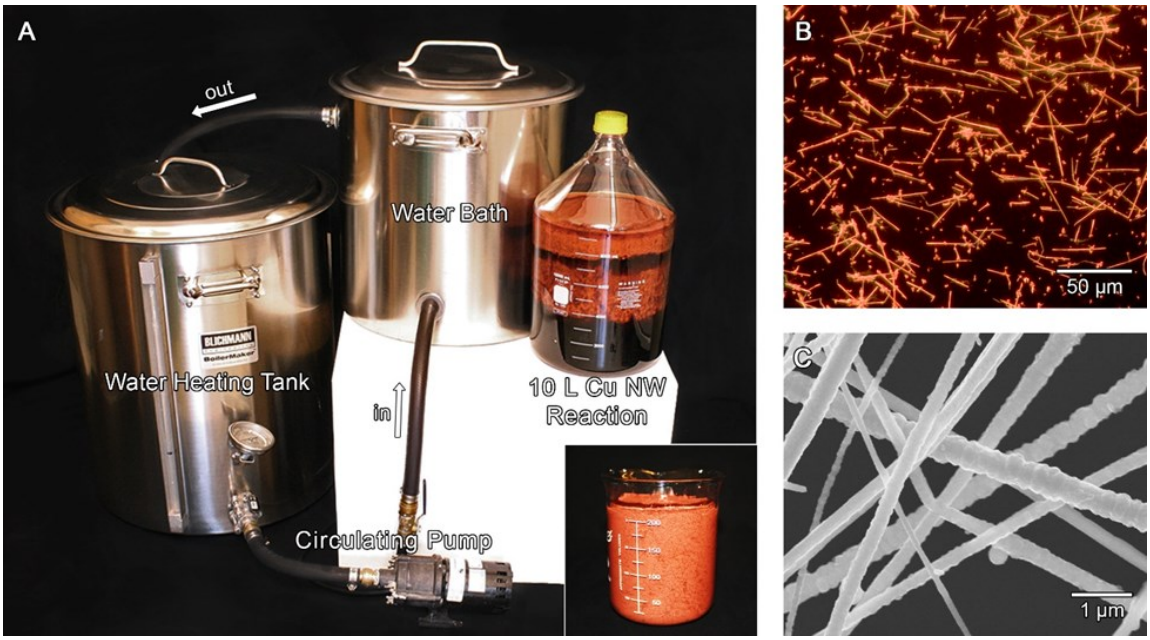

Figure 1: Large-scale synthesis of Cu NWs. (a) Circulating water bath set up for the 10 L synthesis of Cu NWs. Inset shows approximately 22 g of Cu NWs purified from the reaction. (b) Dark-field optical microscopy image shows the Cu NWs have an average length of 45 ± 15 µm. (c) An SEM image shows the Cu NWs have a diameter of 240 ± 95 nm.[16]The large-scale synthesis of Cu NWs avoids most of the problems associated with the large-scale Ag NW synthesis. For example, as seen in Figure 1, there has been recent development of a large-scale synthesis that is capable to producing Cu NWs at a scale of 4.4 g/hr in a 10 L reaction vessel. This is done at a cost of less than $7 per gram, is performed at 60 °C in aqueous media, is more environmentally friendly than other Cu NW syntheses by replacing hydrazine as a reducing agent with glucose,[17] and produces NWs that are over 40 µm in length.[16] Thanks to this synthesis, the manufacturing of electrically conductive 3D printer filaments, using Cu-Ag core-shell NWs (Cu-Ag NWs)

as a conductive filler in polycaprolactone (PCL) thermoplastic, is both physically and economically feasible. Thanks to the use of Cu-Ag NWs, these conductive 3D printer filaments are 100x more conductive (0.002 Ω*cm) than commercially available conductive 3D printer filaments that use graphene as a conductive filler.[16] Additionally, as seen in Figure 2, the Cu-Ag NWs grown in this reaction leads to filtered NW networks with conductivities comparable with Ag NWs when both are deposited at room temperature. The synthesis of these specific Ag NWs requires 6 h at 130 °C to grow to approximately 27 μm in length and must be performed in ethylene glycol.[18] For reference, both of these networks surpass the conductivity of networks based on silver nanoparticles (Ag NPs) at low temperature, which mandate high-temperature annealing for high conductivity.[19] This allows for the deposition of high-conductivity networks with low-temperature processing techniques, which is beneficial for printing on sensitive or biological substrates.[19-22] With such capabilities available thanks to large-scale, low-cost, and low-carbon footprint syntheses of Cu NWs, there are many avenues opening up that allow for the implementation of copper and copper-based nanowires, as well as scientific exploration as to the behavior of large-scale and high-density Cu NW composites.

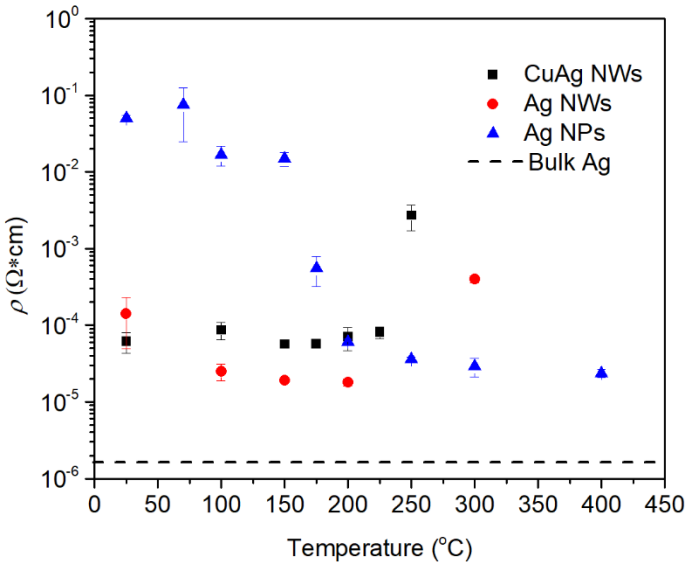

Figure 2: Resistivity vs. sintering temperature for 41 µm Cu-Ag NWs, 27 µm Ag NWs, and Ag NPs. Cu-Ag NW and Ag NW results are from experiments using felts, Ag NP results are from a dropcasting technique described in Stewart *et. al.*[19]

In Chapter 1, I introduce a background of how Cu NWs can be applied in the development of improved electronic composites for applications in printed and stretchable electronics. In Chapter 2, I focus on the development of memristors using copper-silica core-shell nanowires (Cu-SiO_2 NWs), from preliminary analysis of the memory properties of the nanowires, towards the manufacturing of a fully printed and programmable memory array. Through this, we achieved high performance metrics competitive with Flash memory, all while using materials that can be printed via aerosol-jet. Next, in Chapter 3, I focus on how Cu-Ag NWs can be integrated into

stretchable conductive composites. Thanks to the multi-gram synthesis of Cu NWs and the ability to filter the nanowires into a free-standing, felt-like material, we were able to manufacture a stretchable conductive composite with high conductivity, high retention of conductivity after strain cycling, and can be patterned into stretchable LED circuits. Finally, in Chapter 4, I compare the results of this stretchable conductive composite from Chapter 3 relative to a novel manufacturing technique of cofiltering nanowires with waterborne rubber, as well as how the density of Cu-Ag NW aerogels, a potential competitor for Cu-Ag NW felts, can be manufactured and modified by tuning the dimensions of the Cu-Ag NWs.

1.2 Cu-SiO_2 NWs for Fully Printed Memory

Printed electronics enables the rapid prototyping of circuits on a wide variety of curved and flexible substrates, as well as the scalable and low-cost production of simple electronic components or devices.[23] Examples of printed electronic devices include circuit boards,[24] transistors,[25] sensors,[26] radio frequency identification tags (RFID),[27] solar cells,[28] light emitting diodes,[29] transparent electrodes,[17] touch screens,[30] amplifiers,[31] batteries,[32] flexible displays[33] and implantable bioelectronic devices.[34] An ongoing problem with printed electronics is the development of materials and processing methods that enable fully printed electronic components to have properties that are

comparable to their silicon-based counterparts, or at the very least, properties that are sufficient for practical use.

An area of printed electronics in which additional development is necessary is printable non-volatile memory, which will be essential for the development of fully printed RFID tags, e-paper, and sensors with integrated data storage.[35-36] While fully printed one-bit RFID tags have been previously researched, as antennas, rectifiers, and ring oscillators can be readily printed, as seen in Figure 3,[37] in order to develop a fully-realized multibit RFID tag, a memory component is required. Additionally, a non-volatile memory device is preferable as to not require a printed battery, as volatile memory devices would require a continuous source of power as to retain data. One approach to creating a printed memory is by polarizing selected areas in a ferroelectric polymer film, such as those made from poly(vinylidene fluoride) (PVDF) and its copolymers with trifluoroethylene (TfFe).[38-39] Printed ferroelectric polymer memories have write speeds as short as 5 ms,[39] can be switched for as many as 10^3 cycles,[38] require high operating voltages (>15 V),[36] and exhibit short retention times (<1 h).[40] A second approach to creating a printed memory is the creation of a film that enables the trapping of charge in graphene oxide,[41] polymer,[42] or nanoparticle-polymer composites.[36] These devices can be operated at voltages as low as 1.5 V,[43] switch for up to 10^3 cycles,[44] have

write speeds as fast as 10 ms,[42] and most retain charge for a few days. Kim *et. al.* reported a charge-trap based memory that could retain an ON-OFF ratio of ~10^3 for about 1 year, but this memory required 100 V to switch over a period of 1 s, and could only be switched for 50 cycles.[41] In comparison, Flash memory exhibits write speeds of 1 μs, retention times of 10 years, and can be cycled at least 10^4 times.[45] While there is some promise with these fully printed memories, alternative mechanisms for data storage are desirable in order to be competitive with Flash memory.

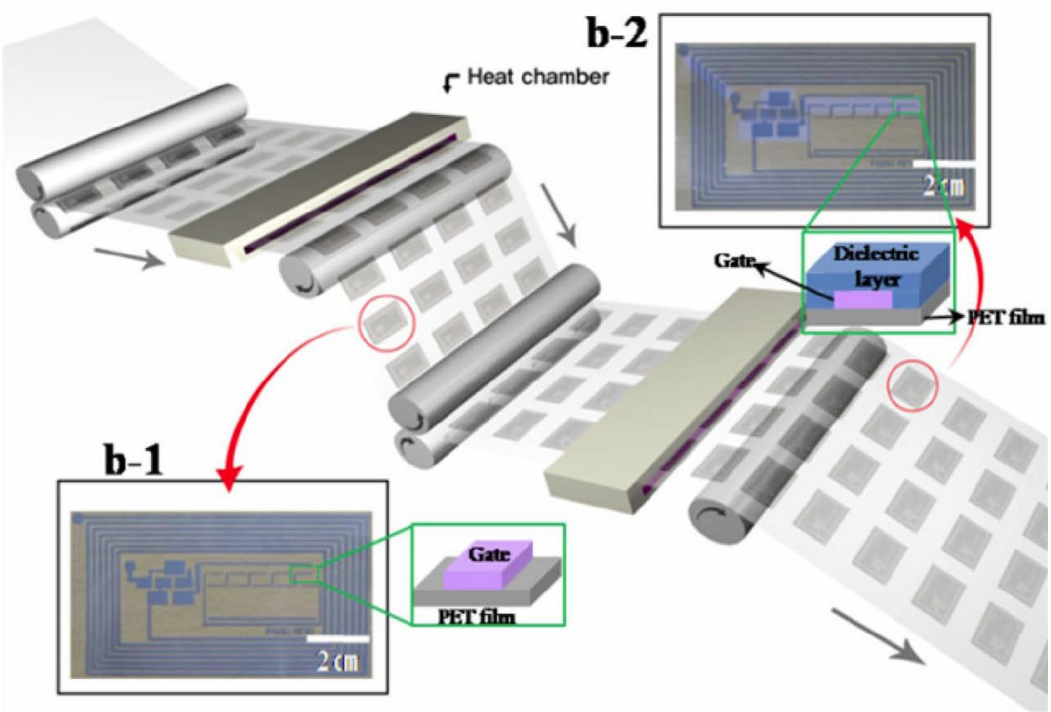

Figure 3: Schematic illustration of roll-to-roll gravure-printed antennas, electrodes, and wires using the silver-based conducting ink and printed dielectric layers on selectively designated spots using high-κ dielectric ink for fully printed RF tags[37]

A third approach to making a printable memory is to utilize materials that exhibit resistive switching; devices based on this mechanism are often referred to as memristors.[46] Typical memristors consist of a solid electrolyte between two metal electrodes, and are made using vapor-phase methods that allow for the creation of a very thin (30-50 nm) solid electrolyte layer.[47] Memristor devices made with vapor-phase methods have exhibited write speeds as small as 0.1 ns (1000x faster than Flash), up to 10^{11} switching cycles, and data retention times of up to 10 years. These performance

metrics indicate resistive switching is one of the most promising approaches to realizing a high-performance fully printed memory. To create fully printed memristor devices, the metal electrodes are typically made with Ag NP and Cu NP inks,[48] and the solid electrolytes are made from metal oxide nanoparticles such as TiO_2,[48-50] ZrO_2,[51] ZnO,[52] CuO_x,[53] and MoO_x/MoS_2.[54] Although a TiO_2 based device reported a switching speed faster than Flash (250 ns), it retained information for only 3 h, and required a sintering temperature of 500 °C,[50] which is highly limiting of the substrates this memory can be printed on. The best retention time for a printable memristor was 11 days for a ZrO_2-based device,[51] and the best endurance was 10^4 cycles for a MoO_x/MoS_2-based device.[54] Although the endurance of 10^4 cycles is comparable to Flash, the MoO_x/MoS_2-based device retained information for only a few hours, and had a switching speed of 5 ms. It may be that the poor performance of fully printed memristors relative to their vapor-phase deposited counterparts is the greater thickness (~100 nm) of the electrolyte or the roughness of the electrolyte/electrode interface.

Table 1: Comparison of switching properties of published fully printed memories and this current work

Materials (Electrode / Switching Layer / Electrode)	Memory Type	Write Speed	Write/erase voltages	Data retention time	ON/OFF cycling endurance
Ag / TiO_2 / C[49]	Resistive	100 μs	2 V / -3 V	8 h	10^3 cycles
Ag / TiO_2 / Mo-In_2O_3[50]	Resistive	250 ns	3 V / -3 V	3 h	10^3 cycles
Ag / MoO_x-MoS_2 / Ag[54]	Resistive	5 ms	1.5 V / -1.5 V	3 h	10^4 cycles
PEDOT:PSS / PMMA-rGO / PEDOT:PSS[41]	Charge-trap	1 s	100 V / -100 V	1 year	50 cycles
Ag / SiO_x / PEDOT:PSS[55]	Resistive	------	0.5 V / -0.5 V	4 h	10^3 cycles
Ag / ZrO_2 / Ag[56]	Resistive	------	3 V / -3 V	------	140 cycles
Ag / ZrO_2 / Ag[51]	Resistive	------	3 V / -3 V	11 days	50 cycles
Ag / TiO_2 / Cu[48]	Resistive	------	0.7 V/ -0.7 V	------	------
Ag / TiO_2 / Ag[57]	Resistive	5 ms	1.5 V/ -1.5 V	------	------
Ag / TiO_2 / Ag[58]	Resistive	------	1 V / -0.5 V	------	100 cycles
Ag / ZnO / Cu[52]	Resistive	------	1.3 V / -1.3 V	------	500 cycles
Ag / AgO-CuO / Cu[59]	Resistive	------	2 V / -3 V	------	40 cycles
Ag / CuO_x / Cu[53]	Resistive	------	1 V / -1 V	2 weeks	100 cycles
Ag / $ZnSnO_3$ / Ag[60]	Resistive	------	2 V / -2 V	24 min	100 cycles
Ag / $ZnSnO_3$-PVA / Ag[43]	Charge-trap	------	1.5 V / -1.5 V	36 h	500 cycles
ITO / GaZnO / ITO[61]	Charge-trap	------	6 V / -7 V	------	300 cycles
PEDOT:PSS / polyvinylphenol / PEDOT: PSS[62]	Charge-trap	------	30 V / -20 V	------	100 cycles
Ag / polyvinylphenol / Ag[63]	Charge-trap	------	1.4 V / -1.4 V	180 days	------
Ag / MoS_2-PVA / Ag[44]	Charge-trap	------	3 V / -3 V	1 day	10^3 cycles
Ag / PMMA-MEH:PPV / Ag[64]	Charge-trap	------	1.2 V / -1.2 V	5 days	50 cycles
Au/Cu-SiO_2/Cu[65] (this work)	**Resistive**	**3 μs**	**3 V / -3 V**	**10 years**	**10^4 cycles**

Table 1 summarizes the performance metrics for every fully printed memory that has been reported. Until recently, no fully printed device has reported excellent all-around performance: write speeds below 10 μs, retention times of 10 years, and an endurance greater than or equal to 10^4 cycles.

Excellent resistive switching properties have previously been observed using a thin film loaded with Cu-SiO_2 NWs, as previously researched in our laboratory.[66] The key motivation for the use of Cu-SiO_2 NWs is that the properties, kinetics, and mechanisms of resistive switching cells have been well-studied with the use of copper as an active electrode and SiO_2 as a solid electrolyte in an evaporated cell.[67-69] In addition, there have been previously studied syntheses that have successfully coated Ag NPs with amorphous silica using a modified Stöber process as to avoid metal etching, and can tune the thickness of the SiO_2 shell depending on the concentration of SiO_2 precursor used.[70] Therefore, through a simple chemical process, we can coat a continuous layer of SiO_2 solid electrolyte with sub-100 nm thickness on a Cu NW, which acts as an active electrode. Likewise, we can print these nanowires on the microscale, the standard resolution of printed techniques, with the electrochemistry associated with resistive switching still contained at the nanoscale NW-core/NW-shell/electrode interface, allowing for high quality resistive switching. These nanowires were successfully coated as a film atop evaporated copper active electrodes and gold inert electrodes on glass, where the conductive copper core of the nanowires act as a via between the two

electrodes. These devices have modest switching voltages (2 V), a fast switching speed (50 ns), good endurance (>10^4 cycles), and data retention times (4 days) comparable to other fully printed memristors.[66]

In Chapter 2, I account the progress made in using Cu-SiO_2 NWs to manufacture a fully printed programmable crossbar array of memristors, with inks that were developed thanks to the large-scale synthesis of Cu NWs. Initial results focused upon making a proof of concept of a 3D architecture. This was done by replacing the coating of Cu-SiO_2 NWs as a 2D thin film by dispersing the Cu-SiO_2 NWs in a polymer-containing ink, which coats into a 3D, thick composite film with nanowires randomly oriented within the polymer matrix. Using evaporated Au bottom contacts and Cu top contacts, we were able to show that reliable resistive switching is capable in a vertical cell with electrodes deposited above and below the resistive switching composite. Thanks to this, we moved forward with making a fully printed memristor array, removing the metal evaporation step entirely. The crossbar array consists of sixteen individual memristors with printed Au bottom contacts, a printed polymer/Cu-SiO_2 NW composite as the resistive switching layer, and printed Cu top contacts. All layers were printed with an aerosol jet, and were shown to be printable on both glass and flexible Kapton tape. The memristors made in this fashion exhibited switching voltages of 3 ± 2 V, endurances of at least 10^4 cycles, 10 years of ON state retention, and write speeds of 3 ± 2 μs. These devices thus meet the performance requirements necessary for use as a

fully printed memory. We demonstrate the integration of these fully printed memristor arrays into a circuit to illustrate the use of a 4-bit memory to control LEDs.

1.3 Cu-Ag NWs for Stretchable Conductive Composites

Materials that are both conductive and stretchable are essential for the construction of stretchable circuits for use in wearables, robotics, bioelectronics, and energy storage.[71-76] While stretchable materials with low-conductivity (<1 S cm^{-1}) can be used for strain sensors or touch sensors, stretchable wiring and interconnects require conductivities as close as possible to copper (5.8×10^5 S cm^{-1}). In addition, such materials should retain their conductivity under high strain (>50%) after many cycles of stretching.

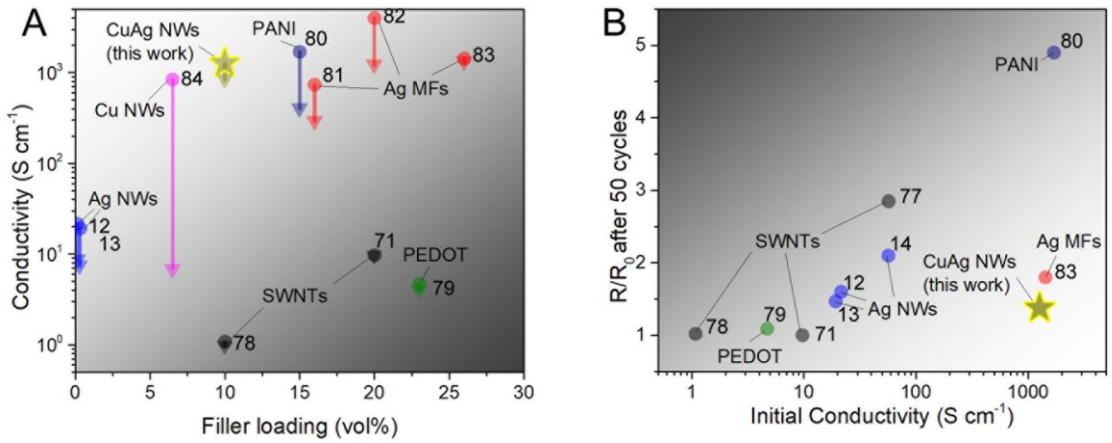

Figure 4: Performance comparison of 3D stretchable conductive composites (A) Conductivity of conductive composites at 0% (circle) and 100% (triangle) strain as a function of conductive filler loading. (B) R/R_0 after 50 cycles of stretching to 50% strain. Numbers indicate references.

Figure 4 shows a concise summary of some of the most remarkable stretchable, conductive composites reported to date. These include elastomers containing single-

walled carbon nanotubes (SWNTs),[71, 77-78] poly(3,4-ethylenedioxythiophene) (PEDOT),[79] polyaniline (PANI),[80] Ag microflakes (Ag MFs),[81-83] Ag NWs, and Cu NWs.[12-14, 84] While high conductivities have also been achieved in stretchable thin films, they have been left out of Figure 4 because their modes of mechanical deformation differ substantially from those of the bulk, 3D composites discussed in this work.[85-86] Among the previously made stretchable composites, those containing Ag MFs clearly stand out as exhibiting a combination of high initial conductivity, as well as retention of conductivity after 50 cycles of stretching to 50% strain. However, in order to retain conductivity after multiple cycles of stretching, it was necessary for the Ag MFs in these composites to be sintered together to form a continuous network. For example, although there are three Ag MF results in Figure 4A, only the sample in which the Ag was sintered together with photonic curing[83] exhibited a minimal (80%) increase in resistance after multiple cycles of stretching, and thus appears in Figure 4B. The other samples that were not sintered exhibited an increase in resistance greater than two orders of magnitude after 50 cycles of stretching to 50% strain.[81-82] This difference may be due to the Ag MFs being pulled apart within the composite when they are not sintered together. In contrast, a sintered porous network of Ag MFs may deform upon stretching with relatively minimal breakup of the interconnected particle network. Although these Ag MF results are highly informative and can provide direction for future work, Ag is rare, expensive, and

has a large carbon footprint. A future in which millions of people wear clothing imbued with stretchable circuitry cannot be built upon such a rare and costly element.

Cu is 1000 times more abundant, 100 times less expensive, and has a carbon footprint 25 times lower than Ag.[87] Previous work with Cu NW-based stretchable composites demonstrated the potential of Cu NWs to achieve high conductivities at low volume fractions due to their high aspect ratios (>$2.2*10^3$).[88] For example, Cu NWs mixed with poly(styrene-block-butadiene-block-styrene) (SBS) rubber obtained a conductivity of 844 S cm-1 at a loading of 7 vol%.[84] However, it is not practical to use bare Cu NWs because of their tendency to oxidize. In addition, this previous Cu NW composite exhibited poor retention of conductivity under strain, likely because the nanowires were mixed into an ink and were not annealed into an interconnected network.

Composites with improved material cyclability can be manufactured with the use of a free-standing interconnected network of conductive material, such as aerogels,[12, 78, 89] foams,[90] or the coating of a free-standing scaffold in conductive material.[13-14, 79] These networks can be subsequently vacuum infiltrated with elastomer, generating a stretchable conductive composite. A continuous, conductive network is established before the introduction of an insulating polymer matrix, allowing for generally higher conductivity with lower loadings relative to pre-blended polymer with conductive filler. For example, a 0.33 vol% dipcoated network of 4-15 μm Ag NWs infiltrated with polydimethylsiloxane (PDMS) exhibits a conductivity of 19.2 S cm^{-1},[13] while a composite

of Ag NWs of similar lengths blended with polystyrene does not reach percolation until a concentration of 2.3 vol%.[1] This method also allows for high material cyclability; a composite of cotton dipcoated in Ag NWs and subsequently infiltrated with PDMS shows an increase in resistance by a factor of 2.1 after 50 cycles at 50% strain with no further loss in conductivity with additional cycles, up to 10^3 cycles.[14] But due to the reduced loading of material in these specific free-standing and dip-coated networks (< 1 vol% for Ag NWs), conductivity is limited to below 60 S cm^{-1}. Therefore, the solution is to use a method to achieve a free-standing high-density network of conductive nanowires that can be infiltrated with elastomer, as to have both the high conductivity associated with high-density networks and the high cyclability associated with infiltrated, free-standing networks.

As I detail in Chapter 3, we hypothesized that these problems of material sustainability and performance for stretchable conductors could be addressed by creating stretchable composites from Cu-Ag NW felts. Cu-Ag NWs can be synthesized at relatively low cost (currently ~$7 per gram),[16] can form highly conductive composites, and are highly resistant to oxidation.[91] To ensure that the Cu-Ag NW composites retained their conductivity under strain, we developed a simple fabrication approach in which nanowires were filtered from solution and annealed together to form a highly-conductive freestanding felt. This approach ensured that the Cu-Ag NWs were electrically connected before infiltration with PDMS, and enabled the creation of

stretchable composites at a concentration of 10 vol% with a conductivity of 1220 S cm^{-1}, a value comparable to previous composites made with Ag MFs. In addition, the Cu-Ag NW composites exhibited only a 37% increase in resistance after stretching to 50% strain for 50 cycles, which is the lowest increase among any material with a conductivity >1000 S cm^{-1}.

Additionally, we show that the conductivity loss under strain is highly dependent on the stiffness of the elastic matrix. We observed that a difference in stiffness of the composite has altered effects of conductivity under strain that appears to be due to the formation of voids upon stretching. To conclude the chapter, we illustrate that the stretchable nanowire composite can be fabricated into serpentine patterns on fabric that retain their conductivity to strains of 300%. The combination of high performance and improved sustainability make Cu-Ag NW composites a promising material upon which to build a stretchable electronics industry.

These felts are made via a vacuum filtration technique with allows for a high-density, free-standing network of Cu-Ag NWs. In order to truly understand the quality of this network, two additional points of comparison are made in Chapter 4. First, the cofiltration of Cu-Ag NWs with elastomer microspheres is employed as a method of manufacturing to increase the rate of production of stretchable conductive composites. This technique for composite manufacturing generates a conductive stretchable composite with unique properties relative to the PDMS-infiltrated felt composite and

previously-studied ink-based composites due to the nature of contacts between nanowires in the composite and interactions between nanowires and the elastomer. Additionally, a variety of Cu-Ag NW aerogels are synthesized, using NWs of different aspect ratios, which can be tuned by altering the reaction conditions of the Cu NW synthesis. Because of this, aerogels of different densities can be manufactured, and can be compared in density to the properties of the Cu-Ag NW felts. Additionally, a greater understanding the properties of the Cu-Ag NWs after settling in solution and freeze-drying can provide a better understanding for potential applications of a Cu-Ag NW aerogel.

2. Fully Printed Memory

As previously researched, it has been proven that a thin film of coated Cu-SiO_2 NWs on active Cu and inert Au electrodes has great performance as a printed memory. In order to improve the practicality of this memory for device integration, a 3D architecture must be employed, as it can improve the density of the memory array. Additionally, replacing the evaporated metal electrodes with printed metal electrodes can reduce processing costs and improve the rate of device manufacturing. As the change of architecture and change in processing methods are required, so too are new material composites and chemical methods required to manufacture these composites. This chapter outlines the processing of a prototype 3D memory architecture using a Cu-SiO_2 NW-PDMS composite and evaporated metal electrodes, followed by the

manufacturing of a fully-aerosol printed memory array using a Cu-SiO_2 NW-ethylcellulose composite and printed metal electrodes.

2.1 Manufacturing of Printed Memory Devices

2.1.1 Cu-SiO_2 NW Synthesis

Cu NWs were synthesized in a manner similar to that reported previously.[92] To start, 50 mL of 0.1 M $Cu(NO_3)_2$ (Fischer Scientific, 99%), 7.5 mL of ethylenediamine (EDA, Fischer Scientific 99%), and 1 L of 12 M NaOH (NOAH, 99%) were added together in a 2 L round bottom flask and agitated by hand until mixed. The solution was then heated to 50°C while stirring vigorously, 1.25 mL of hydrazine (Fischer Scientific, 98% anhydrous) was added, and the solution continued to be stirred for 5 min. The solution was then left unstirred for 90 min to allow for Cu NW growth. The Cu NW product was then rinsed in a solution of polyvinylpyrrolidone (3 wt % PVP in H_2O, Aldrich, 10,000 MW) and 1% diethylhydroxylamine (1 wt % DEHA in H_2O, Aldrich) using a 2 L separation funnel. The procedure was repeated until Cu NWs were dispersed in solution. After rinsing, Cu NWs were dispersed in 1 L of the 3 wt% PVP, 1 wt% DEHA solution. The solution concentration was analyzed via atomic absorption spectroscopy (AAS) using a Perkin Elmer 3100 spectrophotometer. The concentration of Cu NWs in the final storage solution was 4.5 mg/mL.

The Cu NWs were coated with SiO_2 using a modified Stöber reaction that was originally developed for coating Ag NPs,[70] but which we modified for coating SiO_2 on

Cu NWs. To start, 15.34 mg (3.41 mL of the storage solution) of Cu NWs were dispersed into 1.7 mL of an aqueous solution containing 1% PVP (10,000 MW). The solution was added to 10.5 mL of ethanol (EtOH, 190 proof, Koptec), and stirred at 300 rpm in a 20 mL scintillation vial. Subsequently, 282 μL of dimethylamine solution (40 wt % DMA in H_2O, Aldrich) and 40 μL of tetraethylorthosilicate (TEOS, 98%, Acros Organics) were added. The reaction was left to stir for 10 min under ambient conditions. The reaction solution was then added to a 50 mL centrifuge tube containing 36 mL of 40:60 EtOH:H_2O to dilute to a 50:50 mixture of EtOH:H_2O. This solution was centrifuged at 2000 rpm for 10 min. The supernatant was removed, and the wires were rinsed three times with methanol (MeOH, 200 proof, Koptec) using the same centrifugation parameters. The solution was then concentrated to 10 mL in MeOH. A 5 μL portion was dried on ultrathin carbon supported by lacey carbon on a 400 mesh copper grid for transmission electron microscopy (TEM) with a FEI Tecnai G2 Twin Transmission Electron Microscope.

2.1.2 PDMS Ink and Device Manufacturing

The Cu-SiO_2 NW solution is stirred with 3 mL isopropyl alcohol (IPA, 99%, BDH) and 4 mL methylethylketone (MEK, 99+%, Sigma-Aldrich), along with 4 μL of 0.2% trimethoxymethylsilane (TMMS, 98%, Sigma Aldrich) in MEK solution as a functionalizing agent. The solution is then stirred for 15 hrs under ambient conditions to allow for surface functionalization of the SiO_2 shells and improve its dispersibility in

organic solution. After stirring, the solution is then rinsed three times with a 60:40 IPA:MEK solution, and then concentrated to 1.2 mL via centrifugation. This ink ratio was chosen for its good wettability on glass, its ability to dissolve uncured PDMS, and its previously-observed ability to result in good dispersions of functionalized colloidal silica in PDMS.[93] 60 μL of Sylgard-184 Silicone Elastomer Base is added with 12 μL of Sylgard 184 Silicone Curing Agent, and the ink is then agitated to form a disperse ink of 2.8 vol % NWs in PDMS.

Bottom inert electrodes were deposited using e-beam evaporation (5 nm Cr adhesion layer, 95 nm Au, Kurt Lesker PVD 75) on glass slides (75 mm x 25 mm) which were cleaned by sonication in acetone, rinsed with IPA, and plasma cleaned for one minute under air. The Cu-SiO_2 NW-PDMS ink was coated onto the substrate and Au electrodes using a doctor blade (MTI Co. Micrometer Adjustable Film Applicator), followed by curing for 8 hrs at 150°C to yield a 3 μm thick film. The slides were then subjected to 3x30 minute rinses in 50 mL of hexane (99%, Fisher) bath, a 30 min rinse in EtOH bath, 1 hr of drying in an 80°C oven, and a 1 min plasma clean in approximately 600 mTorr forming gas (95% N_2/5% H_2, Airgas) using a Harrick Plasma PDC-001. This was performed in order to ensure adhesion and good resolution of the sputtered top contacts to PDMS.[94] 100 nm thick Cu top contacts were then DC sputtered (Kurt Lesker PVD 75) on top of the PDMS film to complete the device. The volume of the switching

cell is 25 μm x 25 μm x 3 μm. Optical microscope images of the device were taken using a Meiji Techno Microscope.

2.1.3 Fully Printed Device Manufacturing

Au electrodes were printed using an Au ink (UTD-Au40, UT Dots Inc.) containing 40 wt% Au nanoparticles. The ink was printed as received on glass slides or polyimide film by an AJ-300 aerosol jet printer (Optomec Inc., USA). A 150 μm diameter nozzle was used for printing, and the flow rates of sheath gas and carrier gas were set to 50 sccm and 20 sccm, respectively. The platen temperature was maintained at 60 °C, and the printed Au nanoparticle layers were further sintered at 280 °C in air for 1 h in an oven. The printed film thickness was 450 nm, and the sheet resistance was 1.5 Ω/sq.

Cu-SiO_2 NWs in MeOH, as made identically in Chapter 2.1.1, were rinsed into a 30 mL solution of 1.5 wt% ethylcellulose (Ethocel 10, Dow) in MeOH. To facilitate the aerosol jet printing of the ink, 10% α-terpineol (≥96%, Aldrich) was added as a cosolvent into the ink to adjust its viscosity and evaporation rate. The as-prepared Cu-SiO_2 NW-ethylcellulose ink was printed using a wide nozzle with diameter of 1 mm, and the sheath, carrier and exhausting gas flow rates were set to be 60 sccm, 500 sccm and 480 sccm, respectively. All printing was carried out in air at room temperature while the platen was maintained at 70 °C to accelerate ink drying. The printed film thickness is around 4.5 μm.

Cu NP metal-organic decomposition (MOD) ink was derived and modified from a procedure reported by Shin, *et al.*[95] 10 mL of MeOH, 40 mmol of 2-amino-2-methyl-1-propanol (AMP, >99%, Aldrich), and 40 mmol of octylamine (99%, Alfa Aesar) was stirred for 30 min. Next, 40 mmol of copper (II) formate tetrahydrate (98%, Santa Cruz Biotechnology) was added, and stirred for 1 h. The subsequent solution was placed in a vacuum oven for 12 h under reduced pressure at 50°C to remove MeOH. The ink was completed by mixing the vacuumed product in a 3:2 weight ratio with isopropyl alcohol (IPA, 99.5%, BDH). The prepared ink was printed on top of the Cu-SiO_2 layer using the AJ-300 printer. A 150 μm diameter nozzle was used for printing, and the flow rates of sheath gas and carrier gas were set to 40 sccm and 25 sccm, respectively. The platen temperature was set to 40°C during printing. The printed samples were reduced and sintered at 160 °C for 30 min in a tube furnace under a flow of N_2. The printed film thickness was 900 nm. The volume of the switching cells are 250 μm x 250 μm x 4.5 μm.

2.1.4 Switching and Write Speed Measurements

Switching tests were performed with a Keithley 2400 SourceMeter connected via tungsten electrical probes (Micromanipulator Co.) for the PDMS-composite device, and copper clips for the fully printed device. The switching programs were written in LabVIEW 2012. Switching cycles were performed using a voltage sweep with a compliance current of 100 μA. Sweeps were performed at a rate of 1.5 V/s. Write and erase voltages are logged by reading the voltage recorded immediately before the switch

occurs, and the ON and OFF resistances were recorded by reading the resistance after each sweep at a read voltage of 100 mV.

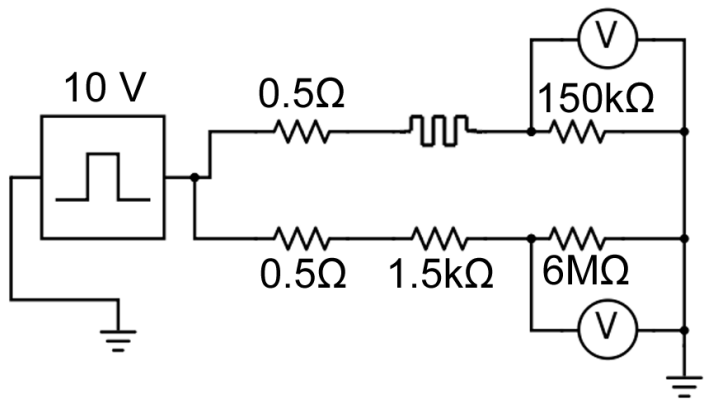

Figure 5: Circuit diagram for the switching speed test.

Write speed tests were performed using an Arduino UNO in conjunction with a VOLTEQ power supply, with voltages read using a Hantek DSO 5200A Oscilloscope. A schematic of the switching speed measurement is provided in Figure 5. A 150 kΩ resistor is in line with the memristor to limit the current through the memristor, and the voltage across this resistor is measured to calculate the current through the memristor. A 6 MΩ resistor is placed after the 1.5 kΩ counter resistor to measure the maximum voltage from the output pulse. Confirmation of the ON state was obtained by using the Keithley 2400 to measure the resistance of the memristor before and after pulse application.

2.1.5 Programming Tests

Programming tests were performed with an Arduino UNO, Keithley 2400 SourceMeter, and VOLTEQ power supply. A 4-bit array of printed memristors was programmed by supplying a 5 V pulse for 500 ms using four outputs from the Arduino. An 8.1 kΩ resistor was placed in line of each memristor to limit the current through the memristors. A 56 kΩ resistor was also added between the base of each transistor and ground. The memristors were read by supplying a 0.7 V across all four memristors using a Keithley 2400 SourceMeter. In the OFF state, 0.7 V is insufficient to turn on the npn bipolar junction transistors (BJT) due to the voltage drop across the memristor. In the ON state, the voltage drop over the memristor is low, allowing the 0.7 V to turn on the BJT and thereby light the LED. Erasing of the device was performed using the previously described LabVIEW program to sweep negative voltage across each memristor until the device was completely erased.

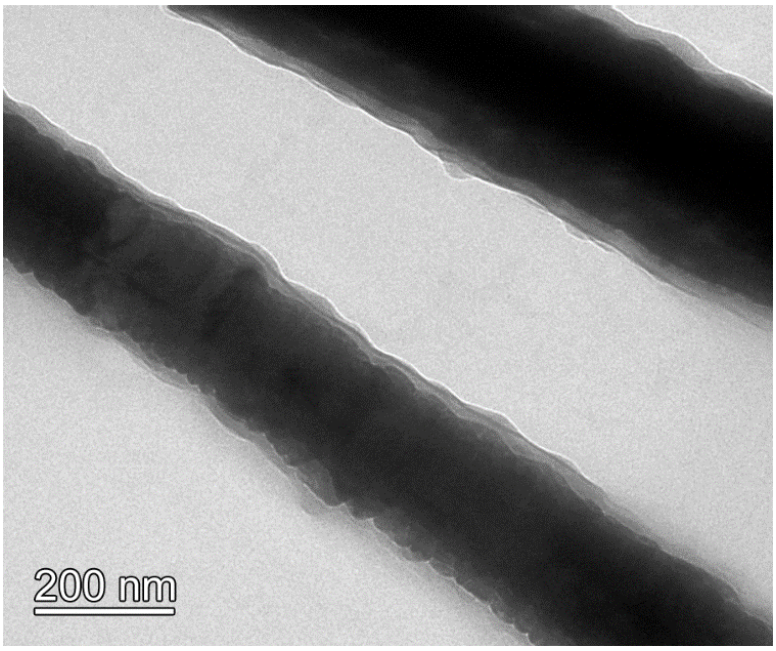

Figure 6: TEM image of Cu-SiO_2 NWs

2.2 PDMS-Composite Device Properties

2.2.1 Cu-SiO_2 NW and Device Imaging

TEM images (Figure 6) show an example of the SiO_2 shells grown on the copper nanowires. The average measured thickness of the SiO_2 shells was 18 ± 3.6 nm, which is thin enough to allow for consistent resistive switching,[67] but thick enough to electrically insulate the nanowires from one another.[66] Additionally, the use of DMA as a catalyst in this reaction was also successful, as there is no observable damage to the Cu cores. The cores are intact and contain no gaps to indicate the partial formation of a silica nanotube, which is observable when ammonia, the typical catalyst used in the Stöber process, is used in its place.[96] Figure 7A shows an optical microscope image of the device, where

Au bottom electrodes, Cu-SiO_2 NW switching layer, and Cu top electrodes are visible. Figure 7B illustrates an inset of one of the given switching cells, where it is hypothesized in the given region, there is at least one randomly-oriented NW in the matrix in contact with both the Au bottom electrode and the Cu top electrode. This technique of using a random NW network of a given density to assure at least one NW bridged the gap between two electrodes was previously used for the thin-film memory device.[66]

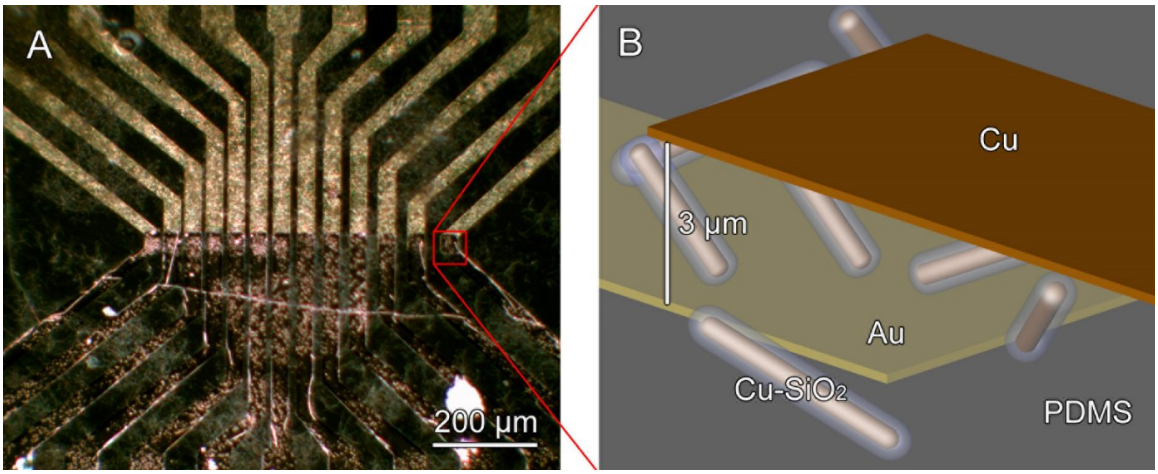

Figure 7: Schematic of the PDMS composite device. (A) Optical microscope image of device with Au bottom contact, Cu top contact, and Cu-SiO_2 NW-PDMS composite switching layer. (B) Illustration of a single memory element.

2.2.2 Resistive Switching

After the device is printed, an initial forming step enables its use as a memristor. A characteristic I-V curve for the forming step is shown in Figure 8A. As the voltage applied to the Cu top contact is swept in the positive direction, the current increases by 10^5 times at 27 V, and is limited by a compliance current set to 100 µA. After the forming step, the device can be reversibly switched between a low-resistance and high-resistance

states. Figure 8B shows a typical I-V curve for bipolar resistive switching of the device. After a memristor has gone through the forming stage and is in the low-resistance state, it can be turned back to the OFF state by reversing the bias, with a positive bias applied to the bottom Au contact. When the voltage reaches approximately -3 V, the current decreases by 10^5 times as the memory reverts to the high-resistance state. The memristor can again be returned to the low-resistance ON state by application of a positive bias to the Cu top contact.

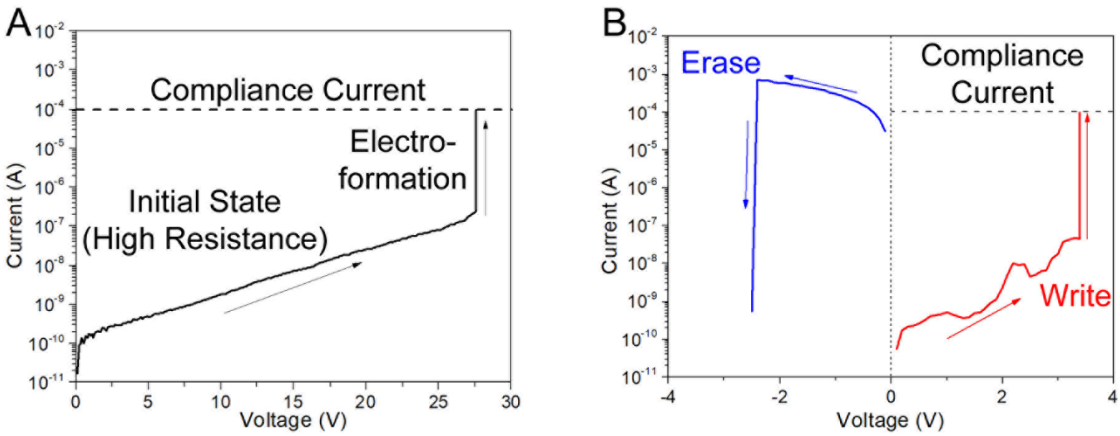

Figure 8: Performance of PDMS composite memristor during forming and cycling (A) Plot of the current and voltage in the memristor during forming. (B) Plot of the current and voltage in the memristor during erasing and writing.

It is thought that the resistance of the SiO_2 junctions between nanowires and the contacts drops due to an electrochemical metallization mechanism, in which the positive bias results in dissolution of the Cu top contact, diffusion of Cu ions through the SiO_2 shell, and reduction of Cu ions on a Cu NW until a Cu filament forms between the Cu NW and the top contact (Figure 9A&B).[47, 66] Filament formation subsequently takes places in

a similar manner between the Cu NW and the Au bottom contact, resulting in a dramatic drop in the resistance between the top and bottom contacts. This low-resistance state is the ON state. To switch the device back to the OFF state, a negative bias can be applied to the Cu electrode, resulting in anodic dissolution of the Cu filament in the SiO_2 shell between the Cu NW and the Au electrode (Figure 9C). In the OFF state, the device can be switched back ON by reapplication of a positive bias to the Cu electrode, leading to regrowth of the filament. Because of the shorter distance Cu ions migrate for the write step compared to the form step, the voltage required for writing (3 V) is less than that required for forming (27 V).[68]

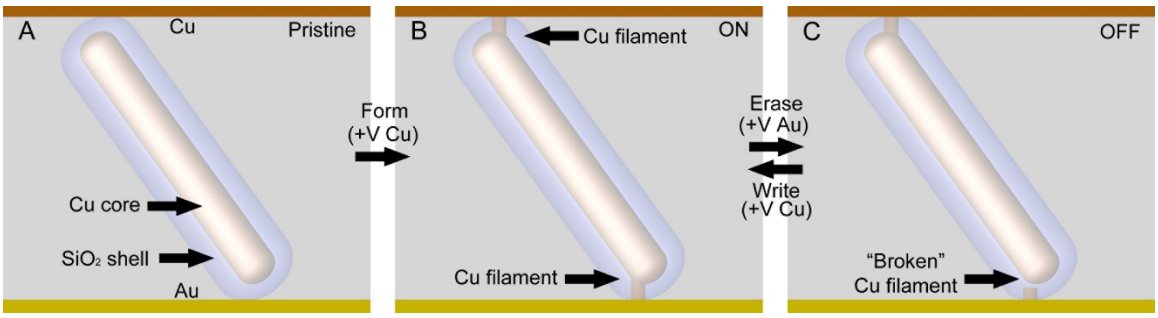

Figure 9: Cross-sectional schematics illustrating the operating mechanism of the Cu-SiO_2 NW memristor. (A) Application of a positive bias to the Cu top contact induces the growth of Cu filaments to form a conductive pathway, resulting in the (B) ON state. The memristor can then be erased by applying a reverse bias to dissolve the filament, resulting in the (C) OFF state.

Figure 10A shows the cumulative switching voltage in a switching cell in this device over the course of 100 cycles. The average write voltage of the given memristor was 3.7 ± 1.9 V, with a maximum voltage of 8.9 V. The average erase voltage was -3.2 ± 1.5 V, with a maximum voltage of -7.4 V. Relative to the thin-film memory using Cu-

SiO_2 NWs, we are seeing comparable switching voltages (2.5 ± 0.6 V to write, -1.8 ± 0.9 V to erase), indicating that the change in architecture of the device has no major effect on the overall cycling performance of the device.

Figure 10B shows that the memristor is capable of switching with $R_{OFF}/R_{ON} > 10^3$ over 10^3 cycles with no observable degradation in ON or OFF state resistance. The OFF state appears noisy due to the limit of detection of the instrument at high resistance vales. Regardless, no visible degradation in quality is observed over 10^3 cycles, suggesting both strong endurance in this range and the potential for the cycling endurance to be greater than 10^3 cycles.

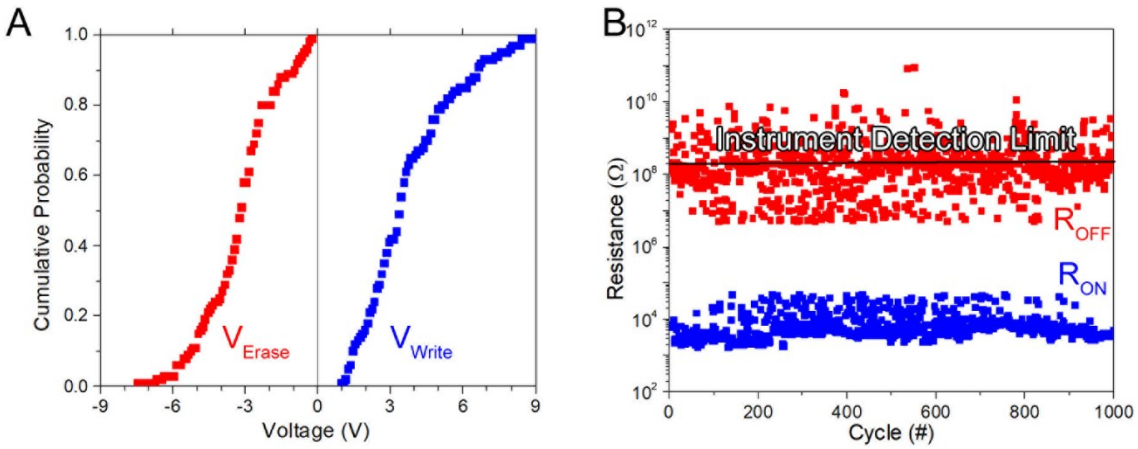

Figure 10: Cycling properties of the PDMS composite memristor. (A) Cumulative probability of write and erase voltages (n=100). (B) ON and OFF resistances over 10^3 cycles. The highlighted horizontal line labeled "Instrument Detection Limit" indicates the highest resistance that can be accurately measured given a 100 mV read voltage with the instrument used.

2.2.3 Retention

A device was tested for retention of the ON state over time in air at room temperature (Figure 11). The ON state was read periodically with a 100 mV read voltage over the course of 10^4 s. A negligible increase in resistance was observed over this time period, and remained at a resistance 10^5 lower than the average OFF state resistance, as calculated from Figure 10B. This shows good non-volatility of the memristor, and makes it competitive with other fully printed memory devices in the literature that have observed the full range of switching properties.[50, 54]

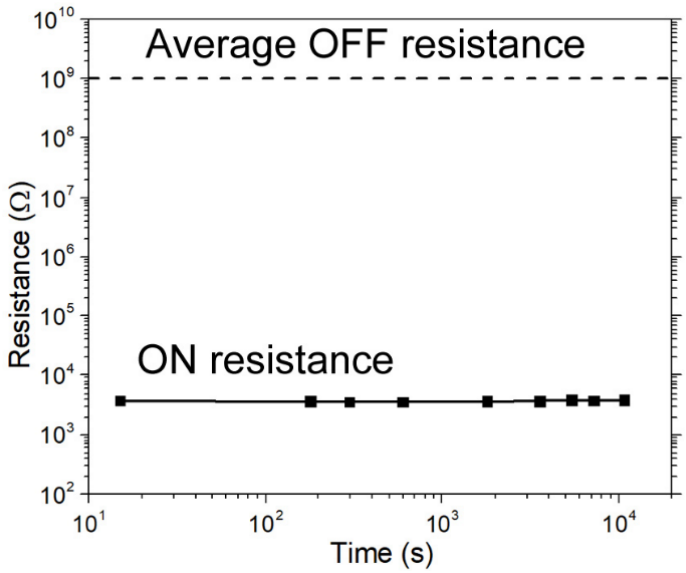

Figure 11: Plot of ON resistance vs. time over 10^4 s for the PDMS composite memristor.

2.2.4 Write Speed

The write speed of the system was characterized by applying a write voltage across a memristor, and measuring the time delay between when 90% of the maximum write voltage is applied and when 90% of the maximum response current is read (Figure 12). The response current indicates when the memristor has entered the ON state; the delay between when the write voltage is applied and when the memristor is ON indicates the time it takes to write to the memristor. With ten replicates, the average write speed is observed at 80 ± 60 ns, within range of the write speeds observed in the thin-film device (50 ± 20 ns).[66]

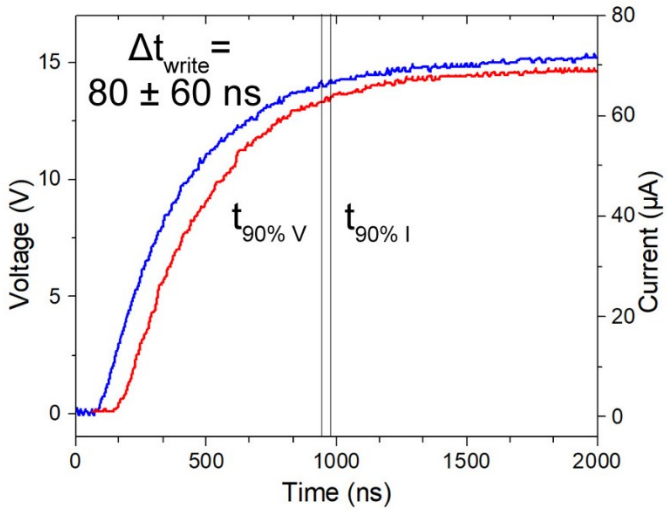

Figure 12: Write speed characteristics of a single write step for the PDMS composite memristor.

2.2.5 Summary

In conclusion, the device properties of a Cu-SiO_2 NW-PDMS composite had properties as a vertical resistive switching cell that are comparable to that of a Cu-SiO_2 NW thin film coated as a horizontal resistive switching cell. Given the success in the manufacturing this preliminary device, we moved forward into the manufacturing of a fully printed memory device, observing the consistency between individual switching cells in the memory array, and integrating the memory array into a practical circuit.

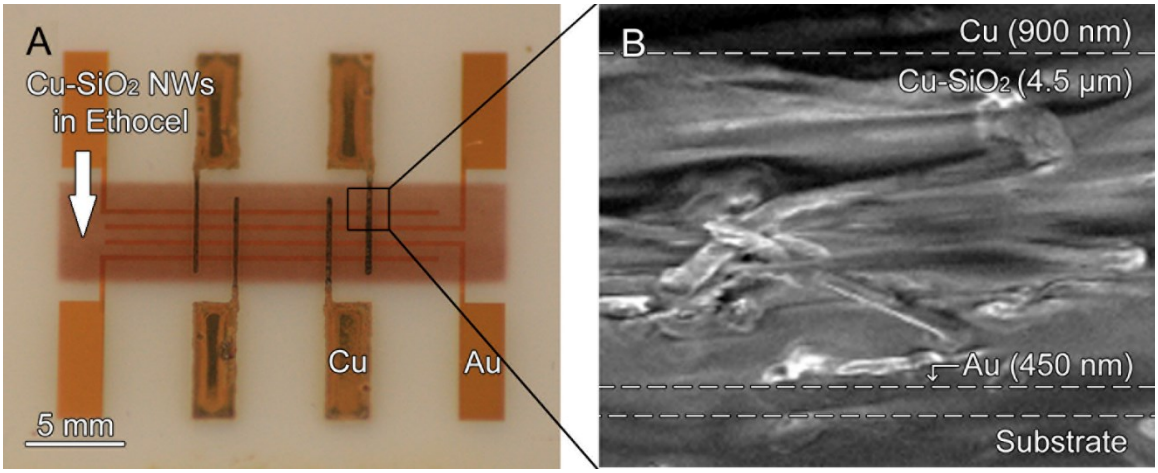

Figure 13: Imaging of fully printed memristor array. (A) Photograph of device with (B) SEM image of a cross-section of the composite film.

2.3 Fully Printed Device Properties

2.3.1 Device Imaging

Figure 13A shows the final crossbar array consisting of 16 individual memristors printed on glass. Figure 13B displays an SEM image of a cross-section of one of the memristors, showing the nanowires embedded within the composite switching layer.

Overall, the printing procedure was successful in emulating the PDMS-composite device, as all printed layers were capable of wetting atop one another and maintaining coherent lines and films after each printing and annealing step.

2.3.2 Resistive Switching

Figure 14A shows the I-V characteristics during the forming step of one memristor on the fully printed device, and Figure 14B shows the a typical I-V curve for bipolar resistive switching of the device. This device is capable of both forming at 9 V and reversible resistive switching at the same compliance current used for testing in Figure 8, illustrating the functionality of the fully printed device as a memristor.

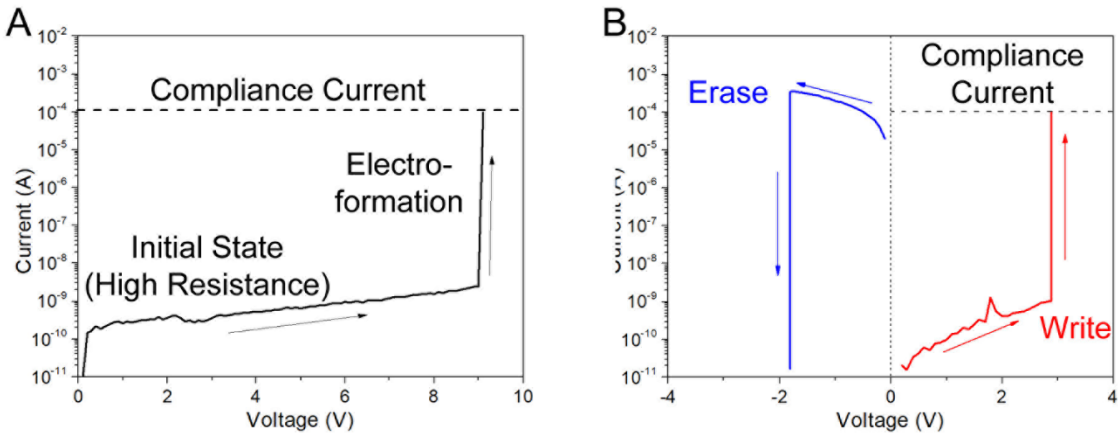

Figure 14: Performance of a fully printed memristor during forming and cycling (A) Plot of the current and voltage in the memristor during forming. (B) Plot of the current and voltage in the memristor during erasing and writing.

Figure 15A shows the average and standard deviation of the switching voltages for every memristor in the 16-memristor crossbar device. Each memristor was cycled

multiple times, and each exhibited moderate operating voltages, with average writing voltages ranging from 1.8 V to 6.3 V, and average erasing voltages between -1.0 V to -5.1 V. Figure 15B shows the cumulative switching voltages, summing the 20 cycles over all 16 memristors (n=320). The average write voltage across all memristors was 3.4 ± 1.8 V, with a maximum of 10 V. The average erase voltage was -2.8 ± 2.2 V, with a maximum of -9.0 V. Relative to the PDMS-composite device, there is no significant difference in performance in regards to writing and erasing voltages.

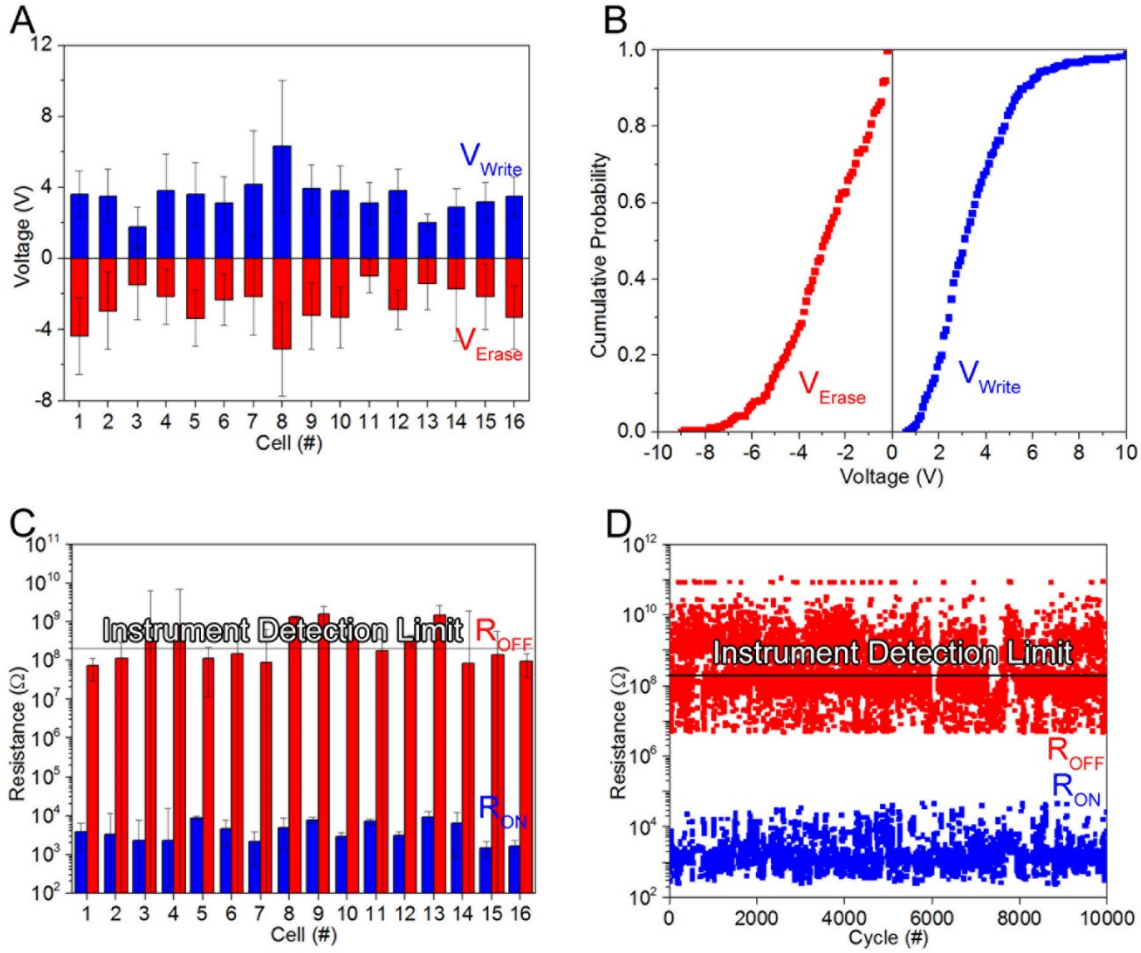

Figure 15: Cycling behavior of the fully printed memristor array over multiple cells. (A) Average write and erase voltages (n=20) in each memristor of the 16-memristor crossbar. (B) Cumulative probability of write and erase voltages (n=320) over all memristors. (C) Average ON and OFF resistances (n=20) in each memristor of the 16-memristor crossbar. (D) ON and OFF resistances over 10^4 switching cycles showing no degradation in performance.

Figure 15C shows the average ON and OFF resistances of each memristor in the crossbar device. The average ON resistance across all 16 memristors was 4.4 kΩ, with the individual average ON resistances ranging between 1.5 kΩ to 9.4 kΩ. Across all 16

memristors, the average OFF resistance was above the instrument detection limit of 200 MΩ. The lowest average OFF resistance measured for a single memristor was 73 MΩ, resulting in a minimum R_{OFF}/R_{ON} of 10^4. Figure 15D shows that the memristor is capable of switching with $R_{OFF}/R_{ON} > 10^5$ over 10^4 cycles with no observable degradation. We stopped testing at 10^4 cycles due to time limitations (one such test takes 10 days), but given the lack of degradation, it appears the endurance may be higher than 10^4 cycles. This confirms the previous hypothesis of extended cycling endurance of the PDMS-composite device, as it also matches the endurance of the thin-film memory.[66]

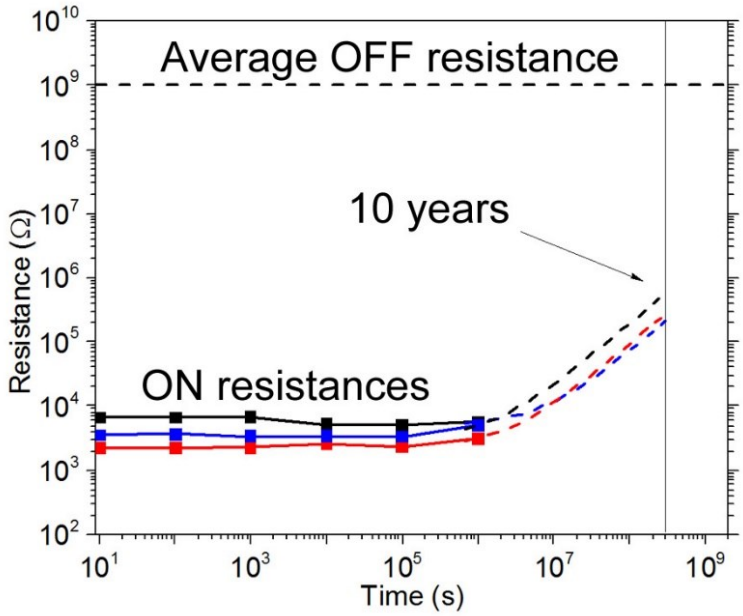

Figure 16: Plot of ON resistances versus time over three separate devices. A linear extrapolation of the data (dotted lines) suggests that the device will retain the ON state for at least 10 years.

2.3.3 Retention

Three devices were tested for retention of the ON state over time in air at room temperature (Figure 16). Over three different memristors, the ON state was read periodically with a 100 mV read voltage over the course of 10^6 s. The memristors retained the ON state and showed negligible degradation over this period. Linearly extrapolating the data out to 10 years, a method that has been previously employed to estimate retention times,[97-98] shows the ON state resistance will remain at least 10^3 times lower than the OFF state resistance. This is a significant improvement over the retention time of 4 days observed in the thin-film memory,[66] and may be due to the presence of the ethylcellulose reducing the diffusion of air into the resistive switching layer.

2.3.4 Write Speed

The average write speed of the fully printed device was characterized by measuring five replicates across five different memristors (n=25). The average write speed was determined to be 2.6 ± 2.0 μs over the 25 replicates (Figure 17A), and the average write speed of each of the five tested memristors was determined to be consistent, with averages ranging from 1.7 μs to 4.3 μs (Figure 17B). Although this result is slower relative to the thin-film and PDMS-composite devices, this write speed is faster than all but one previously reported fully printed memory, and is comparable to the write speed of Flash memories.

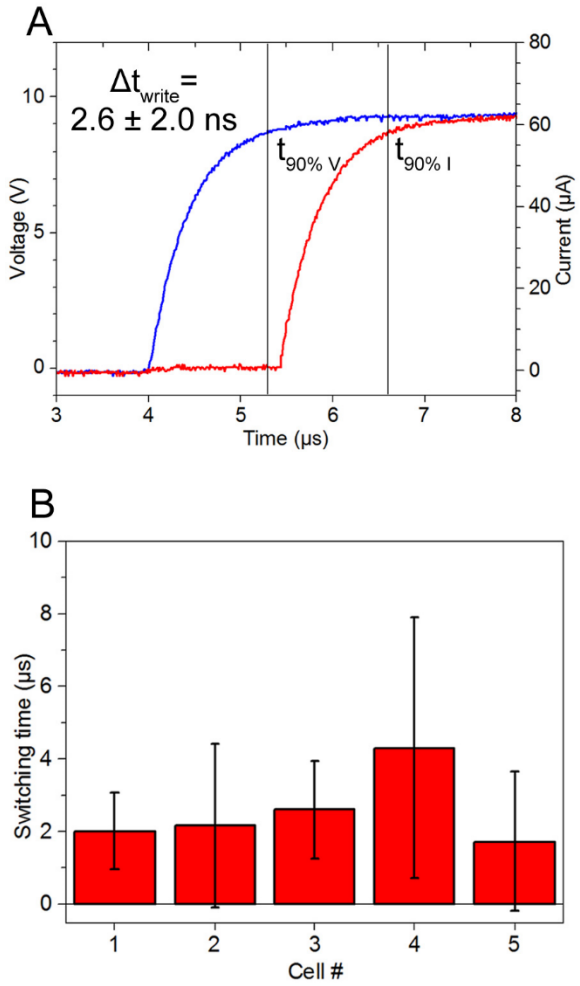

Figure 17: Write speed characteristics of the fully printed memory. (A) Characteristic of a single write step. (B) Averages and standard deviations of switching speed (n=5) in five different memristors.

2.3.5 Circuit Integration

To illustrate how these fully printed memristors might be used in a practical device, we integrated them into a circuit that allowed their ON state to be visualized with an LED. Instead of the crossbar array we used a set of four memristors in parallel to act as a 4-bit memory. We did not use the crossbar array because of the presence of

sneak paths, which is a known issue for memristors fabricated in such a geometry.[99-103] The ability to write or read a memristor in a high-resistance state can be inhibited by neighboring memristors in low-resistance states, which allow the current to flow around the high-resistance memristor. This leads to reading and writing errors. Figure 18A illustrates the circuit diagram used to program the 4-bit memory, and Figure 18B shows a photograph of the programming circuit connected to the device. All 16 programming states of the 4-bit memory are shown in binary in Figure 18C. These states were set with a 5.0 V write voltage from an Arduino, and read with 0.7 V in parallel across all the memristors. In the ON state, the memristor allows the 0.7 V bias to turn on the gate of a transistor, which in turn turns on an LED. While simple, this example of lighting LEDs illustrates successful programming and ON state retention in an actual circuit. A more practical use might be to send the 4-bit output to a BCD-to-7-segment display driver, which in turn could control a 7-segment LED to communicate the price of an item on a shelf. Alternatively, the 4-bit output could be fed to a 4-to-16 multiplexer for a multitude of applications.

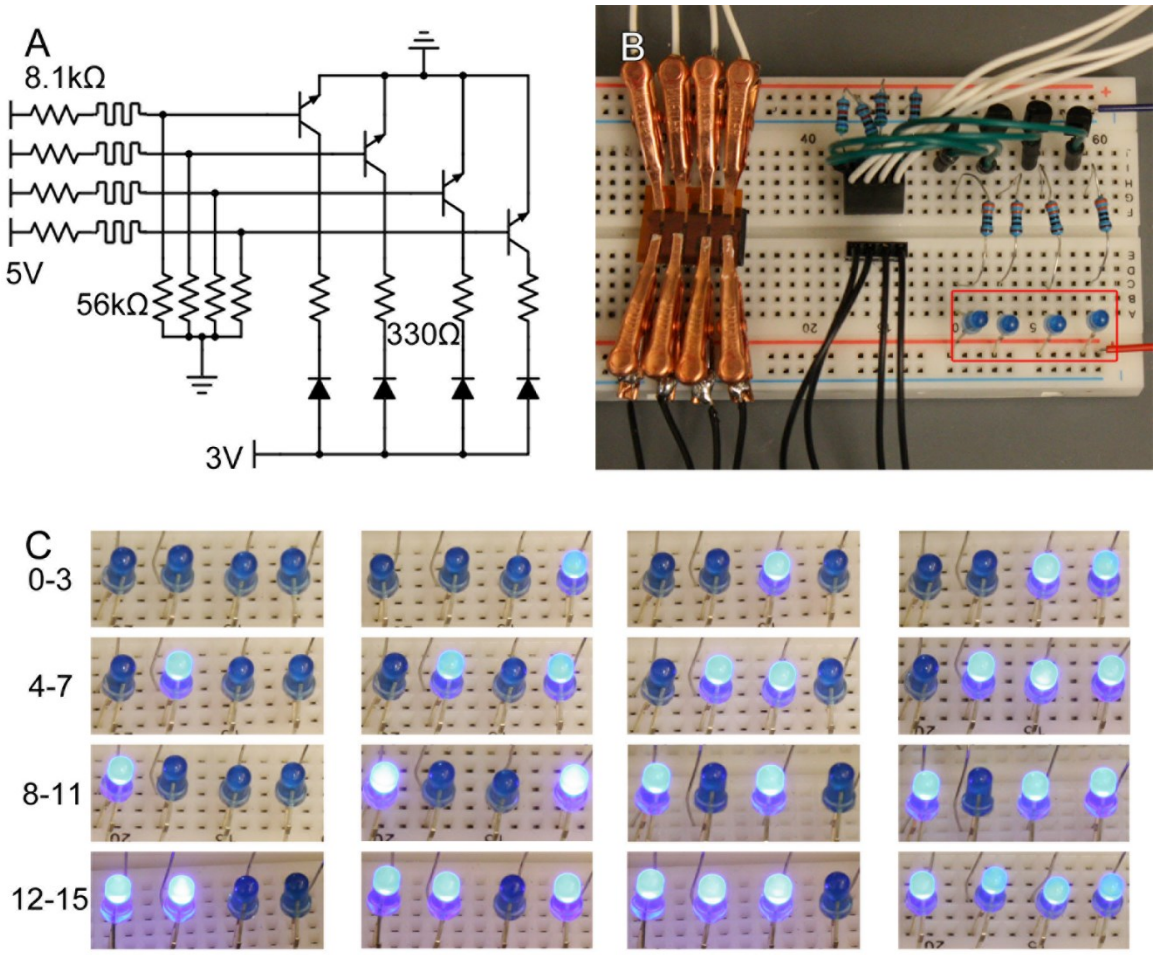

Figure 18: Example circuit utilizing a 4-bit fully printed memristor. (A) A circuit diagram and (B) photograph of the programming circuit. LEDs are highlighted in red. (C) LEDs illustrating the programmed states of the 4-bit memristor. Numbers indicate the binary numbers programmed in each row.

2.3.6 Summary

In summary, Chapter 2 details the progress made from the fabrication of a thin-film, solution-coatable memory into a fully printed array of memristors, in large part due to an ink manufactured using Cu-SiO_2 NWs derived from a large-scale synthesis. Even as a fully printed device, excellent overall performance metrics are observed

relative to the thin-film memory and other fully printed memory devices: write/erase voltages of 3 V / -3 V, endurance of >10^4 cycles, a retention time >10 years, and a write speed of 3 μs. No previous fully printed memory has exhibited such a combination of excellent performance characteristics. The memory can be easily written with 5 V and read with 0.7 V, making it compatible with standard microcontrollers. Future work might explore the integration of fully printed diodes into the crossbar architecture to eliminate sneak paths, or interfacing with fully printed transistors to enable the addressing of larger memory arrays. Additionally, the gold electrodes may potentially be replaced by an alternate inert electrode, such as electrodes deposited using a carbon or carbon-nanomaterial based ink, as to reduce the maximum temperature required for device manufacturing, which allows for the printing on more sensitive substrates.

3. Conductive Stretchable Composites

Recent developments in our laboratory have led to a procedure allowing for a multigram synthesis of Cu-Ag NWs, which when the NWs are vacuum filtered, form a 3D, free-standing NW felt. Because of known procedures to infiltrate free-standing conductive NW networks with elastomer to manufacture stretchable conductive composites, we investigated the performance and properties of the NW felt infiltrated with PDMS as a conductive stretchable composite with a much higher density than previously made infiltrated composites. Additionally, in order to gain a better understanding of the mechanical and electrical behavior of the composite under strain,

multiple observations were made regarding how the NWs behaved during stretching, how NW-matrix interactions may play a role in conductivity effects under strain, and how the stiffness of the elastomer used plays a role in these interactions.

3.1 Manufacturing of Composites

3.1.1 Cu-Ag NW synthesis

Cu-Ag NWs were synthesized via a two-step protocol. In a 10 L bottle, 800 mL of 0.1 M copper (II) nitrate hemi(pentahydrate), ($Cu(NO_3)_2 \bullet 2H_2O$, Sigma-Aldrich ≥98.0%), 115 mL ethylenediamine (EDA, Sigma, ≥99%), and 7.5 L of 8 M sodium hydroxide (NaOH, NOAH Technologies, 99%) solutions were mixed together. Next, 750 mL of 1 g/mL α-D-glucose (Sigma-Aldrich, 96%) solution was added, and the bottle was shaken for one minute. The bottle was then immediately placed in a 60 °C water bath for 1 hr to grow Cu NWs. After the synthesis was complete, the Cu NWs were vacuum filtered using a Buchner funnel and a cloth filter, and rinsed with a solution of 3 wt% 10k MW polyvinylpyrrolidone (PVP, Sigma-Aldrich) and 1 wt% N,N-diethylhydroxylamine (DEHA, TCI America, >95.0%) (PVP/DEHA). After filtration, the Cu NW slurry was rinsed off the filter into a 500 mL solution of PVP/DEHA for resuspension. The Cu NWs were then centrifuged at 2000 rpm for 10 min to concentrate and further rinse the NWs, after which they were resuspended in 250 mL of fresh PVP/DEHA solution. This centrifugation process was repeated three times, and the Cu NWs were kept in 250 ml of a PVP/DEHA storage solution. The concentration of the

product solution was measured with a Perkin Elmer 3100 Atomic Absorption Spectrometer. The observed concentration of the solution was 14.5 mg/mL for a total mass of approximately 3.6 g of Cu NWs.

The Cu NWs were subsequently coated with Ag to form Cu-Ag NWs with a mole ratio of 0.85:0.15 Cu:Ag. The 250 mL solution of Cu NWs in storage solution was diluted with distilled water to 800 mL. This solution was stirred with 1.6 L of 2 wt% PVP in water, and 4.4 L of 1 M ascorbic acid (Duda Energy >99.0%) in water. Then 400 mL of 0.025 M silver nitrate ($AgNO_3$, Fisher Scientific, ≥99.7%) in water was added dropwise to the stirred solution for 10 minutes. After the addition of $AgNO_3$ was complete, the reaction was left to stir for 10 minutes, the stirring was turned off to allow the NWs to settle overnight. The reaction vessel was then decanted to remove excess solution, and the remaining NWs were rinsed with DI water and centrifuged at 2000 rpm for 5 minutes three times to concentrate the NWs into 800 mL of PVP/DEHA storage solution. The average Cu-Ag NW length was 41 ± 14 μm and the average diameter was 240 ± 67 nm.

3.1.2 Filtration and Infiltration

Filtration was performed using a Millipore vacuum filter funnel. Nanowires were filtered through a silicone gasket (Fuel Cell Store) onto a 400 x 400 stainless steel wire cloth (McMaster Carr). An ASTM D412 test specimen, with schematic provided in Figure 19, and a serpentine circuit pattern were cut into the gasket with an Epilog Fusion

60W laser cutter. For filtration, 6 mL of the Cu-Ag NW storage solution was diluted with 40 mL of H_2O and poured through the filter to make a 250-μm-thick Cu-Ag NW felt. The Cu-Ag NW felt was annealed in an oven at 150 °C for 30 minutes, and transferred from the cloth to a Teflon sheet in a petri dish. Samples were infiltrated with a 2:1:1 solution of MEK, PDMS precursor Part A, and PDMS precursor part B. The PDMS precursors Ecoflex 00-30 and Dragon Skin 30 were provided from Smooth-On Inc. The samples were infiltrated for 30 min under ambient conditions, followed by vacuum infiltration for 3 h in a desiccator to allow for solvent evaporation and curing of the PDMS. Scanning electron microscope images of the felt and the infiltrated composite were taken using an FEI XL30 SEM.

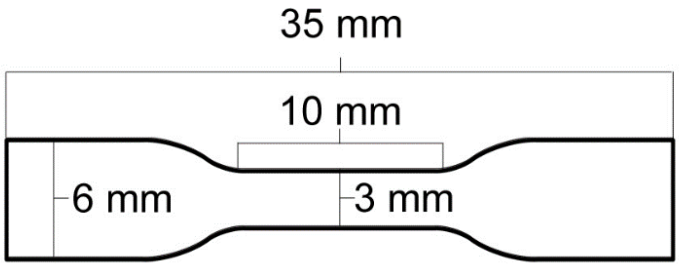

Figure 19: Schematic and dimensions of the ASTM D412 test specimen.

3.1.3 Electrical and Strain Characterization

The electrical conductivity of infiltrated and non-infiltrated samples was measured using a four-point probe, and calculated by multiplying the measured sheet resistance by the sample thickness. Stress-strain tests were performed using a micro-strain analyzer (MSA, TA Instruments RSA III). Electrical characterization during strain was observed using a Keithley 2401 SourceMeter with LabView 2016 software. In order to establish contact with the sample in the MSA, the handles of the test specimen were coated in colloidal silver paste (Electron Microscopy Sciences), and sandwiched with copper foil to establish electrical contact. Two pieces of silicone gasket were used to electrically isolate the sample from the metal clamps of the MSA. Stress-strain measurements were performed at a rate of 1% strain per second. Cycling tests were performed at a strain rate of 20% per second, and the resistance was recorded while the sample was held at the minimum (0%) and maximum (50% or 100%) strain for five seconds. The position at which the strain was 0% for all cycles was defined as the starting position of the MSA for the initial strain test, even for samples that underwent plastic deformation during cycling. Plastic deformation and time dependent behavior studies were performed at a rate of 20% strain per second, holding at a strain of 100% for 5 seconds.

3.1.4 Device Manufacturing

For the LED circuit, a layer of stretchable, 80% nylon, 20% spandex fabric (Rex Fabrics) was placed between the patterned silicone gasket and the metal cloth during the vacuum filtration procedure. Cu-Ag NWs were filtered onto the fabric, and were annealed after filtration. The fabric and patterned NWs were immersed in Ecoflex in a Teflon well, and vacuum infiltrated for 30 min, followed by 30 min in a 60 °C oven to cure the PDMS. The LEDs were powered using an external power supply with a compliance voltage of 7 V and a compliance current of 15 mA.

3.2 Composite Properties

3.2.1 Fabrication and Conductivity

The procedure for composite manufacturing is illustrated in Figure 20A. Cu-Ag nanowires were first synthesized as described previously and in the experimental section.[16, 91] The nanowires were filtered through a rubber gasket onto a metal cloth to form dogbone-shaped test specimens according to ASTM D412 for tensile testing. The length, width and thickness of the test specimens were 10 mm, 3 mm, and 250 μm, respectively. The average density of the nanowire felt prior to infiltration (Figure 20B) over three replicates was 0.87 ± 0.04 mg/mL. This density corresponds to a porosity of 90.5 ± 0.4% based on a weighted average of the densities of Cu (85%) and Ag (15%). After filtration, the NWs were annealed and infiltrated with PDMS (Figure 20C).

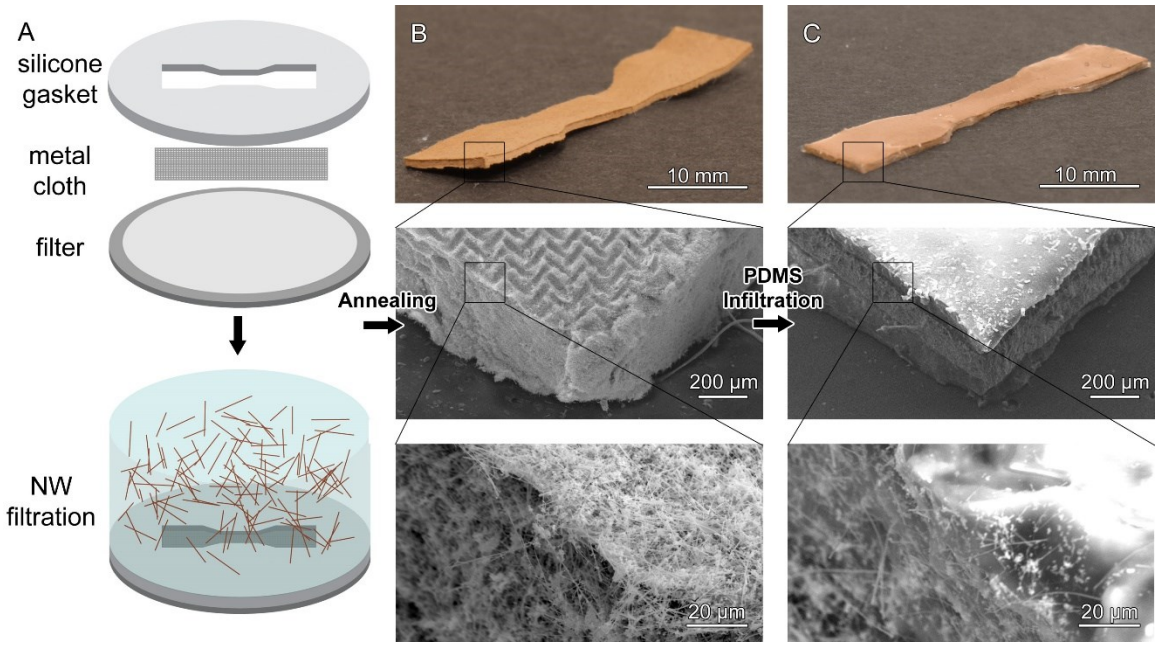

Figure 20: Procedure for stretchable conductive composite manufacturing (A) Cu-Ag NWs were filtered through a silicone gasket onto a metal cloth to create a NW felt in the shape of the hole in the gasket. (B) Photograph and SEM image of felt after annealing and (C) after PDMS infiltration.

In order to maximize the conductivity of the composite, the NW felts were annealed at a variety of temperatures for 30 minutes to determine which temperature yielded the highest conductivity prior to infiltration (Figure 21). An annealing temperature of 150 °C resulted in the highest conductivity (2040 ± 35 S cm^{-1}). This conductivity is 1.6 times higher than the air-dried sample before annealing (1270 ± 610 S cm-^{1}). The conductivity of the annealed NW felts is only 28 times less conductive than Cu with a porosity of 90% (5.8*10^{4} S cm-1). After infiltration, 40% decrease in electrical conductivity was observed (1220 ± 630 S cm-1), likely because the insulating elastomer

increased the contact resistance between the four-point probe and the conductive filler. However, this conductivity is still only 47 times less conductive than bulk Cu at a similar porosity, and is comparable to previous results with Ag MFs at filler loadings double that of the Cu-Ag NW composite (Figure 4A). The infiltrated Cu-Ag NW network is also four times more conductive than identical Cu-Ag NWs blended into polycaprolactone at a similar concentration (12 vol%).[16]

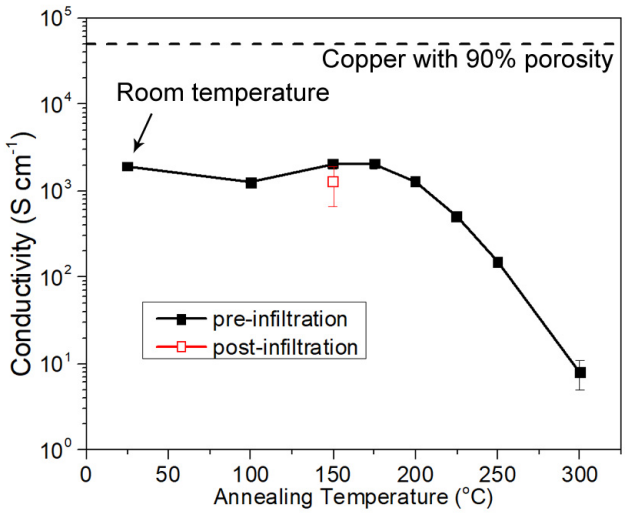

Figure 21: Conductivity of Cu-Ag NW felts vs. annealing temperature , and conductivity after PDMS infiltration. The dotted line indicates the conductivity of bulk Cu with a porosity identical to the composite.

3.2.2 Effect of Matrix Stiffness on Conductivity as a Function of Strain

In order to examine the effect of the stiffness of the elastomer matrix on the ability of the composite to retain its conductivity under strain, the Cu-Ag NW felt was

infiltrated with relatively low-stiffness and high-stiffness PDMS elastomers at different ratios. The low-stiffness PDMS is Ecoflex 00-30 (0.07 MPa at 100% strain), and the high-stiffness PDMS is Dragon Skin 30 (0.59 MPa at 100% strain). We will hereafter refer to these materials as Ecoflex and Dragon Skin. Figure 22A shows that, before infiltration, the annealed Cu-Ag NW network is very brittle. Fracture initiates at 1.5% strain and is complete at approximately 4% strain. After infiltration with PDMS, the composite does not fracture until strains of 250-350% (Figure 22B). Figure 22B also shows that the presence of the NW network within PDMS greatly increases its stiffness. Compared to the pure version of the elastomer, the stiffness of the Dragon Skin and Ecoflex composites increased by a factor of 3.4 and 13, respectively. These mechanical tests illustrate the Cu-Ag NW felt infiltrated with PDMS exhibits a stiffness closer to that of the nanowire felt than that of the elastomer, even though the nanowires comprise only 10% of the volume of the composite. Thus, it seems that the deformation of the nanowire network within the elastomer may be dominating the stress-strain behavior of these materials. In addition, it is clear that the presence of the elastomer matrix prevents fracture and breakup of the nanowire felt, facilitating its deformation under an applied stress.

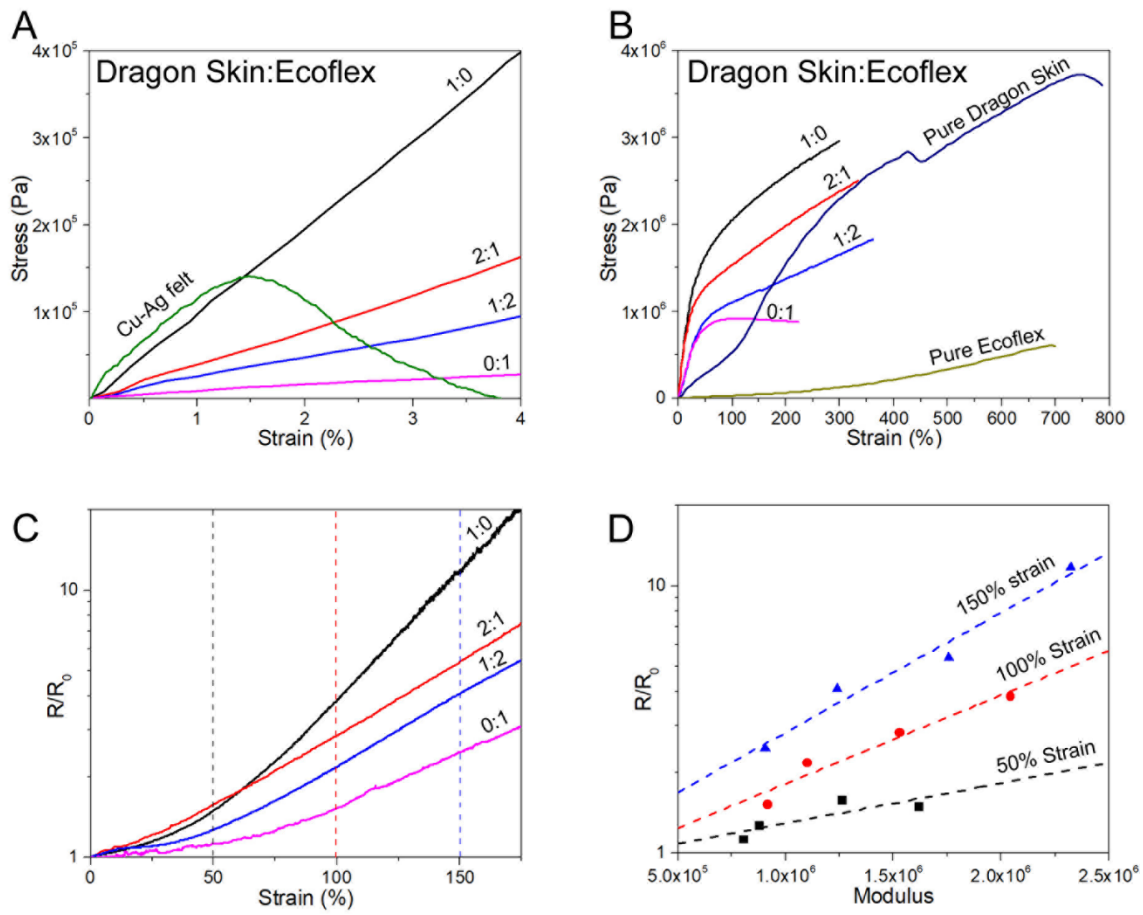

Figure 22: Stiffness vs. conductivity behavior of stretchable conductive composites (A) Stress vs. strain performance for the Cu-Ag NW felt, as well as various Cu-Ag NW PDMS composites containing different ratios of Dragon Skin to Ecoflex. (B) Stress vs. strain curves for Cu-Ag NW composites. (C) R/R_0 vs. strain for the Cu-Ag NW composites. (D) R/R_0 vs. modulus at 50, 100, and 150% strain.

Figure 22A&B shows that, as expected, the stiffness of the composite increases with the amount of Dragon Skin present in the infiltrated PDMS relative to the amount of Ecoflex. Figure 3C shows that this increase in stiffness had a significant effect on the ability of the composites to retain their initial conductivity under an initial applied

strain. The Ecoflex composite exhibits an increase in resistance, denoted by R/R_0, of only 1.12, 1.52, and 2.46 at strains of 50%, 100%, and 150% respectively. In comparison, the R/R_0 of the Dragon Skin-NW composites is higher, at 1.49, 3.86, and 11.7 at the same strains. With the intermediate blends of Ecoflex and Dragon Skin, intermediate values of R/R_0 were observed. Figure 22D summarizes the effect of matrix stiffness on retention of conductivity by plotting the R/R_0 vs. modulus at strains of 50%, 100%, and 150%. The four modulus values are from Ecoflex, Dragon Skin, as well as the 2:1 and 1:2 blends of Dragon Skin:Ecoflex. This panel illustrates there is a clear tradeoff between the stiffness of the matrix and the conductivity that can be retained as the composite is stretched.

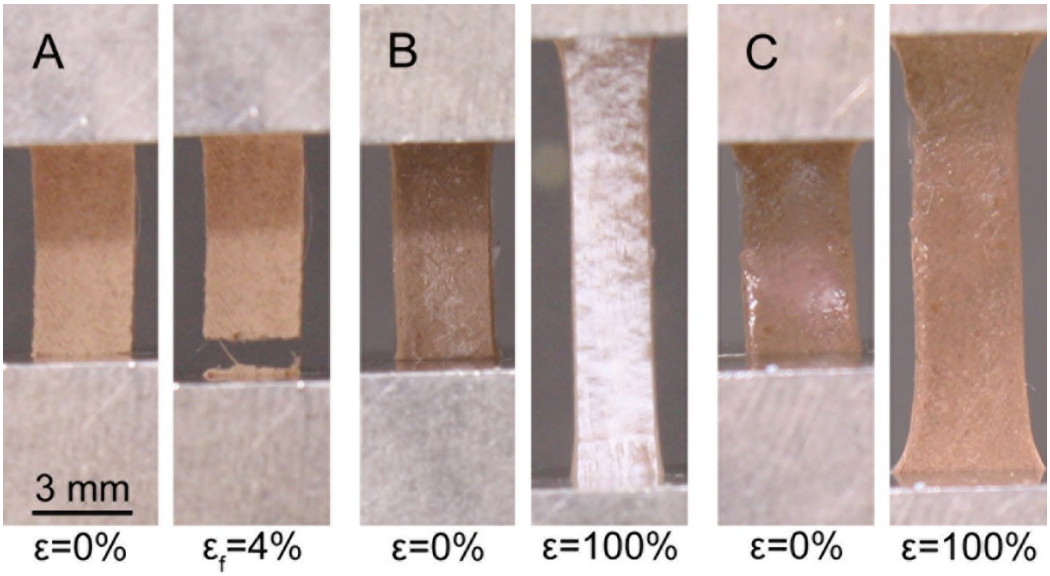

Figure 23: Images showing the difference in the stretchability and void formation for the (A) Cu-Ag felt (B) Dragon Skin-NW composite and (C) Ecoflex-NW composite during the initial strain.

Although there have been many previous studies of the electrical conductivity of PDMS composites, and it has been observed how changing the type or concentration of conductive filler can influence stiffness and electrical properties,[104-110] we found no previous studies on the effect of the stiffness of the elastomer matrix on the ability of the composite to retain its electrical properties under strain. In order to gain further insights into the mechanism of this phenomena, we examined whether there was any difference in the mechanism of deformation for Dragon Skin and Ecoflex composites. Figure 23 displays photographs of the Cu-Ag felt, the Dragon Skin composite, and the Ecoflex composite at 0 and 100% strain. As seen in Figure 23A, the Cu-Ag NW felt without PDMS is brittle and fractures at low strain. The Dragon Skin composite (Figure 23B) turns from orange to white under strain, while no obvious color change was observed for the Ecoflex composite (Figure 23C). This suggested the Dragon Skin composite formed voids under strain, while the Ecoflex composite did not. This difference in deformation response was confirmed with SEM imaging. Figure 24A&D show both the Ecoflex and Dragon Skin composites appeared to be free of voids initially. Although nanowires appeared to align in both composites at 100% strain (Figure 24B&E), only the Dragon Skin contained a large amount of voids in the strained state. When the Ecoflex was brought back to a strain of 0%, there were no noticeable voids present within the composite. In contrast, the voids were retained in the Dragon Skin composite and became buckled as it was relaxed to a strain of 0% (Figure 24F).

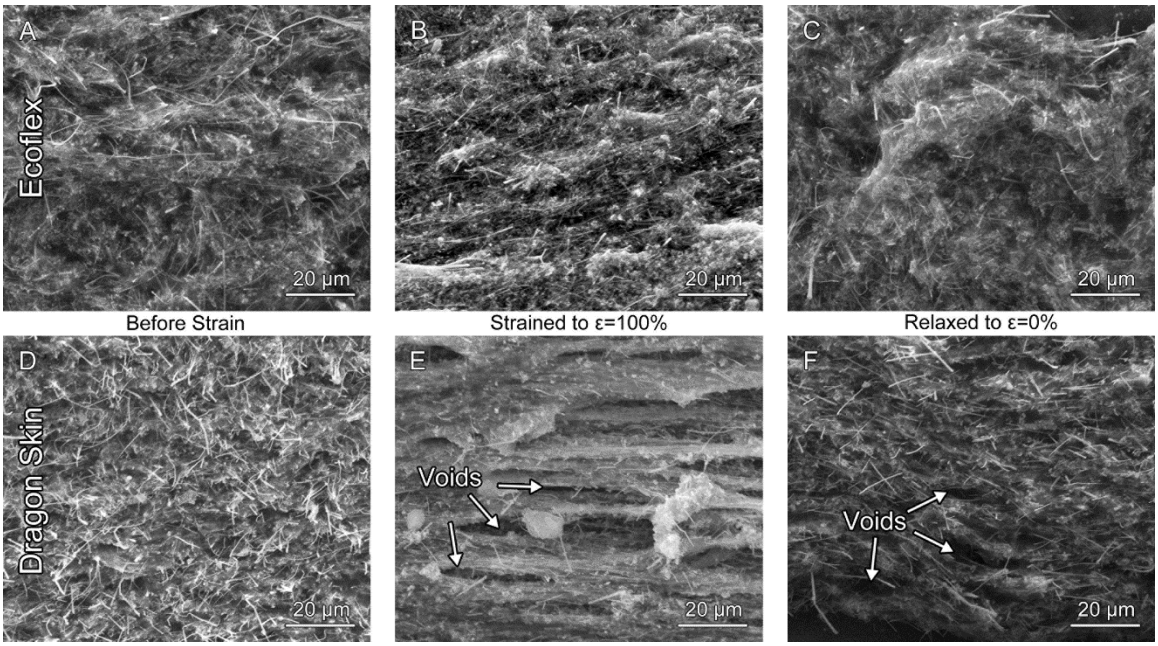

Figure 24: SEM images of the Ecoflex and Dragon Skin composites (A&D) before strain, (B&E) at 100% strain, and (C&F) after relaxation back to 0% strain. Voids are present in the Dragon Skin composite, but not in the Ecoflex composite.

These observations suggest that the reason for the greater decrease in conductivity as a function of strain for composites containing stiffer PDMS is due to the formation of voids. Gent and Park previously studied the effect of elastomer stiffness on the formation of voids through cavitation and debonding in elastomers with rigid spherical inclusions.[111] They found that while the stress required for cavitation (expansion of microvoids) increases with increasing Young's modulus, the stress required for debonding decreases with increasing Young's modulus. This was attributed to the fact that lower-modulus materials are able to dissipate more energy during debonding through viscoelastic energy losses that occur during deformation of the

sample.[112] Thus, the fact that Ecoflex is eight times less stiff than Dragon Skin may result in a stronger interfacial adhesion between the PDMS and the Cu-Ag NWs. This stronger adhesion may prevent void formation during debonding, and thus improve the retention of conductivity under strain for the Ecoflex composite.

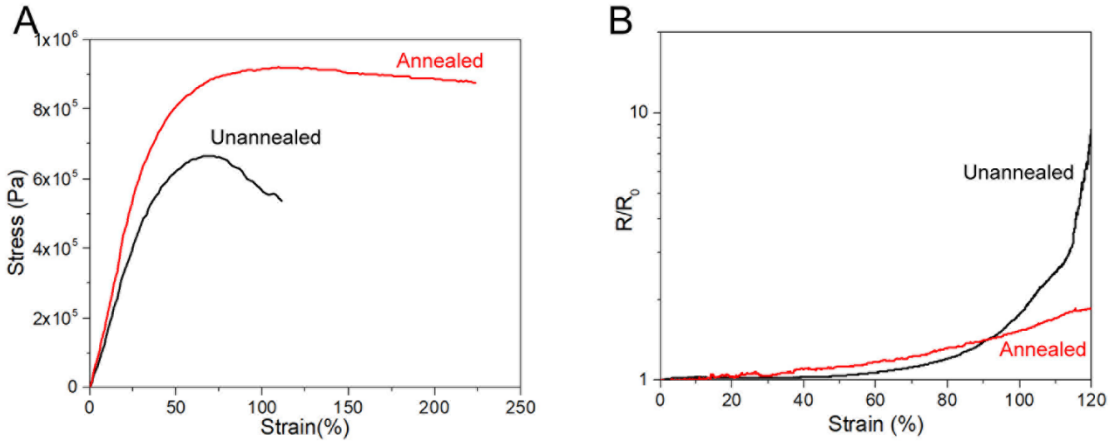

Figure 25: Comparison of stretchable conductive composites and annealing condition. (A) Stress vs. strain behavior for Ecoflex-NW composites using NW cakes that were air-dried and annealed at 150 °C. (B) R/R_0 vs. strain behavior for annealed vs. unannealed composites.

An additional test was performed as to observe if a Cu-Ag NW felt that was not annealed would have different stress vs. strain and R/R_0 vs. strain properties relative to the annealed Cu-Ag NW felt when in the Ecoflex-based composites. The unannealed composite was manufactured by the same procedure detailed in Chapter 3.1.2, except instead of annealing at 150°C for 30 minutes, the Cu-Ag NW felt was air-dried under ambient conditions for 1 hour before infiltration with PDMS. As seen in Figure 25A, the unannealed composite is noticeably less stiff than the annealed composite, as observed

with a shallower slope in the stress vs. strain curve during the initial 50% strain. Likewise, this composite had better R/R_0 under the same initial strain (Figure 25B), which correlates with the results seen in Figure 22 where composites with reduced stiffness have improved R/R_0 vs. strain performance. However, while slight necking is observed in the annealed composite, noted by a decrease in stress with increased strain at high strain, necking effects are more pronounced in the unannealed composite, making it limited in its maximum stretchability. Although the maximum stretchability is reduced in this given composite, there is further evidence to suggest that the R/R_0 vs. strain behavior could be further improved with the use of an even lower-stiffness elastomer matrix than the Ecoflex 00-30 used in this study.

3.2.3 Composite Cycling

The Dragon Skin and Ecoflex composites were cycled 50 times to strains of 50% and 100% to examine how well the composites retained their conductivity over many cycles of stretching (Figure 26A&B). For the cycling to strains of 50%, both the Dragon Skin and Ecoflex composites exhibited an irreversible loss in conductance after the first complete cycle, with an R/R_0 of 1.68 and 1.37, respectively. The resistance at 0 and 50% strain remained fairly stable over subsequent cycles, exhibiting a standard deviation of 0.04 and 0.02 for Dragon Skin and Ecoflex, respectively. We note that, after the first cycle, the resistance was lower in the strained state than for the relaxed state. The ratio between the R/R_0 at 0 and 50% strain was 1.12 ± 0.09 and 1.15 ± 0.05 for the Dragon Skin

and Ecoflex composites, respectively. Overall these composites demonstrated robust cycling durability and a modest change in resistance upon stretching to 50% strain.

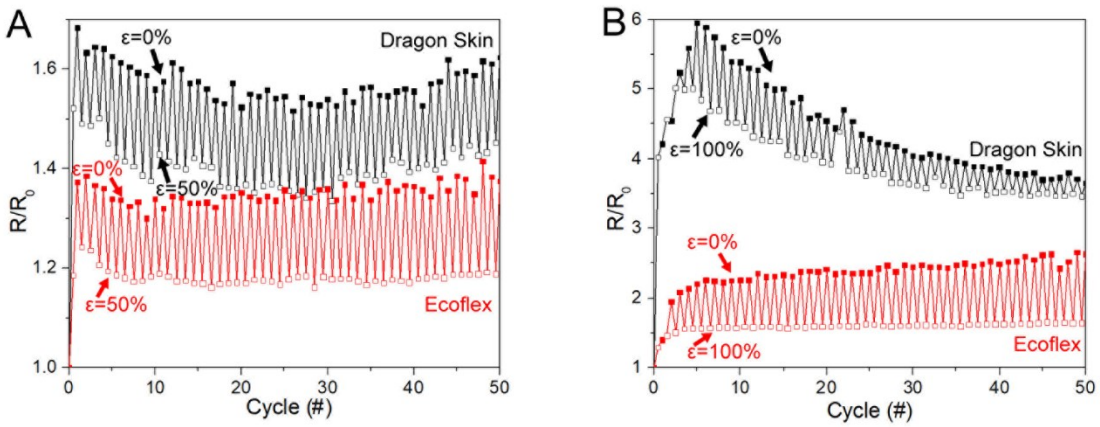

Figure 26: Cycling behavior of the stretchable conductive composites. (A) R/R_0 behavior over 50 cycles at 50% strain and (B) 100% strain

At 100% strain, the Ecoflex composite still exhibits relatively stable resistance, but requires 3 cycles to achieve stable cycling. After 3 cycles, the maximum R/R_0 is 2.65, and the ratio between the R/R_0 for 0 and 50% strain is 1.49 ± 0.06. Significantly different behavior is observed for the Dragon Skin composite. The R/R_0 increases for the first 5 cycles, then subsequently decreases until it becomes fairly stable after 40 cycles. The maximum R/R_0 of the composite (5.94) occurred after the 5th cycle; the R/R_0 max decreases to 3.64 at 0% strain after the 50th cycle.

Most previous studies of infiltrated nanowire networks did not observe a higher conductivity in the strained state after cycling, but we are using much higher concentrations of conductive material (~10 vol%) than was used in those previous

studies (<1 vol%). Studies that have observed such phenomena include those that examined the properties of 2 vol% steel wool infiltrated with PDMS,[113] 32 vol% PEDOT:PSS in polyurethane,[114] 48 vol% Ag MFs in bubbled polyurethane,[115] and 63 vol% carbon black in natural rubber.[116] In attempt to provide additional insights into why the conductivity is higher in the strained state for the Cu-Ag NWs and other highly loaded conductive composites, we examined how the stress-strain and R/R_0-strain behavior changed during cycling.

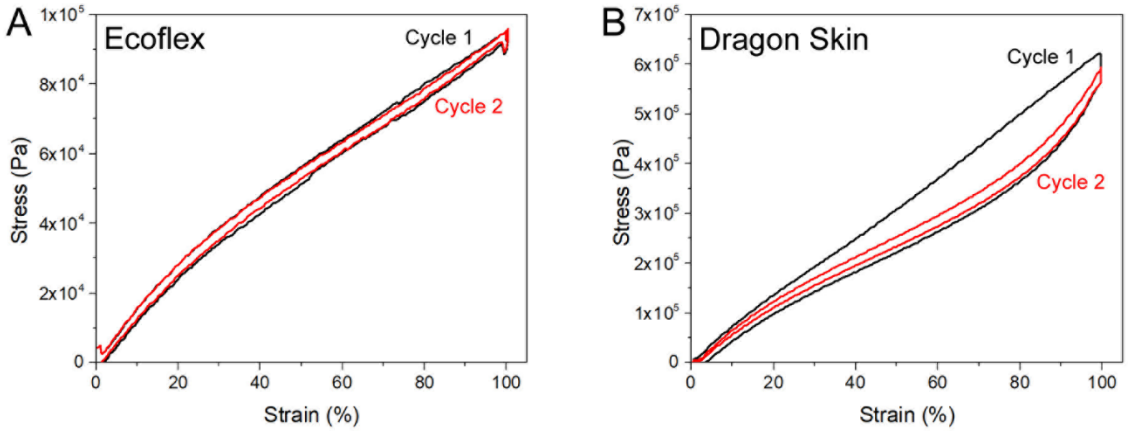

Figure 27: Hysteresis behavior of plain PDMS (A) Stress vs. strain behavior of pure Ecoflex and (B) pure Dragon Skin PDMS over two cycles at 100% strain

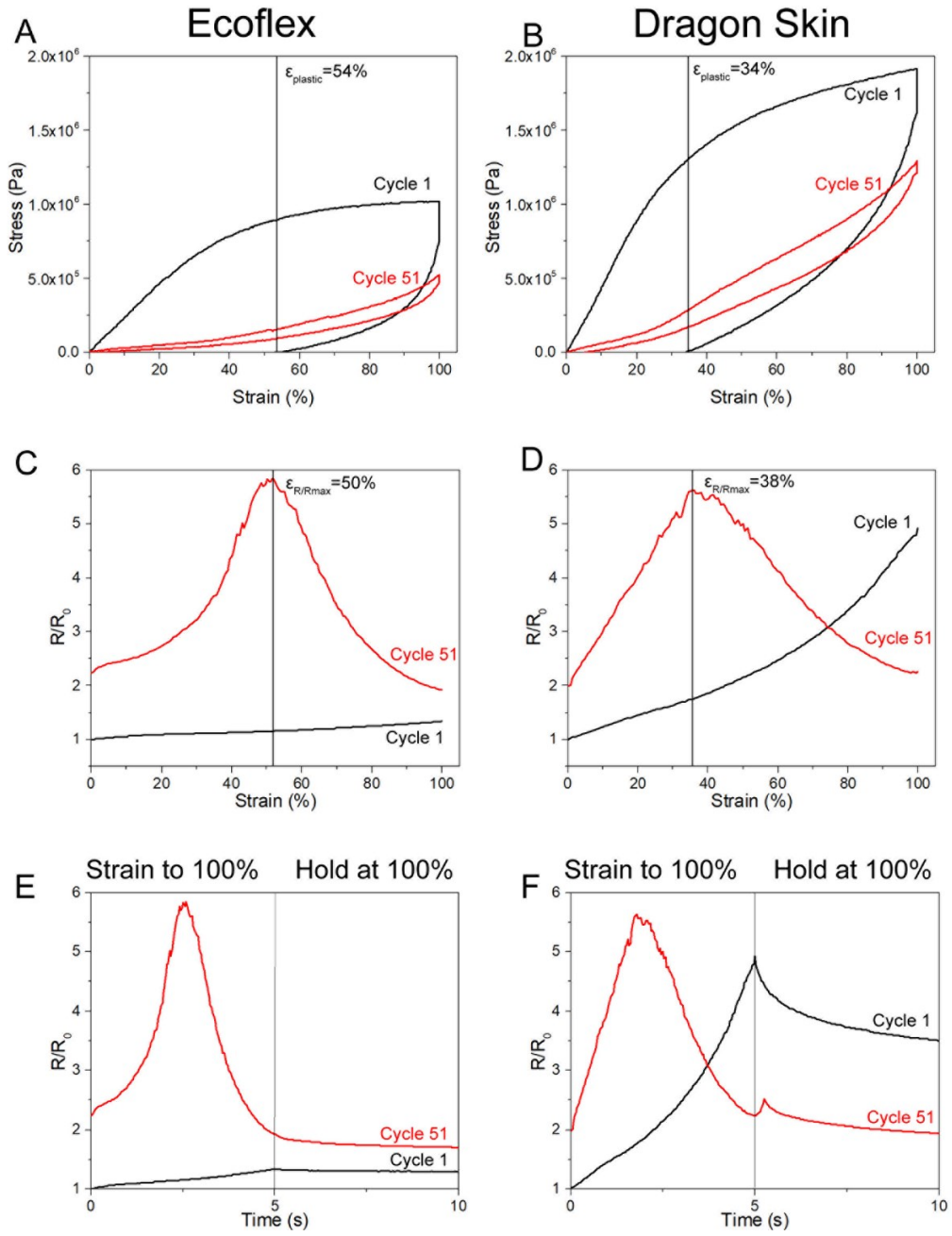

Figure 28: Analysis of composites during strain before and after cycling (A&B) Stress vs. strain curves for Dragon Skin and Ecoflex composites. (C&D) R/R_0 vs. strain behavior for Dragon Skin and Ecoflex composites after the 1st and 51st cycle at 100% strain. (E&F) Time-dependent strain vs. R/R_0 behavior for Dragon Skin and Ecoflex composites after the 1st and 51st cycle at 100% strain.

Figure 27A&B shows the pure Dragon Skin and Ecoflex exhibit little hysteresis during the first two stress-strain cycles, as well as plastic deformations of 4 and 2%, respectively. Figure 28A&B shows that there is a large hysteresis and plastic deformation in the first cycle of stretching for both composites; Ecoflex and Dragon Skin exhibit irreversible strains of 54% and 34%, respectively. In comparison, there is no additional plastic deformation in subsequent cycles, but the composite continued to soften. Such softening is often observed for filler rubbers and is termed the Mullins' effect.[117] There is no consensus as to the mechanism behind the Mullins' effect, and it can vary between composites, but it is often ascribed to sliding of filler material within the composite,[118] and/or debonding between the filler material and the matrix, leading to the generation of voids.[119] The former is difficult to discern, but the latter is obviously occurring in the case of the Dragon Skin composite, as is shown in Figures 24C and 24F.

Figures 28C and 28D show the R/R_0 continuously increases until the maximum strain of 100% during the first cycle. This is consistent with the fact that the R/R_0 increased during the first cycles in Figure 26. By cycle 51, the R/R_0 increases to a maximum of 5.83 at 50% strain for the Ecoflex composite, and a maximum of 5.57 at 38% strain for the Dragon Skin composite. Additional strain to 100% decreased the R/R_0 to 1.92 and 2.25 for the Ecoflex and Dragon Skin, respectively. The strain at which the maximum values of R/R_0 for each composite occurred are nearly identical to the extent of plastic deformation that occurred during the first cycle (54% for Ecoflex, 34% for

Dragon Skin). We hypothesize that as the material is strained from the relaxed state up until the point at which plastic deformation occurred, the buckled voids unbuckle in the Dragon Skin, reducing the overall number of electrical contacts and reducing the conductivity of the material. After the point of plastic deformation up to 100% strain, the voids undergo transverse compression and strands begin to align, increasing the number of electrical contacts and increasing the conductivity of the material. Such behavior was previous observed for a composite with voids containing 48 vol% Ag MFs in polyurethane.[115]

On the other hand, the Ecoflex composite does not contain voids but exhibits nearly identical R/R_0 vs. strain behavior. A study by Yamaguchi *et al.* observed similar conductivity vs. strain behavior for a 63 vol% loaded carbon black in natural rubber, and suggested that the slippage, orientation, and alignment of carbon black aggregates under strain contributed to the enhanced conductivity under strain.[116] Given that the most relaxed state of the Ecoflex composite after the first cycle is the point at which plastic deformation occurred during the first cycle, strains below or above this strain will lead to compression or alignment of the nanowire networks, both of which could conceivably be responsible for the lower R/R_0 at 0% and 100% strain. Therefore, although the mechanisms may differ, for both composites it appears that the alignment of NWs that occurred during the first strain cycle was permanent and made the composite more conductive in the strained state.

3.2.4 Time-Dependent Behavior

The other unusual observation is that the Dragon Skin composite regains some of the conductivity lost during the first 5 cycles of 100% strain, but the Ecoflex remains fairly stable. This effect may be attributed to the time-dependent behavior of the composites. It was previously observed that the resistance of multi-walled CNT-PDMS composites decreased over time when the composite was held at strain, and this behavior was attributed to stress relaxation.[120] We also observe a time-dependent decrease in the R/R_0 for the strained Dragon Skin composite in this study (Figure 28F), but not for the Ecoflex (Figure 28E). The observed drop in R/R_0 after the first 5 cycles for Dragon Skin can be attributed to the decrease in the R/R_0 that occurs over time for this stiffer composite. The difference in time-dependent R/R_0 under strain for Ecoflex and Dragon Skin may be related to the different degree of debonding and void formation observed in these composites. As the Ecoflex composite is strained, the NWs align with the composite during the initial strain, and are held in place when strain is complete. This leads to a minimal decrease in R/R_0 when the composite is held at strain. In contrast, as the Dragon Skin composite is strained, void formation results in a time dependent reordering of the NW network that results in a drop in R/R_0. Gaining additional insights into the mechanism of this process is experimentally challenging due to the difficulties in imaging the time-dependent deformation of a three-dimensional

network of nanowires, as well as calculating what the resistance of the nanowire network should be under various states of strain.

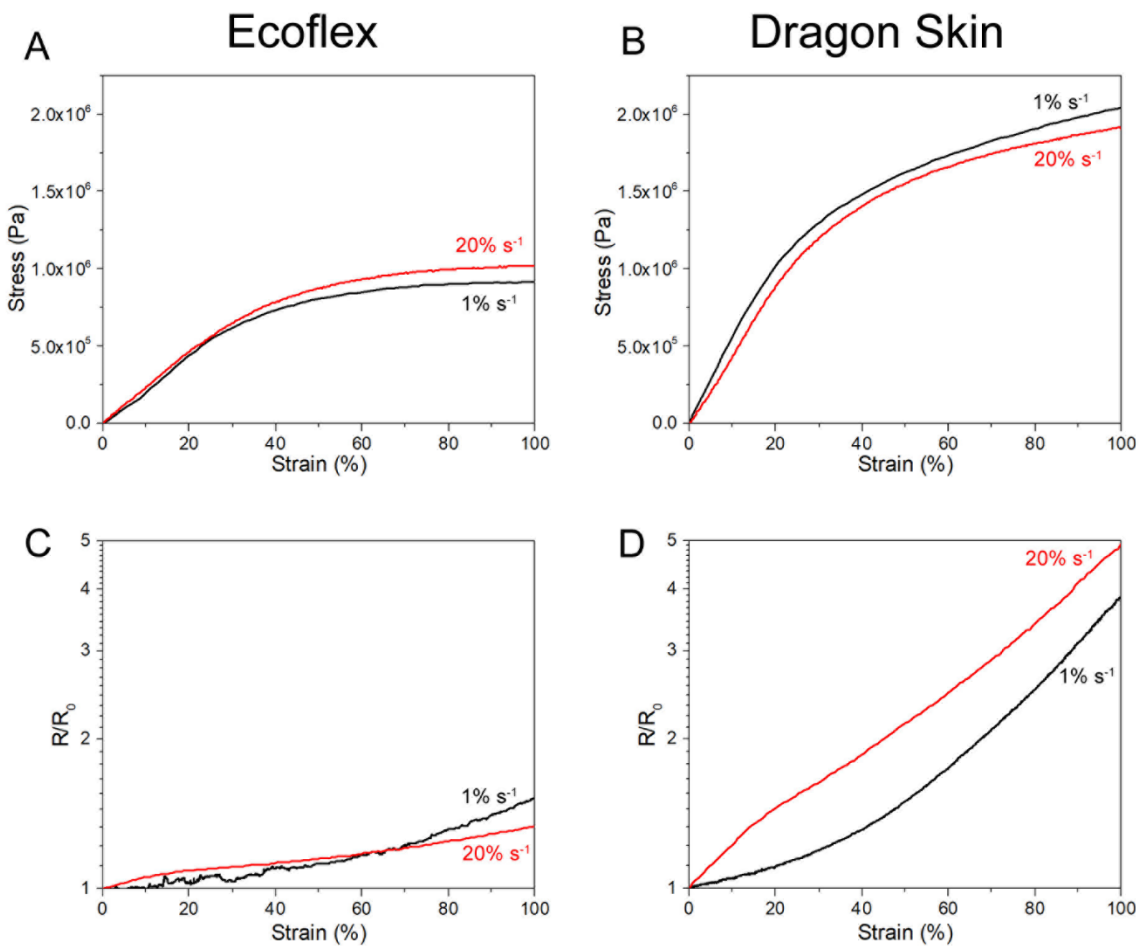

Figure 29: Strain rate dependence on composite behavior. (A) Stress vs. strain curves of the Ecoflex composite and (B) Dragon Skin composite at strain rates of 1% s^{-1} and 20% s^{-1}. (C) R/R_0 vs. strain behavior of the Ecoflex composite and (D) Dragon Skin composite at strain rates of 1% s^{-1} and 20% s^{-1}.

Although the effect of strain rate on the retention of conductivity is important for the practical use of a stretchable conductor, it is a dimension that is rarely explored. For example, the strain rates used in the previous studies listed in Figure 4

vary greatly from 0.08% s^{-1} to 5% s^{-1}, but none of those studies examined the effect of strain rate on the stress and R/R_0 response.[12, 80] Figure 29 shows the effect of strain rate on the stress and R/R_0 for the Ecoflex and Dragon Skin composites. We selected a strain rate of 1% s^{-1} to be in within the range of previous experiments in the literature, and a strain of 20% s^{-1} to more accurately simulate the faster strain rates that would be seen in a wearable device.[72-73, 121-122] The strain rate does not have much effect on the stress vs. strain behavior for both the Ecoflex and Dragon Skin (Figure 29A&B). For the Ecoflex composite, the R/R_0 vs. strain is identical at the two strain rates (Figure 29C&D). However, for the Dragon Skin composite the slope of the R/R_0 vs. strain curve is larger for the 20% s^{-1} strain rate during the first 20% of strain, after which the slopes were similar. This increase in R/R_0 may be associated with the time-dependent effects discussed with respect to Figures 28E&F, as less time is available for the NW network to align and reduce its R/R_0 under high rates of strain. Thus we see that the matrix stiffness can not only affect the static increase in R/R_0, but also its time-dependent behavior.

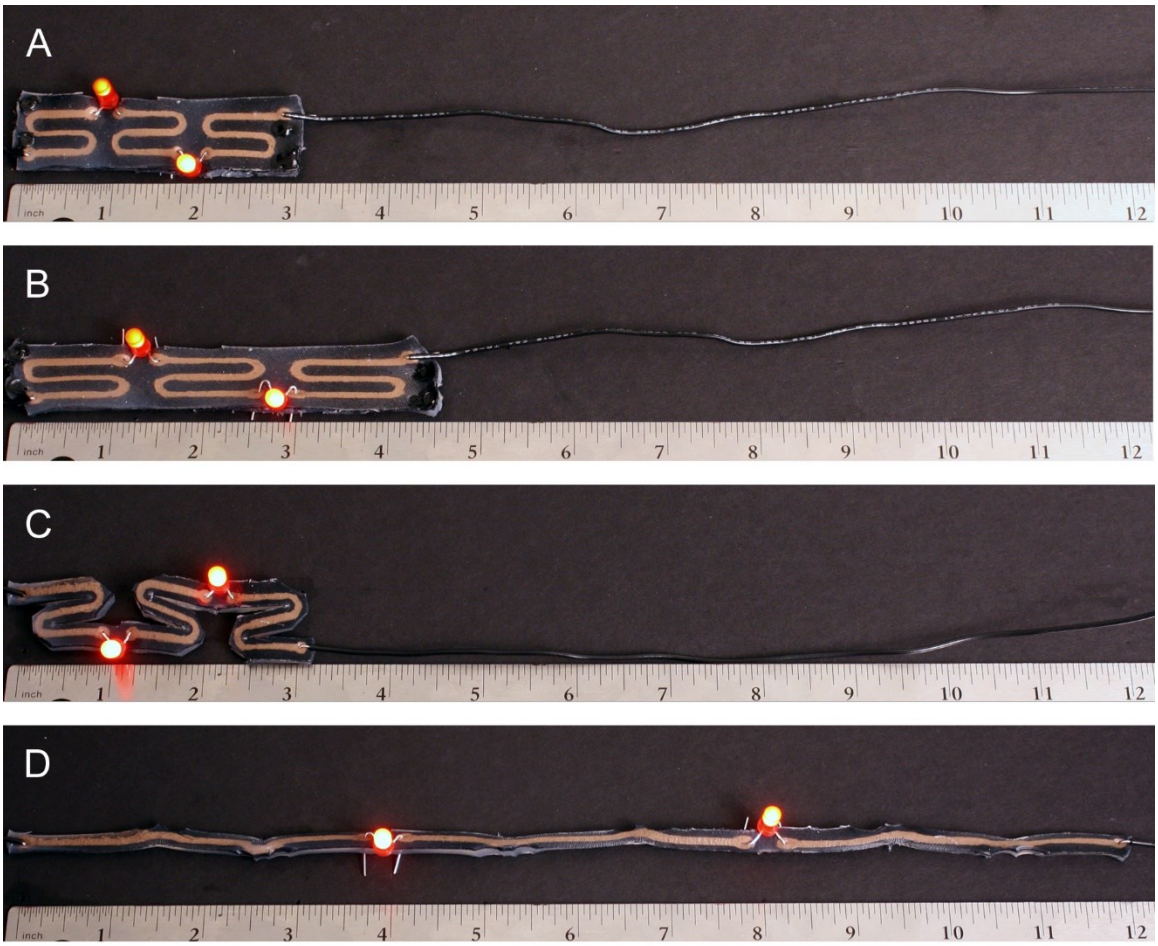

Figure 30: Demonstration of stretchable LED circuit (A) at 0% and (B) 50% strain. Serpentine variant of stretchable LED circuit at (C) 0% (D) 300% strain.

3.2.5 Patterning for Circuit Manufacturing

In addition to the ability to make highly conductive composites that retain their conductivity under strain, the filtration-based fabrication approach reported here can be used to pattern the Cu-Ag NW composite onto stretchable fabric. In addition to enabling the creation of wearable stretchable circuits, Figure 30 shows how patterning onto fabric can be used to create conductive traces that enable much greater

stretchability than can be achieved with the native material. To create the pattern in Figure 8A, the Cu-Ag NWs were filtered through a gasket with serpentine holes onto stretchable fabric, after which the NWs were annealed, and both the NWs and stretch fabric were infiltrated with PDMS. LEDs were electrically connected to the conductive composite by simply inserting the leads through the material. The lit LEDs illustrate the conductivity of the material and its potential for use in stretchable electronics (Figure 8A). By itself, the fabric-NW composite exhibited a maximum strain of approximate 50%, which was limited by the stretchability of the fabric (Figure 30B). Cutting lines between the conductive traces (Figure 30C) allows the circuit to unfold and stretch to 300% strain (Figure 30D), while retaining enough conductivity to power the red LEDs.

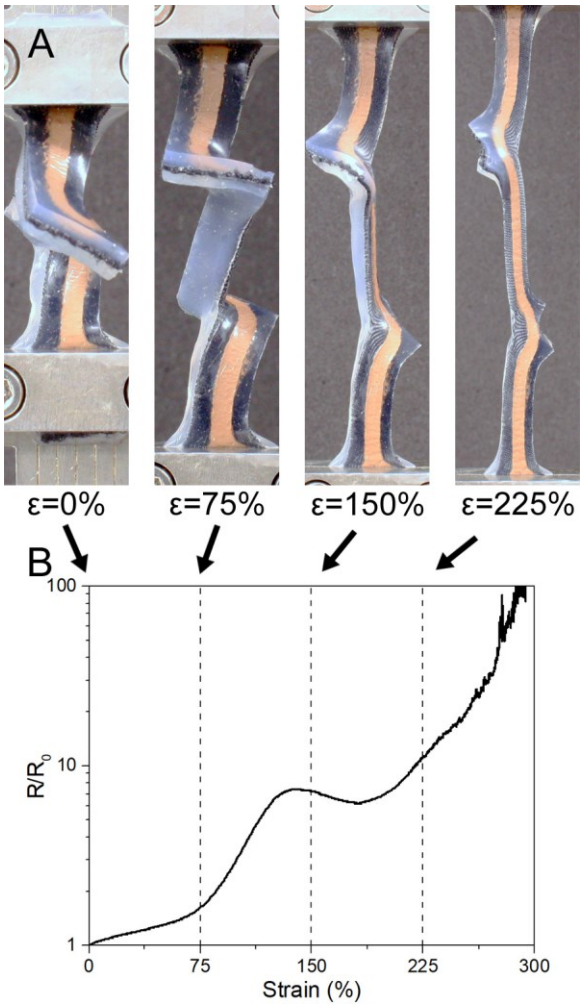

Figure 31: Serpentine Cu-Ag NW trace properties (A) at various degrees of strain illustrating the unfolding process. (B) Strain vs. R/R_0 behavior of the serpentine trace.

Photographs of the serpentine pattern during the strain process (Figure 31A), shows the modes of twisting, bending, and straining that occurs during the unfolding and stretching of the serpentine pattern. The R/R_0 vs. strain behavior (Figure 31B) shows an initial increase to ~150%, a small decrease in R/R_0 to 175%, and a further increase to 300%. We attribute the flat part of the R/R_0 curve to the untwisting of the serpentine

pattern that occurs at 150% strain. These results illustrate not only the extreme stretchability of the patterned composite, but also its ability to retain conductivity during bending and twisting, which are essential modes of motion for wearable electronics.

3.3 Summary

This chapter demonstrates that an infiltrated felt of Cu-Ag core-shell nanowires retains its conductivity under strain better than any composite with a conductivity greater than 1000 S cm^{-1}, including those using AgMFs at concentrations double that of the Cu-Ag nanowires. Given that the composites reported here exhibit better performance than Ag MFs, and use 15 times less silver, this work demonstrates the potential for Cu-Ag nanowires to serve as a more economical and sustainable filler for stretchable conductors. In addition to high performance, this work shows that increasing the stiffness of the PDMS matrix leads to a greater loss of conductivity under strain. This conductivity loss appears to be due to the formation of voids during stretching, which we attribute to debonding between the PDMS matrix and the nanowires. Finally, we show that the nanowire composite can be patterned to create serpentine circuits that retain their functionality up to strains of 300%. Future work might explore the use of this material in clothing-integrated circuits for wearable electronics, or implement an elastomer matrix that has less stiffness than the Ecoflex 00-30 used in this chapter as to improve R/R_0 vs. strain performance. Additionally, a

conductive elastomer could potentially be used to perform infiltration instead of PDMS, which may improve the overall conductivity of the composite above what is already observed.

4. NW Composites from Cofiltration and Aerogels

4.1 Cofiltration of Cu-Ag NWs and Waterborne Elastomer

One of the challenges with the infiltration method for making circuits out of conductive stretchable composites is the scalability of the elastomer infiltration procedure. The size of a stretchable circuit is limited to the size of the infiltration bath used, and the process of infiltration and curing requires processing on the hour-long timescale,[12-14, 78, 89] limiting the capabilities for large scale production. In addition, the infiltration of material also mandates the trimming of excess elastomer to allow for direct electrical contact to the composite, introducing additional steps in the manufacturing process. While printing is feasible as a method of more rapid composite manufacturing, the issue of cycling durability of blended conductive filler in a printable elastomer ink is present, as previously discussed in Chapter 1.3.

A method I propose to address this challenge is to cofilter Cu-Ag NWs with waterborne elastomer microspheres. The infiltration procedure is a four-step procedure: filtering of NWs, annealing of NWs, infiltrating the NW network with elastomer, and curing of the elastomer in the composite. This can be simplified with cofiltration procedure by reducing the number of steps to a two-step procedure of filtering NWs

and elastomer simultaneously, followed by a heating step which simultaneously anneals the wires together and melts the elastomer spheres into a coherent composite. In addition, there are a wide variety of waterborne rubbers that have been manufactured and can be used to manufacture such a composite, including but not limited to: latex rubber, polyurethane, silicone, and SBS rubber.[123-126] Also, this method allows for a more rapid production rate than infiltration, and avoids the use of volatile solvents required for printing elastomer composites, such as chloroform or methylisobutylketone. Hypothetically, we should also see improved cycling durability relative to printed composites, as there is an opportunity to anneal NWs that are directly in contact with each other using this technique. This study observes the results of stretchable conductive composites manufactured using cofiltration, compares the results to filtered Cu-Ag NWs with PDMS infiltration and printed composites of Cu NWs and SBS rubber, and addresses the challenges in improving the quality of this composite manufacturing technique.

4.1.1 Cofiltration Methods and Materials

In a 50 mL centrifuge tube, 120 μL of triethylamine (Acros, 99%) is added to 40 mL of H_2O to help maintain the dispersion of materials added later in solution. Waterborne polyurethane (PU) was supplied by Bond Polymer (Bondthane UD-375, 58 vol% PU in H_2O), which is comprised of microspheres with average diameters of 1.6 ± 0.5 μm, as seen in Figure 32. 35 μL of the waterborne PU (20 μL solid volume) was

added into solution. The concentration of Cu-Ag NWs in the cofiltered composite is determined by the ratio of the volume of PU added vs. the volume of Cu-Ag NWs added. In order to develop a 10 vol% composite, 4.5 mL of a 4.5 mg/mL solution of Cu-Ag NWs (2.2 μL solid volume) directly from PVP/DEHA storage solution are added to the PU solution. This solution is vortexed for 1 min after all components are added, and 22.5 mL of solution is vacuum filtered through a Millipore vacuum filtration setup containing a patterned silicone gasket and 400 x 400 wire cloth. Vacuum is pulled on the wire solution for 3 minutes until all solution has passed. Samples are annealed via a heat press (Promo Heat) for three minutes at 125 °C, followed by 30 minutes of post-annealing in a 150 °C oven. Electrical conductivity and analysis of resistance during strain are performed as previously described in Chapter 3.1.3.

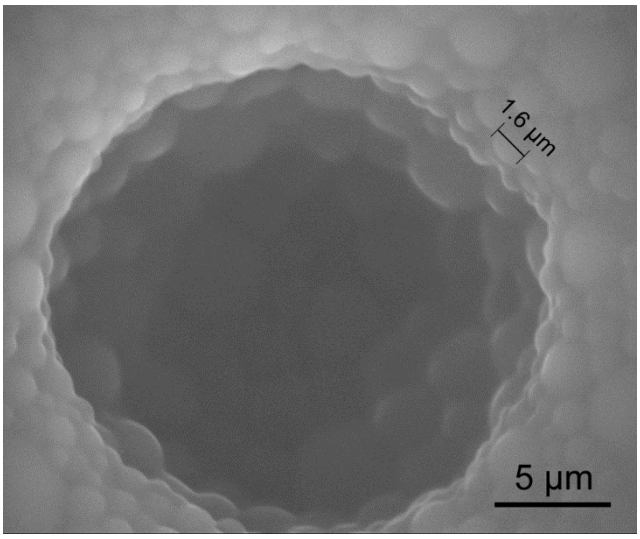

Figure 32: SEM microscope image of plain PU microspheres. A highlighted sphere indicates average diameter.

4.1.2 Cofiltration Results and Conductivity

During the filtration of 50 mL of solution containing 25 mg of only Cu-Ag NWs, which was performed in Chapter 3.1.2, the entirety of the solution passes through the filter in approximately 15 s, leaving behind a felt that is approximately 250 μm thick. However, the 20 mg Cu-Ag NW/waterborne rubber solution (Figure 33A) takes significantly longer to filter 20 mL of solution, upwards of 3 minutes. If more of the solution is added, there is a point where there is a complete clog, and no additional material is filtered. This occurs as the waterborne PU proceeds to completely seal the metal cloth, not allowing more water to pass through. The use of a coarser cloth leads to the NWs and PU to pass completely through the cloth instead of catch and filter, and fails to form a coherent network atop the cloth. This limits the thickness of the composite to approximately 130 μm, which presents challenges for making thicker traces. Nonetheless, even at the reduced thickness relative to the Cu-Ag NW felt, the cofiltered composite can still be readily removed from the metal cloth to allow for further processing and analysis. (Figure 33B).

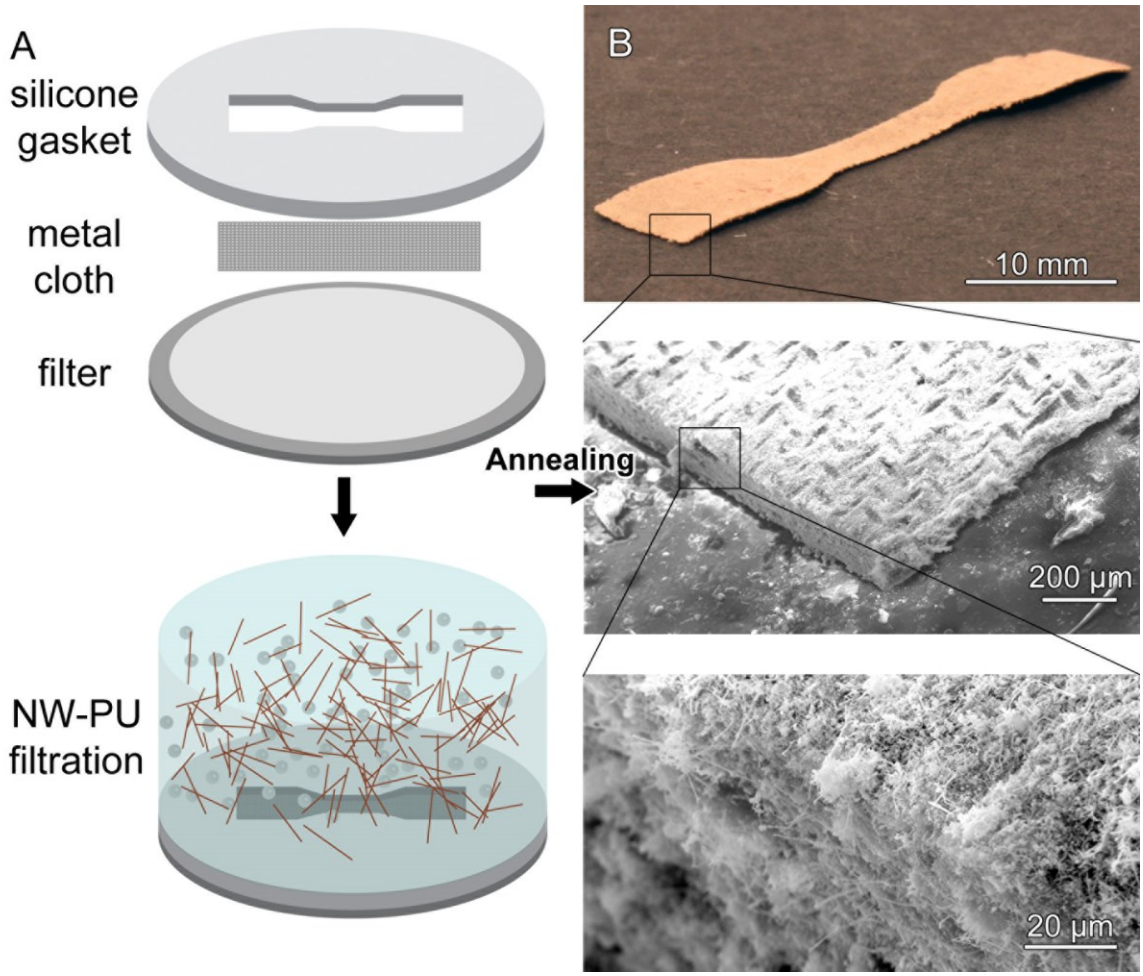

Figure 33: Procedure for the cofiltration method for composite manufacturing (A) Cu-Ag NWs and PU microspheres were filtered through a silicone gasket. (B) Photograph and SEM image of the composite after annealing.

Samples were heat-pressed to melt the PU microspheres and generate a coherent network by filling in any remaining pores. SEM images in Figure 33 show a 10 vol% Cu-Ag NW in PU matrix before (Figure 34A) and after heat-pressing (Figure 34B). Before heat-pressing, individual microspheres are still distinctly visible within the composite. After heat-pressing, the PU spheres melt to form a solid network, closely resembling

that of the PDMS-infiltrated network. This heating step is essential to the manufacturing of the stretchable conductive composite, as the lack of bonding between rubber spheres limits the maximum stretchability of composite. Comparing the unannealed composite to the annealed composite, the stretchability is significantly increased from approximately 25% strain to upwards of 500% strain (Figure 34C).

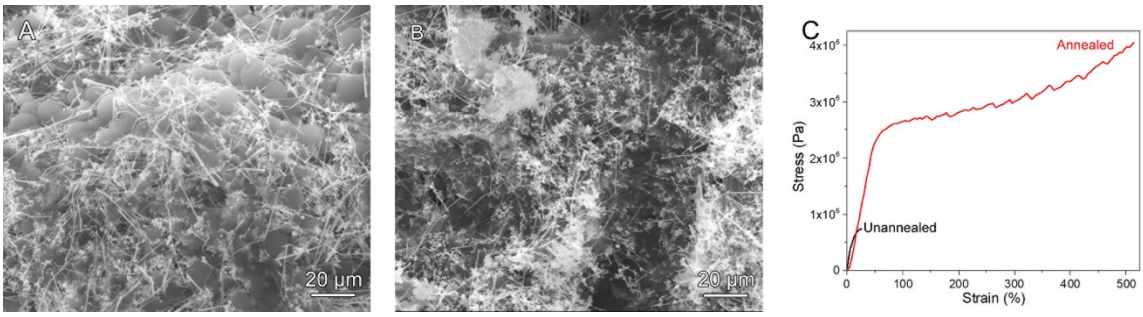

Figure 34: Cofiltered composite properties relative to annealing. (A) SEM image of composite before annealed and (B) after annealing. (C) Stress vs. strain behavior of annealed and unannealed composites.

In addition, heat pressing improves the conductivity of the composite by a factor of 2.3, from 290 ± 59 S cm^{-1} to 670 ± 82 S cm^{-1}. The conductivity of the annealed sample is approximately half that of the infiltrated PDMS-NW composite (1270 S cm^{-1}) but is still approximately double that of 12 vol% Cu-Ag NWs blended with PCL (370 S cm^{-1}).[16] The reasoning for this result is that the technique for mixing the NWs with polymer provides an intermediate level of contacts between NWs relative to the two previously-addressed NW-polymer composites. An infiltrated network has all conductive NW contacts in place before the introduction of polymer, while blending NWs and dissolved polymer in solvent can allow polymer to coat and impede electrical contacts between NWs.

Cofiltration acts as a hybrid between the two techniques; while there is no potential for coating the entirety of a NW with polymer during the filtration step, the presence of PU microspheres is able to slightly inhibit contact between the Cu-Ag NWs as they are cofiltered. Therefore, this method of cofiltration can generate higher-conductivity composites than those manufactured through the blending technique, but is still limited in conductivity relative to the infiltration technique. Additionally, the processing time is greatly reduced relative to the infiltrated felt composite. The processing time is reduced from over 4 hours to approximately 45 minutes as infiltration and curing steps are not performed during the cofiltration procedure.

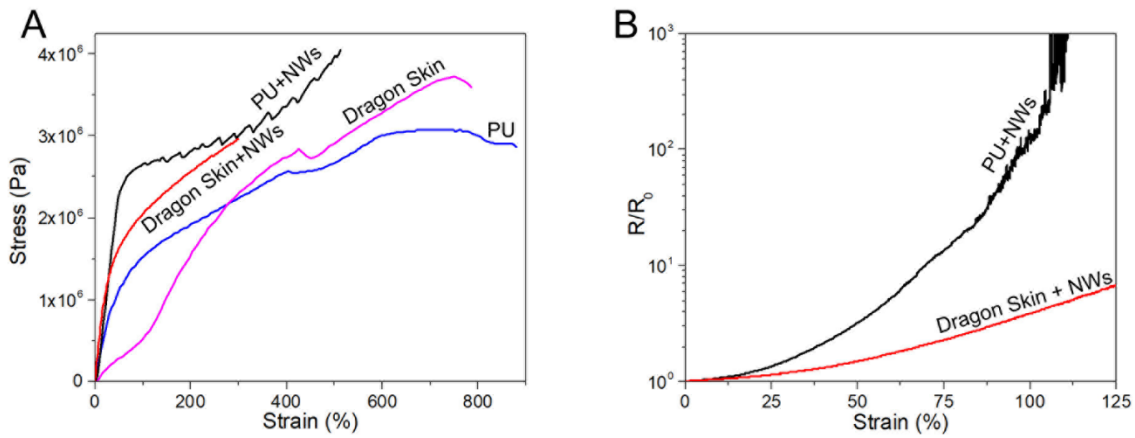

Figure 35: Comparison of PDMS-infiltrated composites vs. PU-cofiltered composites. (A) Stress vs. strain behavior of Dragon Skin and PU with and without NWs. (B) R/R_0 vs. strain behavior for the Dragon Skin and PU composites.

4.1.3 Stress vs. Strain and R/R_0 vs. Strain Analysis

The stretchability of the PU-NW composite relative to plain PU is shown in Figure 35A, alongside the previous results for plain Dragon Skin and Dragon Skin-

infiltrated NWs. Plain PU samples were manufactured by coating the waterborne PU directly from solution on glass, allowing it to air-dry for 12 h, followed by an identical heat pressing and oven heating method as described in Chapter 4.1.1. This comparison was chosen as the reported 100% moduli between the two polymers are similar (0.69 MPa for UD-375, 0.59 for Dragon Skin 30), as to minimize effects between stiffness-dependent strain vs. R/R_0 behavior as previously detailed in Chapter 3. Both plain elastomers have comparable maximum stretchability, with approximately 800% for Dragon Skin and 900% for PU. With a 10 vol%-loaded composite, however, the PU composite is more stretchable, up to 500%, compared to the 300% stretchability of the Dragon Skin composite. This may be due to polyurethane having an increased tear strength than Dragon Skin, as void formation in the composite becomes the most likely point of failure for the entire composite. Additionally, reducing the number of steps of processing reduces the probability that cracks or defects will occur during the handling of the delicate Cu-Ag NW felt, which is only required during the infiltration procedure. Therefore, the maximum stretchability presents a potential advantage for the cofiltration technique relative to the infiltration technique, as processing defects may be minimized.

The strain vs. R/R_0 behavior is compared between the PU and Dragon Skin composites in Figure 35B. The PU composite exhibits significantly greater loss of conductivity with additional strain, with R/R_0 values of 3.2 and 113 at 50% and 100%

strain respectively, well above the values of 1.5 and 3.9 for Dragon Skin at identical strains. This performance is comparable to the results via Huang *et al*., where the R/R_0 values at 50% and 100% strain were approximately 10 and 115 respectively.[84] Therefore, we can conclude that the R/R_0 behavior of the PU-NW composite is more similar to that of a network of NWs blended with polymer relative to a NW network infiltration with elastomer.

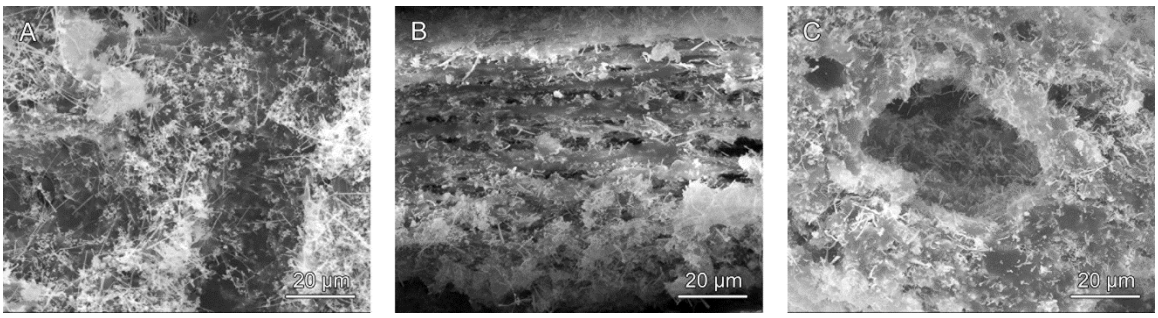

Figure 36: SEM images of the PU composite (A) before strain, (B) at 100% strain, and (C) after relaxation back to 0% strain. Void formation comparable to the Dragon Skin composite, as seen in Figure 24, is observed.

In order to help explain this behavior, the mechanism of conductivity loss during strain in the PU-NW composite is visible in Figure 36. While some initial voids are present in Figure 36A due to incomplete filling of the melted PU, the creation of additional voids, as well as the extension and enlargement of the voids, are visible in Figure 36B. Once returned to a relaxed state (Figure 36C), large voids are present in the composite. In addition, voids formed are much larger than the voids present in the Dragon Skin composite and do not appear to buckle likewise, as seen in Figure 24F.

Void formation in this composite is similar to what is observed in the Dragon Skin-NW composite during strain, which is consistent given the similar stiffnesses between Dragon Skin and PU. The generation of larger voids may also be a reason why there is a greater loss of conductivity with additional strain, as more electrical contacts would be lost during strain if a greater number of voids and larger voids are present. The increase in voids may also be due to the nature of imperfections within the composite. During PDMS infiltration, there is a completely coherent network of PDMS within the pores of the NW felt. During hot-pressing and annealing of PU, any incomplete melting of the PU spheres may act as defect points for additional void formation and growth, as some small voids are visible in the initial PU composite.

4.1.4 Composite Cycling

Cycling behavior at 50% strain over 50 cycles is observed in Figure 37. After the first strain cycle, the R/R_0 increases to 3.8 at 50% strain and decreases to 2.2 when returned to 0% strain. The R/R_0 steadily increases with additional cycles, culminating in a maximum R/R_0 of 24 after 50 cycles at 50% strain. These results are significantly greater than previous results for the Dragon Skin composite, where R/R_0 behavior was stable after 50 cycles. However, this result outperforms the Huang *et al*. result, which suffers from a complete loss in conductivity after 10 stretching cycles at 50% strain.[84] Despite the improved performance relative to the blended NW composite, improvements are required to ensure it has stability with additional stretching cycles, as progressive losses

in conductivity are observed with the PU-NW composite, which has been seen in other sintered, blended composites of metal nanomaterials and elastomer.[83]

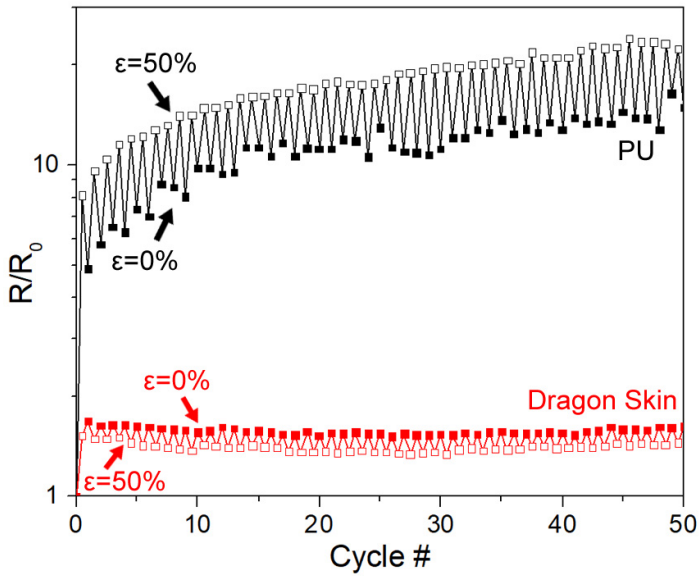

Figure 37: Cycling behavior of the PU composite relative to the Dragon Skin composite. Cycles were performed at 50% strain.

Additionally, we are seeing results in the cycling data similar to most of the previous literature on stretchable conductive composites, where the composite is more conductive at 0% strain than while stretched to 50% strain during cycling. Observations of the R/R_0 behavior during strain during the 1st cycle and during the 51st cycle are compared between the PU-NW composite and the Dragon Skin-NW composite at 50% strain. Comparing for stress vs. strain behavior, comparable behavior is seen between the PU-NW composite (Figure 38A) and the Dragon Skin-NW composite (Figure 38B). Plastic deformation and strain-softening is observed, similarly observed in Figure

28A&B for the Ecoflex and Dragon Skin composites at 100% strain. The R/R_0 vs. strain behavior for both composites are compared in Figure 38C&D. Although the R/R_0 has a much larger increase in the PU-NW composite relative to the Dragon Skin composite, the shape of the curves for R/R_0 vs. strain are similar, with a constant increase in R/R_0 during the 1st cycle, and a maximum R/R_0 occurring near the point of plastic deformation. The major difference is that there is greater recovery from the maximum R/R_0 for the Dragon Skin composite, as the R/R_0 decreases from the maximum to being lower at 50% strain than at 0% strain, relative to the PU composite where the R/R_0 does similarly decrease from the maximum, but is still well above the R/R_0 value at 0% strain once it is fully extended to 50% strain. Therefore, we can hypothesize that potential alignment effects occur more readily with pre-established contacts than with the contacts generated through co-filtration, but these two methods have similar behavior in where void generation and a degree of a wire alignment can still influence the R/R_0 behavior of the composite under strain.

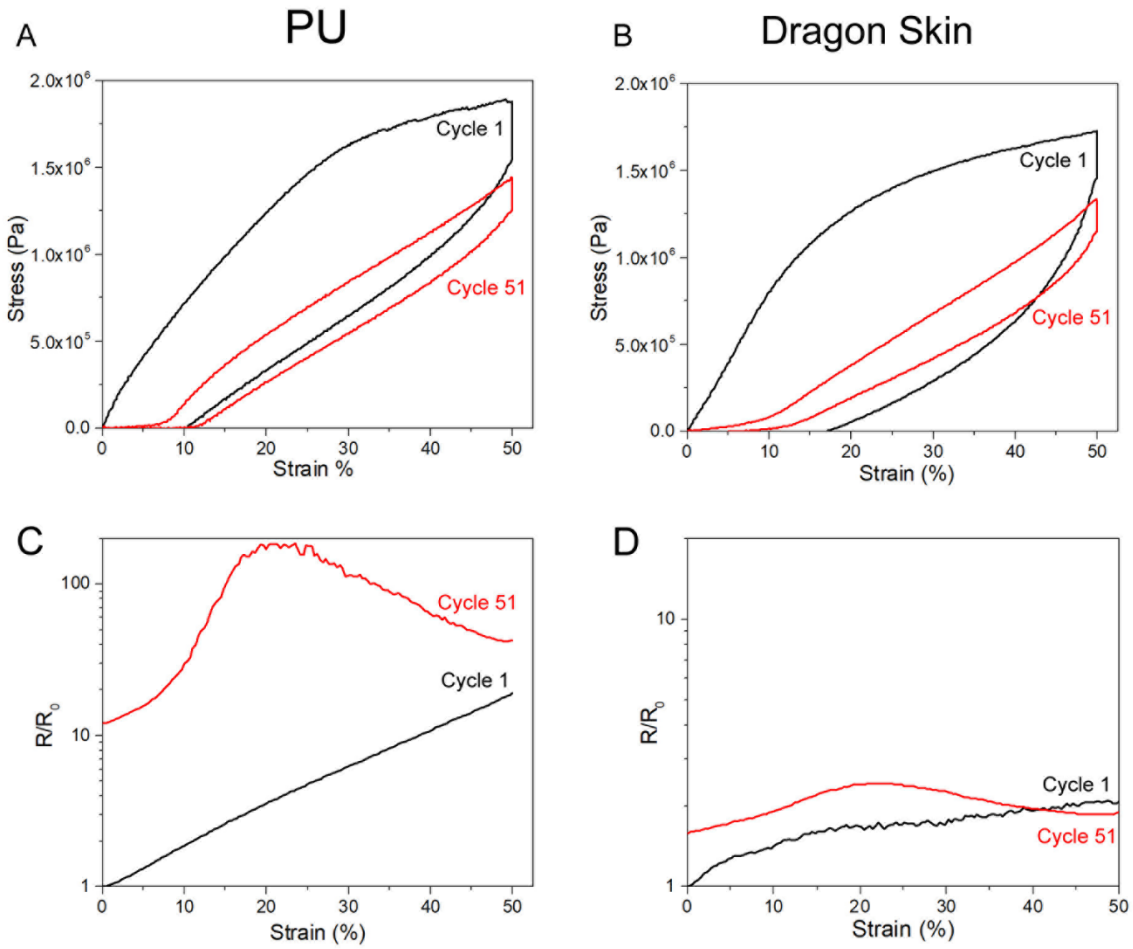

Figure 38: Analysis of PU and Dragon Skin composites during strain before and after cycling (A&B) Stress vs. strain curves for PU and Dragon Skin composites. (C&D) R/R_0 vs. strain behavior for PU and Dragon Skin composites after the 1st and 51st cycle at 50% strain.

4.1.5 Summary

While promising for not using the volatile solvents required for printing, having a faster manufacturing procedure than elastomer-infiltrated composites, and having the potential for high conductivity and improved cycling durability relative to blended composites, there is room for improvement in quality of conductive stretchable

composites manufactured via cofiltration of elastomer and conductive metal nanowires. Regardless, there are many additional, future avenues for the potential improvement of this method of composite manufacturing that could lead to electrical performance competitive with PDMS-infiltrated Cu-Ag NW felts. Certain potential methods to improve this technique may include the following: the use of elastomer microspheres with reduced stiffness, given the known correlations between elastomer matrix stiffness and the retention of conductivity with strain, or the use of smaller particulates that are still capable of being co-filtered without passing though the NW felt and the metal cloth, and may reduce the inhibition of contacts within the conductive filler.

4.2 Cu-Ag NW Aerogels

Aerogels are a commonly-studied material for the fabrication of stretchable conductive composites. They allow for the capability of high conductivity in a very low-density network, as pre-established contacts before infiltration allow for conductivity to occur well before the percolation threshold of the material for a normally blended composite, as previously detailed in Chapter 1.3. One of the factors that allows for the high conductivity of our stretchable conductive composite is the relatively low porosity of filtered felt (90%) relative to the porosities of NW-based aerogels (>99%).[12, 89, 127] While aerogels of a variety of conducive materials have been studied, a Cu-Ag NW aerogel has not been previously manufactured. Cu NW aerogels have low conductivity due to their low oxidation resistance.[89] Ag NW aerogels have also been made but are very-low

density or use very short NWs, due to the costs and materials required to make large enough batches of Ag NWs for aerogel manufacturing.[12, 127] There is promise in the manufacturing and study of Cu-Ag NW aerogels, as they have greater oxidation resistance than Cu NWs, but can be processed on a scale where manufacturing is more feasible relative to Ag NWs. In this section, I observed the behavior and properties of a Cu-Ag NW aerogel and its precursors using Cu-Ag NWs of varied aspect ratios, as to compare it to the Cu-Ag NW felts manufactured in Chapter 3.1.2.

4.2.1 Manufacturing Aerogels of Cu-Ag NWs with Varied Aspect Ratios

Cu-Ag NWs for four different aspect ratios were synthesized; 10, 110, 175, and 230. NWs of an aspect ratio of 175 (AR 175) were synthesized identically to the procedure detailed in Chapter 3.1.1. NWs of an aspect ratio of 230 (AR 230) were synthesized by using the same parameters as the 175 AR reaction, but performed at a 2 L scale instead of a 10 L scale. NWs of an aspect ratio of 110 (AR 110) were synthesized identically to the 230 AR reaction, in addition to increasing the volume of glucose used from 150 mL to 250 mL. NWs of an aspect ratio of 10 (AR 10) were synthesized via a separate procedure at the 2 L scale. 1.5 L of 15 M NaOH, 125 mL of 0.1 M $Cu(NO_3)$, and 16 mL of EDA were shaken together in a 2 L bottle. Both this solution and 250 mL of 1 g/mL glucose were preheated to 50 °C, and the glucose was added into the Cu precursor solution. The bottle was left to sit at room temperature for 5 minutes to allow for NW

growth. All Cu NWs were silver coated identically by previously detailed procedures in Chapter 3.1.1.

All Cu-Ag NWs were initially concentrated to 4 mg/mL in PVP/DEHA storage solution. 3 mL of solution was transferred into a 15 mL centrifuge tube, and were centrifuged for 5 minutes at 2000 rpm. The supernatant was removed, and the NWs were rinsed into DI H_2O. This procedure was repeated three times to remove PVP/DEHA from solution. Once concentrated into a 3 mL solution, the solution is poured into a 3 mL polyethylene well. The NWs were allowed to settle for 4 h, until the supernatant of the settled solution is clear of NWs. The wells containing solution are placed in an -80 °C Isotemp freezer for 1 hr to freeze the solutions. After freezing, the samples are then placed into a Labconco freeze-drier for 24 h to allow for the freeze-drying of the aerogels. Dried aerogels are removed from the well, and are measured for mass, diameter, and thickness as to calculate density.

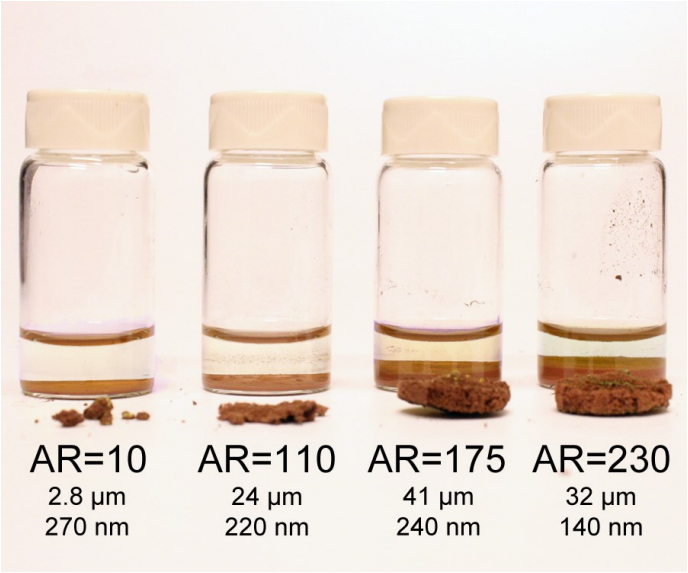

Figure 39: Photograph of settled Cu-Ag NWs in solution and subsequent aerogels formed after freeze-drying.

4.2.2 Visualization and Density Characteristics of Aerogels

A photograph in Figure 39 illustrates the degree of settling for identical concentrations of the Cu-Ag NWs. After 4 h of settling, there is a noticeable difference in thickness between the four settled solutions. The density of the settled NW solution and of the aerogel are compared relative to each other, in additional the theoretical density of colloidal rods settled in solution in Figure 40. The theoretical density of settled rods in solution in units of volume fraction generally follows a trend of the inverse of aspect ratio, with the factor dependent upon what type of packing occurs in the network, whether as a gel or a glass packing.[128-130] By measuring the volume of the settled NWs in the vial, the measured density is similar to the theoretical concentration of a NW gel given nanocellulose-like packing within the glass region,[131] where the trend

of packing fraction follows by the inverse of the aspect ratio multiplied by a factor of 1.54, and had observed a range of aspect ratios (29-1180) in which the aspect ratios used in our experiments were mostly within (10-230).[132] Given this density, an aspect ratio of approximately 15 would be required to achieve a concentration of 10 vol% as a gel in solution if identical nanocellulose glass-type packing is present with the Cu-Ag NW glasses.

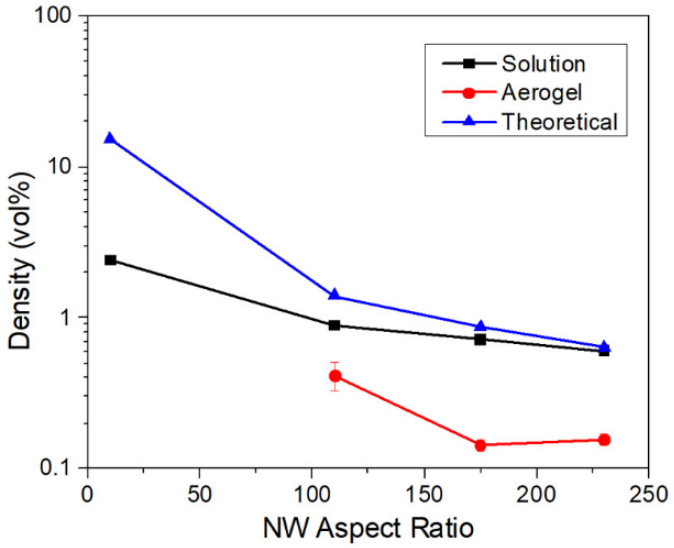

Figure 40: Density calculations of Cu-Ag NWs relative to aspect ratio , for NWs settled in solution, NWs freeze-dried into an aerogel, and the theoretical packing density of a colloidal rod glass.

Once freeze-dried into an aerogel, the density of the aerogels is significantly reduced relative to the settled solution. A microscope image of the AR 175 aerogel is seen in Fig 41. Large pores are visible within the aerogel, which can be attributed to the formation of large ice crystals due to slow freezing of the composite, which have been

previously observed in NW aerogels.[12, 89] As the sample is frozen, the formation of ice crystals in water begin to push against the NWs in solution until they are wedged in between crystal boundaries. Afterwards, the NWs become compressed into a network along the boundaries.[12] This may be attributed to why there is a loss in density, as the motion of ice crystal formation causes the NW network to expand in solution. Although may can be mitigated by the faster freezing or lower temperature freezing of the solution[12] using liquid nitrogen (LN_2), the immersion of the well into LN_2 leads to sample agitation, which disrupts the settled solution and decreases the concentration of the aerogel. Therefore, in order to compensate, nanowires of an aspect ratio less than 15 would be needed for similar concentration to the Cu-Ag NW felts at 10 vol%. As also seen in Figure 39, NWs with an aspect ratio of 10 were unable to form a coherent aerogel. Given this is similar to the targeted aspect ratio for a 10 vol% density aerogel, this presents a challenge for forming a coherent aerogel at the desired density for high conductivity. In addition, shorter NWs in a composite have been modeled to create a much stiffer network than one of longer NWs.[7] Even if a nanowire network of a low enough aspect ratio to form a 10 vol% density composite, the increased stiffness of the composite would very likely result in worse R/R_0 vs. strain performance, as concluded in chapter 3.2.2, once infiltrated with elastomer.

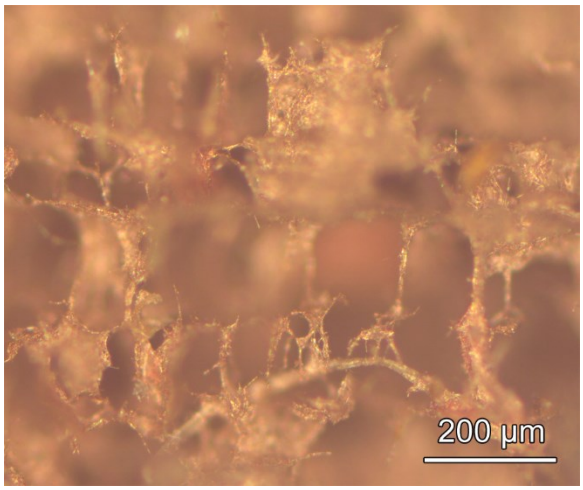

Figure 41: Microscope image of aerogel made with 175 AR Cu-Ag NWs.

4.2.3 Summary

While Cu-Ag NW-based aerogels of variable density can be readily manufactured, they are unsuitable for highly conductive stretchable composites due to their low density; and attempts to form a high-density network are not stable enough to be handled properly after freeze-drying. Otherwise, there is some potential in the use of Cu-Ag NW aerogels, due to greater oxidation resistance relative to Cu NW aerogels, and ease of processing relative to Ag NW aerogels. Additionally, some properties may still allow for stretchable anti-static composites and strain sensors, and further analysis into the correlation between aspect ratio and how it can influence properties other than density, such as electrical conductivity, thermal conductivity, and Young's Modulus may be studied in the future.

5. Conclusion

In conclusion, the availability of large-scale syntheses of copper nanowires allow for the manufacturing and analysis of new composite materials that can only be practically generated via large-scale syntheses. As detailed in Chapter 2, a gram-scale synthesis of copper nanowires allowed for the manufacturing of a Cu-SiO_2 NW based ink for fully printed memristor arrays, in which larger-scale syntheses can allow for the mass-production of this ink and a method to mass-produce printable memories. In Chapter 3, the multi-gram scale synthesis of copper nanowires allowed for the manufacturing of 3D stretchable conductive composites for testing capabilities, as well as a serpentine stretchable conductor that is able to stretch to over one foot in length. Additionally, the composite has very high cycling endurance while maintaining high electrical conductivity to levels unseen in previously-studied stretchable conductive composites. Lastly, in Chapter 4, other new nanowire composites can be manufactured and studied more readily thanks to the multi-gram synthesis. For example, the manufacturing of Cu-Ag NW aerogels with variable density relative to the aspect ratio of the Cu-Ag NWs used, and the cofiltration of NWs and waterborne rubber for stretchable conductive composites, which allows for more the rapid production of stretchable conductive composites with comparable conductivity to PDMS-infiltrated felts.

While the document details some of the potential applications that are available thanks to the large-scale synthesis of copper nanowires, there are many other avenues that may be potentially explored. As it is known how aspect ratio can influence the density of aerogels, the same aspect ratios may have similar density effects on filtered Cu-Ag NW felts, allowing for Cu-Ag NW felts with tunable porosity, and studies can look into how tuning the porosity and aspect ratio may influence electrical conductivity, thermal conductivity, and Young's modulus. In addition, studies could be performed to observe how those properties change in a polymer composite, as well as other polymer-NW interactions as previously studied in regards to stretchable conductive composites.

Another challenge is the improvement of large-scale syntheses using an alkylamine-mediated Cu NW synthesis in place of an EDA-mediated synthesis. The alkylamine-mediated synthesis does not require the use of NaOH and results in NWs that have much higher aspect ratios relative to the NWs synthesized via the EDA-mediated synthesis. However, the alkylamine needs to be stripped from the NW surfaces in order to modify them with oxidation-resistant coatings. If this barrier can be crossed, this opens up additional paths for research into devices and composites manufactured using large-scale syntheses of Cu NWs with much greater lengths, and can build further upon the research I have presented in this dissertation.

References

1. White, S. I.; Mutiso, R. M.; Vora, P. M.; Jahnke, D.; Hsu, S.; Kikkawa, J. M.; Li, J.; Fischer, J. E.; Winey, K. I., Electrical Percolation Behavior in Silver Nanowire–Polystyrene Composites: Simulation and Experiment. *Adv. Funct. Mater.* **2010,** *20* (16), 2709-2716.

2. Gelves, G. A.; Lin, B.; Sundararaj, U.; Haber, J. A., Low Electrical Percolation Threshold of Silver and Copper Nanowires in Polystyrene Composites. *Adv. Funct. Mater.* **2006,** *16* (18), 2423-2430.

3. Wang, S.; Cheng, Y.; Wang, R.; Sun, J.; Gao, L., Highly Thermal Conductive Copper Nanowire Composites with Ultralow Loading: Toward Applications as Thermal Interface Materials. *ACS Appl. Mater. Interfaces* **2014,** *6* (9), 6481-6486.

4. De, S.; Higgins, T. M.; Lyons, P. E.; Doherty, E. M.; Nirmalraj, P. N.; Blau, W. J.; Boland, J. J.; Coleman, J. N., Silver Nanowire Networks as Flexible, Transparent, Conducting Films: Extremely High DC to Optical Conductivity Ratios. *ACS Nano* **2009,** *3* (7), 1767-1774.

5. Ye, S.; Rathmell, A. R.; Chen, Z.; Stewart, I. E.; Wiley, B. J., Metal Nanowire Networks: The Next Generation of Transparent Conductors. *Adv. Mater.* **2014,** *26* (39), 6670-6687.

6. Lee, J.; Lee, P.; Lee, H.; Lee, D.; Lee, S. S.; Ko, S. H., Very long Ag nanowire synthesis and its application in a highly transparent, conductive and flexible metal electrode touch panel. *Nanoscale* **2012,** *4* (20), 6408-6414.

7. Lee, P.; Lee, J.; Lee, H.; Yeo, J.; Hong, S.; Nam, K. H.; Lee, D.; Lee, S. S.; Ko, S. H., Highly Stretchable and Highly Conductive Metal Electrode by Very Long Metal Nanowire Percolation Network. *Adv. Mater.* **2012,** *24* (25), 3326-3332.

8. Li, B.; Ye, S.; Stewart, I. E.; Alvarez, S.; Wiley, B. J., Synthesis and Purification of Silver Nanowires To Make Conducting Films with a Transmittance of 99%. *Nano Lett.* **2015,** *15* (10), 6722-6726.

9. Bari, B.; Lee, J.; Jang, T.; Won, P.; Ko, S. H.; Alamgir, K.; Arshad, M.; Guo, L. J., Simple hydrothermal synthesis of very-long and thin silver nanowires and their

application in high quality transparent electrodes. *Journal of Materials Chemistry A* **2016,** *4* (29), 11365-11371.

10. Li, R.-Z.; Hu, A.; Zhang, T.; Oakes, K. D., Direct Writing on Paper of Foldable Capacitive Touch Pads with Silver Nanowire Inks. *ACS Appl. Mater. Interfaces* **2014,** *6* (23), 21721-21729.

11. Akter, T.; Kim, W. S., Reversibly Stretchable Transparent Conductive Coatings of Spray-Deposited Silver Nanowires. *ACS Appl. Mater. Interfaces* **2012,** *4* (4), 1855-1859.

12. Gao, H.-L.; Xu, L.; Long, F.; Pan, Z.; Du, Y.-X.; Lu, Y.; Ge, J.; Yu, S.-H., Macroscopic Free-Standing Hierarchical 3D Architectures Assembled from Silver Nanowires by Ice Templating. *Angew. Chem. Int. Ed.* **2014,** *53* (18), 4561-4566.

13. Ge, J.; Yao, H.-B.; Wang, X.; Ye, Y.-D.; Wang, J.-L.; Wu, Z.-Y.; Liu, J.-W.; Fan, F.-J.; Gao, H.-L.; Zhang, C.-L.; Yu, S.-H., Stretchable Conductors Based on Silver Nanowires: Improved Performance through a Binary Network Design. *Angew. Chem. Int. Ed.* **2013,** *52* (6), 1654-1659.

14. Zhu, C.-H.; Li, L.-M.; Wang, J.-H.; Wu, Y.-P.; Liu, Y., Three-dimensional highly conductive silver nanowires sponges based on cotton-templated porous structures for stretchable conductors. *RSC Advances* **2017,** *7* (1), 51-57.

15. Yang, C.; Gu, H.; Lin, W.; Yuen, M. M.; Wong, C. P.; Xiong, M.; Gao, B., Silver Nanowires: From Scalable Synthesis to Recyclable Foldable Electronics. *Adv. Mater.* **2011,** *23* (27), 3052-3056.

16. Cruz, M. A.; Ye, S.; Kim, M. J.; Reyes, C.; Yang, F.; Flowers, P. F.; Wiley, B. J., Multigram Synthesis of Cu-Ag Core-Shell Nanowires Enables the Production of a Highly Conductive Polymer Filament for 3D Printing Electronics. *Part. Part. Syst. Char.* **2018**.

17. Rathmell, A. R.; Bergin, S. M.; Hua, Y. L.; Li, Z. Y.; Wiley, B. J., The growth mechanism of copper nanowires and their properties in flexible, transparent conducting films. *Adv. Mater.* **2010,** *22* (32), 3558-3563.

18. Bergin, S. M.; Chen, Y.-H.; Rathmell, A. R.; Charbonneau, P.; Li, Z.-Y.; Wiley, B. J., The effect of nanowire length and diameter on the properties of transparent, conducting nanowire films. *Nanoscale* **2012,** *4* (6), 1996-2004.

19. Stewart, I. E.; Kim, M. J.; Wiley, B. J., Effect of Morphology on the Electrical Resistivity of Silver Nanostructure Films. *ACS Appl. Mater. Interfaces* **2017,** *9* (2), 1870-1876.

20. Hsieh, M.-C.; Kim, C.; Nogi, M.; Suganuma, K., Electrically conductive lines on cellulose nanopaper for flexible electrical devices. *Nanoscale* **2013,** *5* (19), 9289-9295.

21. Finn, D. J.; Lotya, M.; Coleman, J. N., Inkjet Printing of Silver Nanowire Networks. *ACS Appl. Mater. Interfaces* **2015,** *7* (17), 9254-9261.

22. Tobjörk, D.; Österbacka, R., Paper Electronics. *Adv. Mater.* **2011,** *23* (17), 1935-1961.

23. Suganuma, K., *Introduction to Printed Electronics*. Springer New York: [S.l.], 2013.

24. Van Osch, T. H.; Perelaer, J.; de Laat, A. W.; Schubert, U. S., Inkjet printing of narrow conductive tracks on untreated polymeric substrates. *Adv. Mater.* **2008,** *20* (2), 343-345.

25. Lau, P. H.; Takei, K.; Wang, C.; Ju, Y.; Kim, J.; Yu, Z.; Takahashi, T.; Cho, G.; Javey, A., Fully Printed, High Performance Carbon Nanotube Thin-Film Transistors on Flexible Substrates. *Nano Lett.* **2013,** *13* (8), 3864-3869.

26. Molina-Lopez, F.; Briand, D.; de Rooij, N. F., All additive inkjet printed humidity sensors on plastic substrate. *Sensor Actuat B-Chem* **2012,** *166*, 212-222.

27. Yang, L.; Rida, A.; Vyas, R.; Tentzeris, M. M., RFID tag and RF structures on a paper substrate using inkjet-printing technology. *IEEE Trans. Microwave Theory Tech.* **2007,** *55* (12), 2894-2901.

28. Facchetti, A., Π-conjugated polymers for organic electronics and photovoltaic cell applications†. *Chem. Mater.* **2010,** *23* (3), 733-758.

29. Kopola, P.; Tuomikoski, M.; Suhonen, R.; Maaninen, A., Gravure printed organic light emitting diodes for lighting applications. *Thin Solid Films* **2009,** *517* (19), 5757-5762.

30. Lee, J.; Lee, P.; Lee, H. B.; Hong, S.; Lee, I.; Yeo, J.; Lee, S. S.; Kim, T.-S.; Lee, D.; Ko, S. H., Room-Temperature Nanosoldering of a Very Long Metal Nanowire Network by Conducting-Polymer-Assisted Joining for a Flexible Touch-Panel Application. *Adv. Funct. Mater.* **2013,** *23* (34), 4171-4176.

31. Chang, J.; Zhang, X.; Ge, T.; Zhou, J., Fully printed electronics on flexible substrates: High gain amplifiers and DAC. *Org. Electron.* **2014,** *15* (3), 701-710.

32. Gaikwad, A. M.; Steingart, D. A.; Ng, T. N.; Schwartz, D. E.; Whiting, G. L., A flexible high potential printed battery for powering printed electronics. *Appl. Phys. Lett.* **2013,** *102* (23), 233302.

33. Arias, A. C.; Daniel, J.; Krusor, B.; Ready, S.; Sholin, V.; Street, R., All-additive ink-jet-printed display backplanes: Materials development and integration. *J. Soc. Inf. Disp.* **2007,** *15* (7), 485-490.

34. Magliulo, M.; Mulla, M.; Singh, M.; Macchia, E.; Tiwari, A.; Torsi, L.; Manoli, K., Printable and flexible electronics: from TFTs to bioelectronic devices. *J. Mater. Chem. C.* **2015,** *3* (48), 12347-12363.

35. Han, S.-T.; Zhou, Y.; Roy, V. A. L., Towards the Development of Flexible Non-Volatile Memories. *Adv. Mater.* **2013,** *25* (38), 5425-5449.

36. Lin, H. T.; Pei, Z.; Chen, J. R.; Kung, C. P.; Lin, Y. C.; Tseng, C. M.; Chan, Y. J. In *A 16-Byte Nonvolatile Bistable Polymer Memory Array on Plastic Substrates*, 2007 IEEE International Electron Devices Meeting, 10-12 Dec. 2007; 2007; pp 233-236.

37. Jung, M.; Kim, J.; Noh, J.; Lim, N.; Lim, C.; Lee, G.; Kim, J.; Kang, H.; Jung, K.; Leonard, A. D.; Tour, J. M.; Cho, G., All-Printed and Roll-to-Roll-Printable 13.56-MHz-Operated 1-bit RF Tag on Plastic Foils. *IEEE Trans. Electron Devices* **2010,** *57* (3), 571-580.

38. Bhansali, U. S.; Khan, M. A.; Alshareef, H. N., Organic ferroelectric memory devices with inkjet-printed polymer electrodes on flexible substrates. *Microelectron. Eng.* **2013,** *105*, 68-73.

39. Ng, T. N.; Schwartz, D. E.; Lavery, L. L.; Whiting, G. L.; Russo, B.; Krusor, B.; Veres, J.; Bröms, P.; Herlogsson, L.; Alam, N.; Hagel, O.; Nilsson, J.; Karlsson, C., Scalable printed electronics: an organic decoder addressing ferroelectric non-volatile memory. *Sci. Rep.* **2012,** *2*, 585.

40. Bak, J. Y.; Jung, S. W.; Yoon, S. M., Nonvolatile memory performance improvements for solution-processed thin-film transistors with composition-modified In–Zn–Ti–O active channel and ferroelectric copolymer gate insulator. *Org. Electron.* **2013,** *14* (9), 2148-2157.

41. Kim, C.; Song, J.-M.; Lee, J.-S.; Lee, M. J., All-solution-processed nonvolatile flexible nano-floating gate memory devices. *Nanotechnology* **2013,** *25* (1), 014016.

42. Baeg, K. J.; Khim, D.; Kim, J.; Yang, B. D.; Kang, M.; Jung, S. W.; You, I. K.; Kim, D. Y.; Noh, Y. Y., High-performance top-gated organic field-effect transistor memory using electrets for monolithic printed flexible NAND flash memory. *Adv. Funct. Mater.* **2012,** *22* (14), 2915-2926.

43. Siddiqui, G. U.; Rehman, M. M.; Choi, K. H., Enhanced resistive switching in all-printed, hybrid and flexible memory device based on perovskite ZnSnO 3 via PVOH polymer. *Polymer* **2016,** *100*, 102-110.

44. Rehman, M. M.; Siddiqui, G. U.; Gul, J. Z.; Kim, S.-W.; Lim, J. H.; Choi, K. H., Resistive Switching in All-Printed, Flexible and Hybrid MoS2-PVA Nanocomposite based Memristive Device Fabricated by Reverse Offset. *Sci. Rep.* **2016,** *6*, 36195.

45. Laplante, P. A.; Ovaska, S. J., *Real-time systems design and analysis: tools for the practitioner*. John Wiley and Sons: 2011.

46. Chua, L. O., Memristor-the missing circuit element. *IEEE Trans. Circuit Theory* **1971,** *18* (5), 507-519.

47. Waser, R.; Dittmann, R.; Staikov, G.; Szot, K., Redox-based resistive switching memories–nanoionic mechanisms, prospects, and challenges. *Adv. Mater.* **2009,** *21* (25-26), 2632-2663.

48. Duraisamy, N.; Muhammad, N. M.; Kim, H.-C.; Jo, J.-D.; Choi, K.-H., Fabrication of TiO2 thin film memristor device using electrohydrodynamic inkjet printing. *Thin Solid Films* **2012,** *520* (15), 5070-5074.

49. Lien, D.-H.; Kao, Z.-K.; Huang, T.-H.; Liao, Y.-C.; Lee, S.-C.; He, J.-H., All-Printed Paper Memory. *ACS Nano* **2014,** *8* (8), 7613-7619.

50. Vishwanath, S. K.; Kim, J., Resistive switching characteristics of all-solution-based Ag/TiO2/Mo-doped In2O3 devices for non-volatile memory applications. *J. Mater. Chem. C.* **2016,** *4* (46), 10967-10972.

51. Awais, M. N.; Muhammad, N. M.; Navaneethan, D.; Kim, H. C.; Jo, J.; Choi, K. H., Fabrication of ZrO2 layer through electrohydrodynamic atomization for the printed resistive switch (memristor). *Microelectron. Eng.* **2013,** *103*, 167-172.

52. Muhammad, N. M.; Duraisamy, N.; Rahman, K.; Dang, H. W.; Jo, J.; Choi, K. H., Fabrication of printed memory device having zinc-oxide active nano-layer and investigation of resistive switching. *Curr. Appl. Phys.* **2013,** *13* (1), 90-96.

53. Zou, S.; Michael, C. In *Flexible non-volatile Cu/Cu x O/Ag ReRAM memory devices fabricated using ink-jet printing technology*, 2014 IEEE 64th Electronic Components and Technology Conference (ECTC), IEEE: 2014; pp 441-446.

54. Bessonov, A. A.; Kirikova, M. N.; Petukhov, D. I.; Allen, M.; Ryhänen, T.; Bailey, M. J., Layered memristive and memcapacitive switches for printable electronics. *Nat. Mater.* **2015,** *14* (2), 199-204.

55. Huber, B.; Popp, P. B.; Kaiser, M.; Ruediger, A.; Schindler, C., Fully inkjet printed flexible resistive memory. *Appl. Phys. Lett.* **2017,** *110* (14), 143503.

56. Awais, M. N.; Kim, H. C.; Doh, Y. H.; Choi, K. H., ZrO 2 flexible printed resistive (memristive) switch through electrohydrodynamic printing process. *Thin Solid Films* **2013,** *536*, 308-312.

57. Vilmi, P.; Nelo, M.; Voutilainen, J.-V.; Palosaari, J.; Pörhönen, J.; Tuukkanen, S.; Jantunen, H.; Juuti, J.; Fabritius, T., Fully printed memristors for a self-sustainable recorder of mechanical energy. *Flex. Print. Electron.* **2016,** *1* (2), 025002.

58. Rahman, K.; Mustafa, M.; Muhammad, N.; Choi, K., Electrohydrodynamic printed TiO2 flexible memory device-fabrication and characterisation. *Electron. Lett.* **2012,** *48* (20), 1261.

59. Zou, S.; Xu, P.; Hamilton, M., Resistive switching characteristics in printed Cu/CuO/(AgO)/Ag memristors. *Electron. Lett.* **2013,** *49* (13), 829-830.

60. Siddiqui, G.-u.-d.; Ali, J.; Doh, Y.-H.; Choi, K. H., Fabrication of zinc stannate based all-printed resistive switching device. *Mater. Lett.* **2016,** *166*, 311-316.

61. Kim, A.; Song, K.; Kim, Y.; Moon, J., All solution-processed, fully transparent resistive memory devices. *ACS Appl. Mater. Interfaces* **2011,** *3* (11), 4525-4530.

62. Awais, M. N.; Choi, K. H., Resistive switching and current conduction mechanism in full organic resistive switch with the sandwiched structure of poly(3,4-ethylenedioxythiophene): poly(styrenesulfonate)/poly(4-vinylphenol)/poly(3,4-ethylenedioxythiophene): poly(styrenesulfonate). *Electron. Mater. Lett.* **2014,** *10* (3), 601-606.

63. Ali, S.; Bae, J.; Lee, C. H.; Shin, S.; Kobayashi, N. P., Ultra-low power non-volatile resistive crossbar memory based on pull up resistors. *Org. Electron.* **2017,** *41*, 73-78.

64. Rehman, M. M.; Yang, B.-S.; Yang, Y.-J.; Karimov, K. S.; Choi, K. H., Effect of device structure on the resistive switching characteristics of organic polymers fabricated through all printed technology. *Curr. Appl. Phys.* **2017,** *17* (4), 533-540.

65. Catenacci, M. J.; Flowers, P. F.; Cao, C.; Andrews, J. B.; Franklin, A. D.; Wiley, B. J., Fully Printed Memristors from Cu–SiO2 Core–Shell Nanowire Composites. *J. Electron. Mater.* **2017,** *46* (7), 4596-4603.

66. Flowers, P. F.; Catenacci, M. J.; Wiley, B. J., High-speed, solution-coatable memory based on Cu-SiO2 core-shell nanowires. *Nanoscale Horiz.* **2016,** *1* (4), 313-316.

67. Schindler, C.; Weides, M.; Kozicki, M. N.; Waser, R., Low current resistive switching in Cu–SiO2 cells. *Appl. Phys. Lett.* **2008,** *92* (12), 122910.

68. Schindler, C.; Staikov, G.; Waser, R., Electrode kinetics of Cu–SiO2-based resistive switching cells: Overcoming the voltage-time dilemma of electrochemical metallization memories. *Appl. Phys. Lett.* **2009,** *94* (7), 072109.

69. Thermadam, S. P.; Bhagat, S. K.; Alford, T. L.; Sakaguchi, Y.; Kozicki, M. N.; Mitkova, M., Influence of Cu diffusion conditions on the switching of Cu–SiO2-based resistive memory devices. *Thin Solid Films* **2010,** *518* (12), 3293-3298.

70. Kobayashi, Y.; Katakami, H.; Mine, E.; Nagao, D.; Konno, M.; Liz-Marzán, L. M., Silica coating of silver nanoparticles using a modified Stöber method. *J. Colloid Interface Sci.* **2005,** *283* (2), 392-396.

71. Sekitani, T.; Nakajima, H.; Maeda, H.; Fukushima, T.; Aida, T.; Hata, K.; Someya, T., Stretchable active-matrix organic light-emitting diode display using printable elastic conductors. *Nat Mater* **2009,** *8* (6), 494-499.

72. Yamada, T.; Hayamizu, Y.; Yamamoto, Y.; Yomogida, Y.; Izadi-Najafabadi, A.; Futaba, D. N.; Hata, K., A stretchable carbon nanotube strain sensor for human-motion detection. *Nature Nanotechnology* **2011,** *6*, 296.

73. Yan, C.; Wang, J.; Kang, W.; Cui, M.; Wang, X.; Foo, C. Y.; Chee, K. J.; Lee, P. S., Highly Stretchable Piezoresistive Graphene–Nanocellulose Nanopaper for Strain Sensors. *Adv. Mater.* **2014,** *26* (13), 2022-2027.

74. Hong, S.; Lee, H.; Lee, J.; Kwon, J.; Han, S.; Suh, Y. D.; Cho, H.; Shin, J.; Yeo, J.; Ko, S. H., Highly Stretchable and Transparent Metal Nanowire Heater for Wearable Electronics Applications. *Adv. Mater.* **2015,** *27* (32), 4744-4751.

75. Joshipura, I. D.; Finn, M.; Tan, S. T. M.; Dickey, M. D.; Lipomi, D. J., Stretchable bioelectronics—Current and future. *MRS Bull.* **2017,** *42* (12), 960-967.

76. Xu, S.; Zhang, Y.; Cho, J.; Lee, J.; Huang, X.; Jia, L.; Fan, J. A.; Su, Y.; Su, J.; Zhang, H.; Cheng, H.; Lu, B.; Yu, C.; Chuang, C.; Kim, T.-i.; Song, T.; Shigeta, K.; Kang, S.; Dagdeviren, C.; Petrov, I.; Braun, P. V.; Huang, Y.; Paik, U.; Rogers, J. A., Stretchable batteries with self-similar serpentine interconnects and integrated wireless recharging systems. *Nature Communications* **2013,** *4*, 1543.

77. Sekitani, T.; Noguchi, Y.; Hata, K.; Fukushima, T.; Aida, T.; Someya, T., A Rubberlike Stretchable Active Matrix Using Elastic Conductors. *Science* **2008,** *321* (5895), 1468-1472.

78. Kim, K. H.; Vural, M.; Islam, M. F., Single-Walled Carbon Nanotube Aerogel-Based Elastic Conductors. *Adv. Mater.* **2011,** *23* (25), 2865-2869.

79. Duan, S.; Wang, Z.; Zhang, L.; Liu, J.; Li, C., Three-Dimensional Highly Stretchable Conductors from Elastic Fiber Mat with Conductive Polymer Coating. *ACS Appl. Mater. Interfaces* **2017,** *9* (36), 30772-30778.

80. Stoyanov, H.; Kollosche, M.; Risse, S.; Waché, R.; Kofod, G., Soft Conductive Elastomer Materials for Stretchable Electronics and Voltage Controlled Artificial Muscles. *Adv. Mater.* **2013,** *25* (4), 578-583.

81. Matsuhisa, N.; Kaltenbrunner, M.; Yokota, T.; Jinno, H.; Kuribara, K.; Sekitani, T.; Someya, T., Printable elastic conductors with a high conductivity for electronic textile applications. *Nature Communications* **2015,** *6*, 7461.

82. Matsuhisa, N.; Inoue, D.; Zalar, P.; Jin, H.; Matsuba, Y.; Itoh, A.; Yokota, T.; Hashizume, D.; Someya, T., Printable elastic conductors by in situ formation of silver nanoparticles from silver flakes. *Nat. Mater.* **2017,** *16*, 834.

83. Oh, Y.; Yoon, I. S.; Lee, C.; Kim, S. H.; Ju, B.-K.; Hong, J.-M., Selective photonic sintering of Ag flakes embedded in silicone elastomers to fabricate stretchable conductors. *J. Mater. Chem. C.* **2017,** *5* (45), 11733-11740.

84. Huang, W.; Li, J.; Zhao, S.; Han, F.; Zhang, G.; Sun, R.; Wong, C.-P., Highly electrically conductive and stretchable copper nanowires-based composite for flexible and printable electronics. *Compos. Sci. Technol.* **2017,** *146*, 169-176.

85. Lipomi, D. J.; Vosgueritchian, M.; Tee, B. C. K.; Hellstrom, S. L.; Lee, J. A.; Fox, C. H.; Bao, Z., Skin-like pressure and strain sensors based on transparent elastic films of carbon nanotubes. *Nature Nanotechnology* **2011,** *6*, 788.

86. Wang, Y.; Zhu, C.; Pfattner, R.; Yan, H.; Jin, L.; Chen, S.; Molina-Lopez, F.; Lissel, F.; Liu, J.; Rabiah, N. I.; Chen, Z.; Chung, J. W.; Linder, C.; Toney, M. F.; Murmann, B.; Bao, Z., A highly stretchable, transparent, and conductive polymer. *Science Advances* **2017,** *3* (3).

87. Gutowski, T. G.; Sahni, S.; Allwood, J. M.; Ashby, M. F.; Worrell, E., The energy required to produce materials: constraints on energy-intensity improvements, parameters of demand. *Philosophical Transactions of the Royal Society A: Mathematical, Physical and Engineering Sciences* **2013,** *371* (1986).

88. Li, S.; Chen, Y.; Huang, L.; Pan, D., Large-Scale Synthesis of Well-Dispersed Copper Nanowires in an Electric Pressure Cooker and Their Application in Transparent and Conductive Networks. *Inorg. Chem.* **2014,** *53* (9), 4440-4444.

89. Tang, Y.; Gong, S.; Chen, Y.; Yap, L. W.; Cheng, W., Manufacturable Conducting Rubber Ambers and Stretchable Conductors from Copper Nanowire Aerogel Monoliths. *ACS Nano* **2014,** *8* (6), 5707-5714.

90. Chen, Z.; Ren, W.; Gao, L.; Liu, B.; Pei, S.; Cheng, H.-M., Three-dimensional flexible and conductive interconnected graphene networks grown by chemical vapour deposition. *Nat. Mater.* **2011,** *10*, 424.

91. Stewart, I. E.; Ye, S.; Chen, Z.; Flowers, P. F.; Wiley, B. J., Synthesis of Cu–Ag, Cu–Au, and Cu–Pt Core–Shell Nanowires and Their Use in Transparent Conducting Films. *Chem. Mater.* **2015,** *27* (22), 7788-7794.

92. Ye, S.; Rathmell, A. R.; Ha, Y.-C.; Wilson, A. R.; Wiley, B. J., The Role of Cuprous Oxide Seeds in the One-Pot and Seeded Syntheses of Copper Nanowires. *Small* **2014,** *10* (9), 1771-1778.

93. Sumi, D.; Dhanabalan, A.; Thimmappa, B.; Krishnamurthy, S., Effect of colloidal silica dispersions on the properties of PDMS-colloidal silica composites. *Journal of Applied Polymer Science* **2012,** *125* (S1), E515-E522.

94. Meng, Y.; Li, Z. B.; Chen, X.; Chen, J. P., Reducing wrinkles and cracks of metal films on PDMS substrate by hexane extraction and oxygen plasma etching. *Microelectron. Eng.* **2014,** *130*, 8-12.

95. Shin, D.-H.; Woo, S.; Yem, H.; Cha, M.; Cho, S.; Kang, M.; Jeong, S.; Kim, Y.; Kang, K.; Piao, Y., A self-reducible and alcohol-soluble copper-based metal–organic decomposition ink for printed electronics. *ACS Appl. Mater. Interfaces* **2014,** *6* (5), 3312-3319.

96. Yin, Y.; Lu, Y.; Sun, Y.; Xia, Y., Silver Nanowires Can Be Directly Coated with Amorphous Silica To Generate Well-Controlled Coaxial Nanocables of Silver/Silica. *Nano Lett.* **2002,** *2* (4), 427-430.

97. Kim, S.; Moon, H.; Gupta, D.; Yoo, S.; Choi, Y. K., Resistive Switching Characteristics of Sol-Gel Zinc Oxide Films for Flexible Memory Applications. *IEEE Trans. Electron Devices* **2009,** *56* (4), 696-699.

98. Seo, J. W.; Park, J.-W.; Lim, K. S.; Kang, S. J.; Hong, Y. H.; Yang, J. H.; Fang, L.; Sung, G. Y.; Kim, H.-K., Transparent flexible resistive random access memory fabricated at room temperature. *Appl. Phys. Lett.* **2009,** *95* (13), 133508.

99. Linn, E.; Rosezin, R.; Kugeler, C.; Waser, R., Complementary resistive switches for passive nanocrossbar memories. *Nat Mater* **2010,** *9* (5), 403-406.

100. Kim, K.-H.; Gaba, S.; Wheeler, D.; Cruz-Albrecht, J. M.; Hussain, T.; Srinivasa, N.; Lu, W., A Functional Hybrid Memristor Crossbar-Array/CMOS System for Data Storage and Neuromorphic Applications. *Nano Lett.* **2012,** *12* (1), 389-395.

101. Zidan, M. A.; Fahmy, H. A. H.; Hussain, M. M.; Salama, K. N., Memristor-based memory: The sneak paths problem and solutions. *Microelectron. J.* **2013,** *44* (2), 176-183.

102. Yang, J. J.; Zhang, M.-X.; Pickett, M. D.; Miao, F.; Strachan, J. P.; Li, W.-D.; Yi, W.; Ohlberg, D. A.; Choi, B. J.; Wu, W., Engineering nonlinearity into memristors for passive crossbar applications. *Appl. Phys. Lett.* **2012,** *100* (11), 113501.

103. Zhou, J.; Kim, K.-H.; Lu, W., Crossbar RRAM arrays: Selector device requirements during read operation. *IEEE Trans. Electron Devices* **2014,** *61* (5), 1369-1376.

104. Savagatrup, S.; Makaram, A. S.; Burke, D. J.; Lipomi, D. J., Mechanical Properties of Conjugated Polymers and Polymer-Fullerene Composites as a Function of Molecular Structure. *Adv. Funct. Mater.* **2014,** *24* (8), 1169-1181.

105. Lee, J.-B.; Khang, D.-Y., Electrical and mechanical characterization of stretchable multi-walled carbon nanotubes/polydimethylsiloxane elastomeric composite conductors. *Compos. Sci. Technol.* **2012,** *72* (11), 1257-1263.

106. Lu, N.; Lu, C.; Yang, S.; Rogers, J., Highly Sensitive Skin-Mountable Strain Gauges Based Entirely on Elastomers. *Adv. Funct. Mater.* **2012,** *22* (19), 4044-4050.

107. Zu, M.; Li, Q.; Wang, G.; Byun, J.-H.; Chou, T.-W., Carbon Nanotube Fiber Based Stretchable Conductor. *Adv. Funct. Mater.* **2013,** *23* (7), 789-793.

108. Chen, M.; Zhang, L.; Duan, S.; Jing, S.; Jiang, H.; Luo, M.; Li, C., Highly conductive and flexible polymer composites with improved mechanical and electromagnetic interference shielding performances. *Nanoscale* **2014,** *6* (7), 3796-3803.

109. Zhao, S.; Li, J.; Cao, D.; Zhang, G.; Li, J.; Li, K.; Yang, Y.; Wang, W.; Jin, Y.; Sun, R.; Wong, C.-P., Recent Advancements in Flexible and Stretchable Electrodes for Electromechanical Sensors: Strategies, Materials, and Features. *ACS Appl. Mater. Interfaces* **2017,** *9* (14), 12147-12164.

110. Rosset, S.; Niklaus, M.; Dubois, P.; Shea, H. R., Metal Ion Implantation for the Fabrication of Stretchable Electrodes on Elastomers. *Adv. Funct. Mater.* **2009,** *19* (3), 470-478.

111. Gent, A. N.; Park, B., Failure processes in elastomers at or near a rigid spherical inclusion. *Journal of Materials Science* **1984,** *19* (6), 1947-1956.

112. Ahagon, A.; Gent, A. N., Effect of interfacial bonding on the strength of adhesion. *Journal of Polymer Science: Polymer Physics Edition* **1975,** *13* (7), 1285-1300.

113. Lessing, J.; Morin, S. A.; Keplinger, C.; Tayi, A. S.; Whitesides, G. M., Stretchable Conductive Composites Based on Metal Wools for Use as Electrical Vias in Soft Devices. *Adv. Funct. Mater.* **2015,** *25* (9), 1418-1425.

114. Hansen, T. S.; West, K.; Hassager, O.; Larsen, N. B., Highly Stretchable and Conductive Polymer Material Made from Poly(3,4-ethylenedioxythiophene) and Polyurethane Elastomers. *Adv. Funct. Mater.* **2007,** *17* (16), 3069-3073.

115. Araki, T.; Sugahara, T.; Nogi, M.; Suganuma, K., Effect of void volume and silver loading on strain response of electrical resistance in silver flakes/polyurethane composite for stretchable conductors. *Jpn. J. Appl. Phys.* **2012,** *51* (11S), 11PD01.

116. Yamaguchi, K.; Busfield, J. J. C.; Thomas, A. G., Electrical and mechanical behavior of filled elastomers. I. The effect of strain. *J. Polym. Sci., Part B: Polym. Phys.* **2003,** *41* (17), 2079-2089.

117. Hanson, D. E.; Hawley, M.; Houlton, R.; Chitanvis, K.; Rae, P.; Orler, E. B.; Wrobleski, D. A., Stress softening experiments in silica-filled polydimethylsiloxane provide insight into a mechanism for the Mullins effect. *Polymer* **2005,** *46* (24), 10989-10995.

118. Cantournet, S.; Desmorat, R.; Besson, J., Mullins effect and cyclic stress softening of filled elastomers by internal sliding and friction thermodynamics model. *International Journal of Solids and Structures* **2009,** *46* (11), 2255-2264.

119. Fukahori, Y., New progress in the theory and model of carbon black reinforcement of elastomers. *Journal of Applied Polymer Science* **2005,** *95* (1), 60-67.

120. Liu, C.-X.; Choi, J.-W., Analyzing resistance response of embedded PDMS and carbon nanotubes composite under tensile strain. *Microelectron. Eng.* **2014,** *117*, 1-7.

121. Wang, C.; Li, X.; Gao, E.; Jian, M.; Xia, K.; Wang, Q.; Xu, Z.; Ren, T.; Zhang, Y., Carbonized Silk Fabric for Ultrastretchable, Highly Sensitive, and Wearable Strain Sensors. *Adv. Mater.* **2016,** *28* (31), 6640-6648.

122. Zhang, M.; Wang, C.; Wang, Q.; Jian, M.; Zhang, Y., Sheath–Core Graphite/Silk Fiber Made by Dry-Meyer-Rod-Coating for Wearable Strain Sensors. *ACS Appl. Mater. Interfaces* **2016,** *8* (32), 20894-20899.

123. Kim, B. K.; Lee, J. C., Waterborne polyurethanes and their properties. *J. Polym. Sci., Part A: Polym. Chem.* **1996,** *34* (6), 1095-1104.

124. Lee, S. Y.; Lee, J. S.; Kim, B. K., Preparation and Properties of Water-borne Polyurethanes. *Polym. Int.* **1997,** *42* (1), 67-76.

125. Johnson, L. M.; Gao, L.; Shields IV, C. W.; Smith, M.; Efimenko, K.; Cushing, K.; Genzer, J.; López, G. P., Elastomeric microparticles for acoustic mediated bioseparations. *Journal of Nanobiotechnology* **2013,** *11* (1), 22.

126. Cheng, P. L.; Berney, C. V.; Cohen, R. E., Distribution of chain ends inside the polybutadiene microspheres of styrene-butadiene diblock copolymers. *Macromolecules* **1988,** *21* (12), 3442-3446.

127. Qian, F.; Lan, P. C.; Freyman, M. C.; Chen, W.; Kou, T.; Olson, T. Y.; Zhu, C.; Worsley, M. A.; Duoss, E. B.; Spadaccini, C. M.; Baumann, T.; Han, T. Y.-J., Ultralight Conductive Silver Nanowire Aerogels. *Nano Lett.* **2017,** *17* (12), 7171-7176.

128. Philipse, A. P., The Random Contact Equation and Its Implications for (Colloidal) Rods in Packings, Suspensions, and Anisotropic Powders. *Langmuir* **1996,** *12* (5), 1127-1133.

129. Philipse, A. P.; Wierenga, A. M., On the Density and Structure Formation in Gels and Clusters of Colloidal Rods and Fibers. *Langmuir* **1998,** *14* (1), 49-54.

130. Balberg, I.; Binenbaum, N.; Wagner, N., Percolation Thresholds in the Three-Dimensional Sticks System. *Phys. Rev. Lett.* **1984,** *52* (17), 1465-1468.

131. Solomon, M. J.; Spicer, P. T., Microstructural regimes of colloidal rod suspensions, gels, and glasses. *Soft Matter* **2010,** *6* (7), 1391-1400.

132. Nordenström, M.; Fall, A.; Nyström, G.; Wågberg, L., Formation of Colloidal Nanocellulose Glasses and Gels. *Langmuir* **2017,** *33* (38), 9772-9780.

Biography

Matthew Joseph Catenacci was born on April 6, 1991 in Flemington, NJ. He graduated from the University of Notre Dame in May 2013 with a BS degree in chemistry and a minor in environmental geosciences, and performed undergraduate research under the supervision of Prof. Gregory Hartland. In the spring of 2014, he began work towards his PhD in chemistry under the supervision of Prof. Benjamin Wiley. The focus of his research has been exploring practical electronic applications for copper nanowires through investigating their structure-property relationships. Matthew has published research articles in this field in peer reviewed journals including: "Fully Printed Memristors from Cu-SiO_2 Core-Shell Nanowire Composites", "Stretchable Conductive Composites from Cu-Ag Nanowire Felt", "High-Speed Solution-Coatable Memory Based on Cu-SiO_2 Core-Shell Nanowires", and "Production of Oxidation-Resistant Cu-Based Nanoparticles by Wire Explosion". During his time at Duke, he has been a recipient of the Paul M. Gross Fellowship to fund his research.